N° d'ordre : 4394

THÈSE

Présentée et soutenue publiquement le 5 Décembre 2011 à

L'UNIVERSITÉ BORDEAUX 1

ÉCOLE DOCTORALE DES SCIENCES PHYSIQUES ET DE L'INGENIEUR

Par

Fulvio INFANTE

Pour obtenir le grade de

DOCTEUR
Spécialité : ÉLECTRONIQUE

"Development of Magnetic Microscopy techniques for failure localization on three-dimensional circuits"

« Développement des techniques de Microscopie Magnétique pour la localisation des défauts dans les circuits tridimensionnels »

Après avis de :

Mme	Christelle AUPETIT	*Professeur*	*Université de Limoge*	*Rapporteur*
Mme	Sylvie JARRIX	*Professeur*	*Université Montpellier 2*	*Rapporteur*

Devant la commission formée de :

Mme	Christelle AUPETIT	*Professeur*	*Université de Limoge*	*Rapporteur*
Mme	Sylvie JARRIX	*Professeur*	*Université Montpellier 2*	*Rapporteur*
Ms	Dean LEWIS	*Professeur*	*Université de Bordeaux 1*	*Dir. de Thèse*
Ms	Philippe PERDU	*Docteur-Ingenieur*	*CNES*	*Dir. de Thèse*
Ms	Vincent POUGET	*Chargé de recherche*	*CNRS*	*Examinateur*
Mme	Nathalie MALBERT	*Professeur*	*Université de Bordeaux 1*	*Examinateur*
Ms	Antonio OROZCO	*Docteur-Ingenieur*	*Neocera*	*Membre invité*

Contents

IV Application of the new techniques to case studies 125

List of Figures

List of Tables

Acknowledgements

I would firstly like to express my most sincere gratitude to Dr.Philippe Perdu, my CNES supervisor, for giving me the chance to work on this project and for helping me in a way no one else could have. This work could not have been done without his help: I will never forget the time he spent with me and our long after-hour discussions on all subjects.

I would also like to thank Prof. Dean Lewis, my Ph.D. director from the University of Bordeaux, for all his help and guidance during this project.

My time at CNES was made so much nicer by my colleagues; I would like to thank them all. I want to especially thank Francis Pressecq, the head of department, and Patrick Saunier, the head of the sub-directorate, for having welcomed me to the laboratory. My sincere thanks also go to Kevin Sanchez, for his many useful comments and suggestions on how to keep improving my work.

During the three years of my doctorate, I could always count on the support of my fellow students. I would therefore like to thank Magdalena Sienkiewicz, Amjad Deyne and Julie Ferrigno. A special thanks goes to Jerome di Battista: after sharing an office with him, no one's life could ever be the same again. I would also like to acknowledge the people working in our laboratory from Novamems and Thales. Naming them all would keep me writing for hours, but their company has always been deeply appreciated.

I would also like to acknowledge Dr.Antonio Orozco and Jan Gaudestad, from Neocera, for their help with the Magma tool. Their knowledge on Magnetic Microscopy is unique, and it has been an extreme pleasure to exchange information with them.

This project would not have been finished on time if it had not been for Richard, my father-in-law: I will always be grateful for the long hours he spent proofreading the English of this manuscript. If any mistake still remains, it is solely because of me. I will not forget Kate, my wife, who not only helped correct my English, but also supported me in every way possible, and put up with the long working weekends. And finally, Julia, my daughter, for making those weekends livelier than ever.

Introduction

Failure Analysis for electronics components is nowadays a very important step during the conception and development of new electronic devices. When a component is found to be defective, it is very important to understand the causes of the malfunction so that corrective measures can be put into practice. In this way it is possible to prevent the same problem from repeating itself, and save huge amounts of money which would have been spent on the customer returns of defective systems. It is in fact a lot cheaper for the electronic industry to identify the defective devices as early as possible in design, qualification and production process in order to avoid field return. After that, the components are assembled and sold to the customers: the cost linked to the failures during all this process increases constantly. Sometimes, as in the avionics electronics industry, or in space applications, it is of fundamental importance that the maximum reliability possible is obtained, as once the defect manifests itself it will be too late.

One of the most complex steps of Failure Analysis is the defect localization: this is necessary to pinpoint the exact spot in the device where the failure occurred. By doing so, it is possible to understand the root cause of the failure and therefore think of possible countermeasures to apply. As foreseen by Moore [1], the number of transistors inside a microchip doubles every year (this rate has then be adjusted, first to 18 months and then to 2 years). With a constant area of the chip, the size of each transistor is destined to keep shrinking more and more. The techniques for failure localization used during the years had to adapt and evolve in order to be able to keep up with this trend. While in the past the failure analyst worked with transistors of the size of hundreds of micrometers, nowadays he or she has to face the big challenge of localizing defects in a structure presenting transistors measuring tens of nanometers.

Still, with the physical limits of the transistors size quickly approaching, new ways of increasing the capabilities of the circuits have been found. This time, instead of trying to increase the number of transistors inside the single die, a number of ways to interconnect multiple dies inside the same package were developed. With the arrival of these new technologies it has become extremely complicated to perform a Failure Analysis (FA) process. The new packages have gone 'vertical' [2], as was foreseen by the More than Moore paradigm [3]. However, all the standard techniques for failure localization are only suitable for bi-dimensional packages: as soon as the third dimension brought by the stacking of different dies is taken under consideration, it becomes impossible to precisely localize the defect without proceeding to deprocess the component. Yet whenever the components are de-packaged, there is a high risk of destroying the defect and therefore losing all the relevant information. That is why, with the increase of System in Package use in industry, the need for non-destructive techniques for failure localization has quickly arisen.

This work was carried out in a collaboration between the IMS Laboratory, in the Bordeaux University, and the French Space Agency, CNES, in Toulouse. As three-dimensional components are more and more used for space applications (and it has been foreseen that their presence will even increase in the future), the CNES needs to be well aware of the difficulties that this type of technologies can bring to the failure analyst. Therefore the necessity of starting a thorough investigation of the techniques which could help to analyse these components arose.

In the present work some new developments on localization techniques for three-dimensional electronic components are shown. These are performed through the introduction of simulations for an already existing technique: Magnetic Microscopy (MM). The results obtained constitute one of the first steps to solve the failure localization problem in the direction of the More than Moore's world.

This document has been divided into four main parts. In the first part, a state of the art of new three-dimensional components assembly is described. It is then followed by an up to date FA process description, while keeping it as general as possible. A description of the devices reliability, in function of the time of usage of such devices is shown, allowing the reader to understand why the need of Failure Analysis has arisen in the first place. The whole process of failure analysis is then described in a general way, starting from the electrical characterization of the defect, to the final results. Understanding the process flow is of fundamental importance in order to understand why and when to use the different techniques. Furthermore, most of the techniques are complementary to each other, and only a deep and meticulous study of a single case can tell which techniques will be more appropriate. Localization techniques, which are the main topic of this entire work, are therefore explained in more detail. The most used techniques will be described in relation to their potential application to three-dimensional components.

A second part will then explain in a deeper detail the Magnetic Microscopy technique. To understand it, a short reminder of the physical laws which govern magnetic fields is needed. Therefore an introduction of the magnetic fields theory will bring the reader from the basic simplified Maxwell equations to the Biot-Savart's law, which governs the generation of the magnetic field from a arbitrary distribution of the current density. Understanding this passage is needed as the following chapter of this part will be dedicated to the opposite process: the magnetic microscopy technique is in fact used to reconstruct the current density once the magnetic field is given. This problem is referred to as the inversion problem for the magnetic field, and as it will be shown, it has no unique solution unless a certain number of constraints are applied. Finally, the MCI technique, which involves applying the inversion algorithm from the measurement of the z component of the magnetic field above the sample is described.

The third part of this work will be dedicated to the Simulation Approach (SA): a new methodology developed to extend the capabilities of Magnetic Microscopy techniques. The basic principle is that of comparing magnetic simulation generated by hypothetical current distributions to the magnetic acquisitions of the real current distribution. The evaluation of the correlation between the two will then give a measurement of the distance between them. Therefore, a magnetic simulator, based on the generation of the magnetic field from the Biot-Savart law, has been developed. As the simulation needs to be fast (to generate a vast set of different hypotheses) and accurate, a linear model was developed and programmed under the Scilab environment. As the most commonly used magnetic sensors can pick up only the z component of the magnetic field, by using these it is not possible to generate a map of the vertical currents: the currents flowing on the z axis do not give any contribution to the vertical component of the magnetic field. The methodology proposed in this work is that of performing a tilt of the sample. This will allow the measurement of the other components of the magnetic field, and therefore give additional information needed to localize vertical currents. This approach is then implemented in the simulation model. A last section will describe the possibility of applying the Simulation Approach on a bi-dimensional current distribution. It is in fact impossible, with the standard inversion algorithm, to generate a map of currents flowing inside a plane, as it happens on the ground planes or in the substrate of the electronic components. The proposed solution is still related to the simulations: the bi-dimensional current is discretized into a set of mono-dimensional currents as a resistor network, and then simulated.

Finally, in the fourth part a set of case studies will be shown along with the results obtained from this approach. The validity of the simulation methodology will be proven on different types of defects in different components. Starting from standard bi-dimensional components up to full three-dimensional multi-dies packages, this new approach is shown to be working on all types of samples.

There has been a skyrocketing increase in the evolution of three-dimensional structures in microelectronics in recent years: defect localization in such structures is a very important topic, and this work explains how this problem can be solved by using a novel approach based on Magnetic Microscopy analysis.

Part I

Failure Analysis: State of the art

CHAPTER I.1

New needs: 3D packaging

As far back as 1965, Gordon Moore, by looking at the trends of Integrated Circuits of the time, firstly understood what was going to be called later the Moore's Law: the number of transistors inside an Integrated Circuit (IC) would double every year [1]. This trend has been respected, with a few adjustments in the time slots, up to now. However, as the transistors move more and more into the nanoelectronics domain, the limitations of such scaling trend are not too far to be reached. Furthermore, the size of today's transistors is such that a number of new physical phenomena are being seen, which need to be studied in order to find a way to a solution. Consequently, the reliability of new ICs is constantly challenged: deep sub-micron technologies pay the price of high performances with the loss of yield, decrease in lifetime and reliability [4]. The easiest solution of this dilemma has therefore been the 3D: instead of, or even together with, decreasing the size of a single component, the industry started to move to the integration of more ICs inside the same package. Two other reasons for this type of integration are the new needs for so-called nomad applications, which need to be light and small, and cost related factors.

The need for heterogeneous functions in nomadic applications led to the invention of the System on Chip (SoC) technologies: having the possibility of mixing different technologies in the same substrate (for example, digital and analog) seemed to be the right way to overcome the limitations of standard ICs. However, the SoC solution presents a number of drawbacks: it still needs to follow Moore's law to increase its performances, and its reliability is still much lower than the standard ICs, as the integration of multiple technologies is not always straightforward [5][6].

I.1.1 More than Moore

As the standard ICs, following Moore's law, are not able to answer all of today's needs, a new axis of technology has been developed: what has been called the More than Moore (MtM) axis [3].

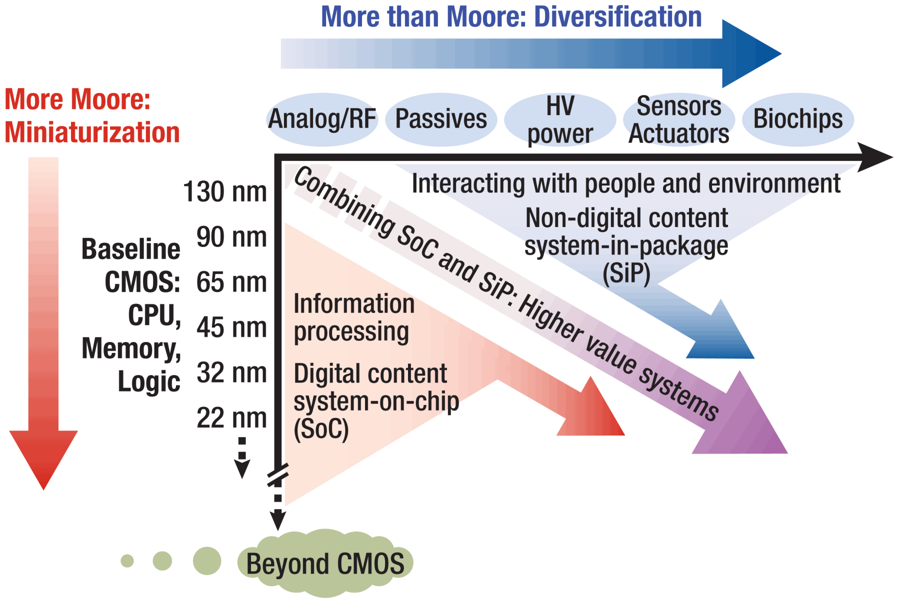

Figure I.1.1: More Moore and More than Moore

In the end, the combination of the two axes will give the best results in terms of performances, weight and size.

The More than Moore axis leads to the development and integration of different heterogeneous devices inside the same package. The resulting three-dimensional component, which has theoretically all included in one package, is the so called System in Package (SiP). The More than Moore market has been constantly growing during the last 10 years, and it is expected to keep growing due to the new applications on portable products [7][8].

I.1.2 SiP advantages

By using 3D technologies for the packaging, a set of advantages can be achieved [9]. The most visible ones are of course the size and weight of the package, which are extremely reduced with respect to the use of single packaged components.

As transistor sizes decrease more and more over time, the number of transistors on the same die increases exponentially. Therefore, a most limiting problem is the use of several metal layers. The interconnections in this way become longer and longer. It is now clear that they limit IC performances due to parasitic resistances and capacities [5]. Reduction of the interconnections by simply putting the different dies closer to each other, as in multi chip solutions, increases the component performances in terms of speed, noise and power consumption.

I.1.3 3D technologies

There is a wide set of SiP technologies, with different naming. In this section, a short review of the most common is given. A full bibliography on the different techniques for stacking ICs would be out of the scope for this document: the reader will be directed to the given references to get a deeper understanding of them.

I.1.3.1 Multi Chip Modules (MCM)

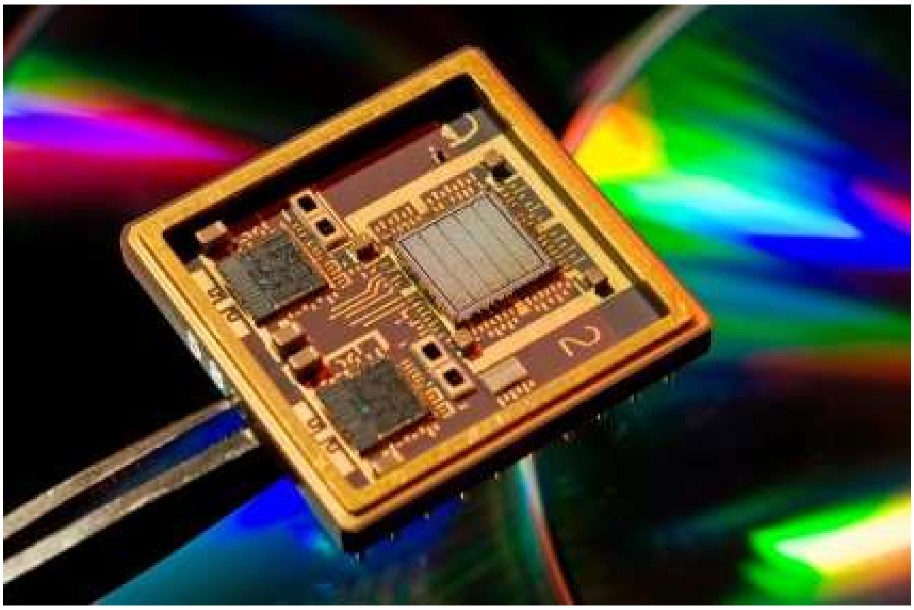

Figure I.1.2: Example of Multi Chip Module

MCMs were the first components to include a whole system inside one package. Even though there is more than one die in the package, the different dies are not stacked, but connected in the package on the same vertical layer. In comparison to 3D technologies, MCM are easier to build, and present a much higher yield: however, performances attainable with such components are not the same as those for SiPs, as the interconnections are much longer, and the silicon area wasted is much larger [10]. An example of Multi Chip Module can be seen in figure I.1.2.

I.1.3.2 Package on Package (PoP)

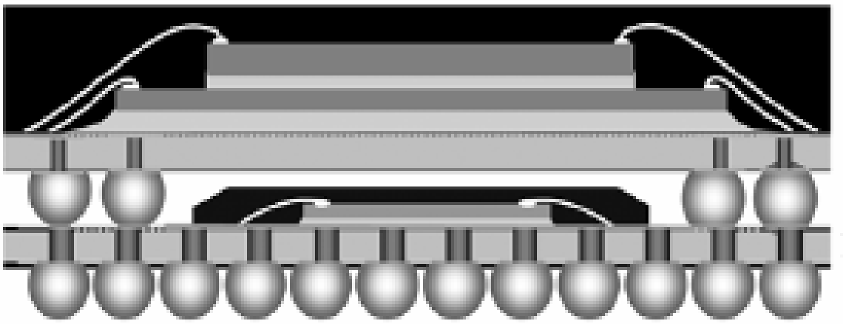

Figure I.1.3: Example of Package on Package device

The PoP is a solution to stack inside the same package two already packaged [10] devices. It is most often used for stacking memories together with a processor at the bottom: in figure I.1.3 an example of PoP is shown. The bottom layer, where the processor lies, has the possibility to have more connections through the external pins, while in the upper layer are stacked memory chips, needing fewer connections.

I.1.3.3 Package in Package (PiP)

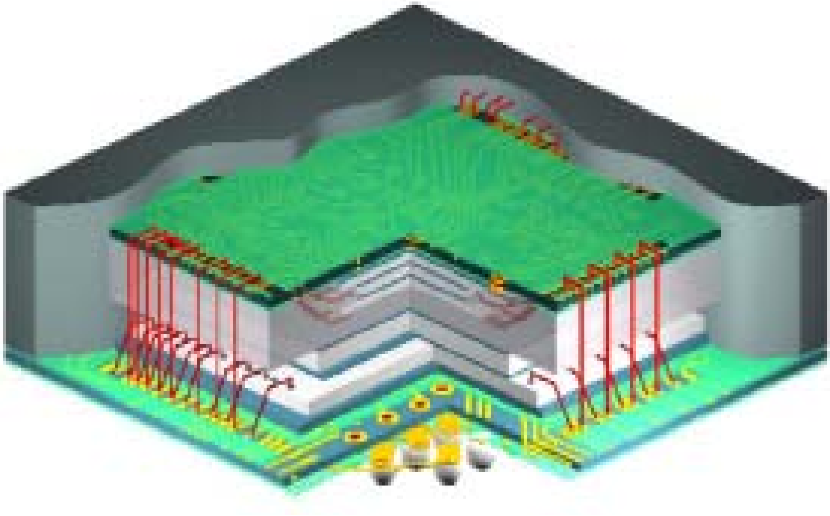

Figure I.1.4: Example of Package in Package device

PiP technology is very similar to the PoP. The difference is in the higher level of flexibility, so that more packages can be stacked one on top of each other and bonded together in a bigger package [11][10]. An example of PiP is shown in figure I.1.4.

I.1.3.4 System on Package (SoP)

From a definition given by Tummala [12], a System on Package differs from a SiP device by integrating not only active dies, but also passive components. However, from the assembly level Failure Analysis, which is the main subject of this work, the difference between SiP and SoP can be considered of no importance.

I.1.4 Vertical connections

From the point of view of a failure analyst, it can be very interesting to understand all the different types of vertical integrations for SiP devices. The number of possibilities for vertical connections is very wide; furthermore very often more than one connection technology is used in the same package, as for example in [13]. The way the vertical connections are performed is very important when trying to reconstruct the current paths flowing between the different layers. Therefore a brief explanation is needed, mostly regarding the position and type of such connections.

I.1.4.1 Bonding wires

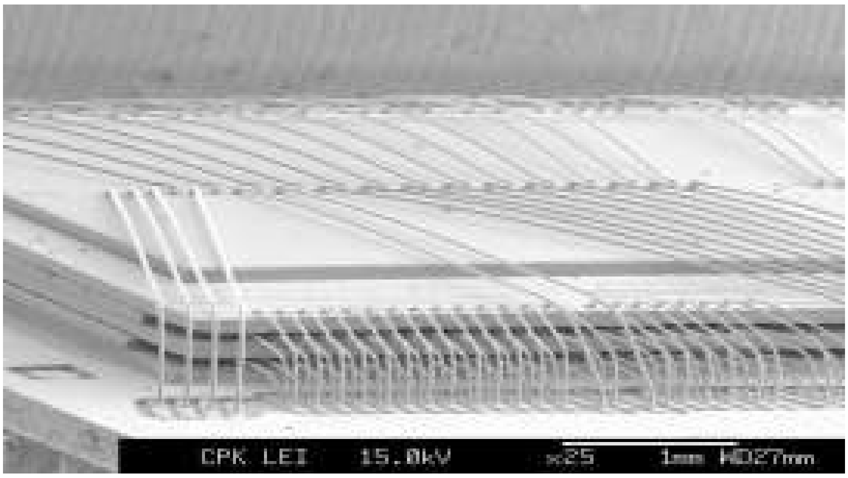

Figure I.1.5: Stack of four dies connected with bonding wires

The oldest and easiest way to connect stacked dies inside the same package is to wire-bond them, as shown in figure I.1.5. In terms of efficiency, however, this is not the best way, as the presence of the bonding wires increases all the parasitic variables inside the circuitry. Many different solutions have been found over the years in order to stack more and more dies on top of each other.

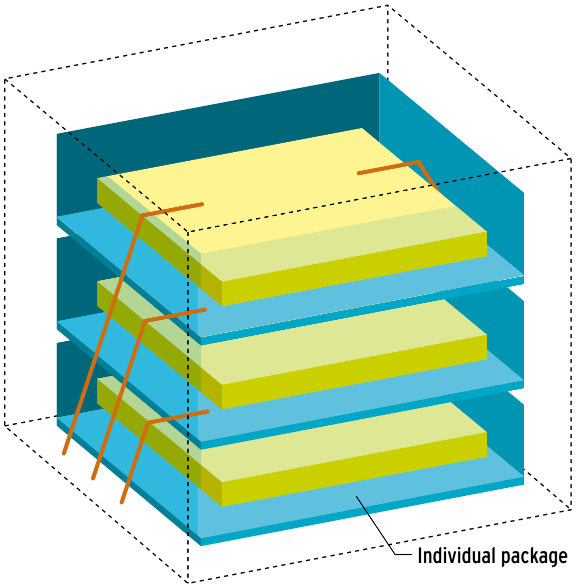

Figure I.1.6: Schematic view of a PiP connected internally through bond wires

A diagram of a possible PiP solution is shown in figure I.1.6.

I.1.4.2 Lateral connections

In this type of configuration, all the connections are performed on the sides of the components [2] [14]. Very often, the single dies (either singularly packaged or not) are bonded to a strap layer, often consisting of a PCB. The PCBs of all the layers are then connected to their sides vertically.

Sometimes, as shown in figure I.1.8, the vertical connection can be established on the external side through an IC directly connected to the lateral connections.

I.1.4.3 Solder bump interconnections

In some cases, two or more dies can be simply connected to each other through solder bump, in a flip-chip configuration [15]. Even though this technique does not allow for stacking a huge number of dies, it is quite widely used as it is reliable and relatively easy to put in place. An example is shown in figure I.1.9.

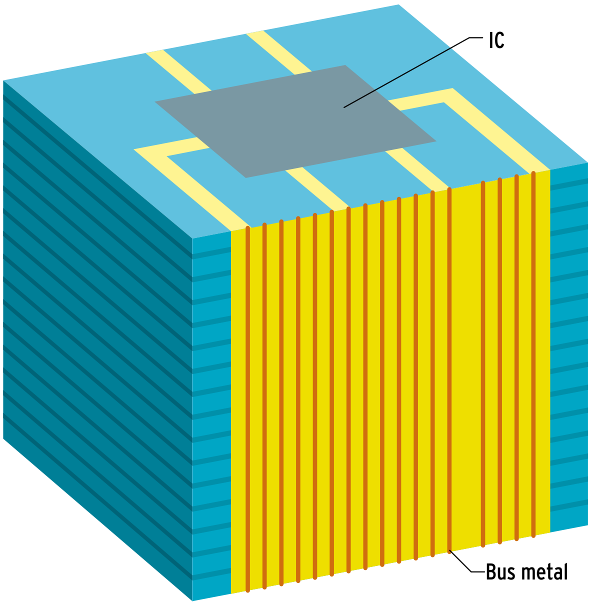

Figure I.1.7: Vertical connection on the external sides of the package

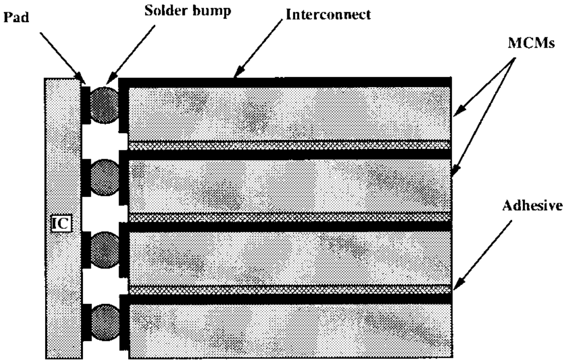

Figure I.1.8: Vertical connection through an additional vertical die

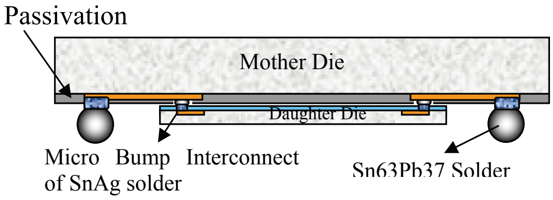

Figure I.1.9: Vertical connection through solder bumps

I.1.4.4 Through Silicon Vias (TSV)

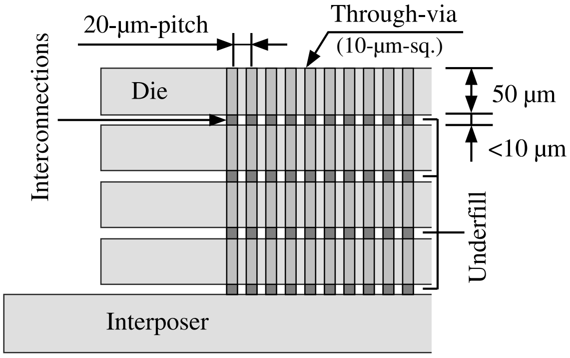

Figure I.1.10: Vertical connection with Through Silicon Vias

The latest technique used for vertical connections is the Through Silicon Via [16][17]. An example from [18] is shown in figure I.1.10. The silicon dies are pierced through their substrate, and filled with metal [19]. Then direct vertical connections are possible by aligning dies directly on top of each other, only divided by a small insulating spacer. There are plenty of different techniques to build such connections, and the precise description of all of them would be off topic in this work. What is interesting here are the common added values of such technology, as it allows for the best performances: the length of the interconnections is minimized, together with the parasitic resistances and capacities. Therefore, speed and frequency are considerably increased.

At this stage of development the main drawbacks are yield and reliability. These problems have not yet been fully resolved.

I.1.5 Conclusion

The list of technologies showed in this chapter is not exhaustive. The aim was to show how three-dimensional components are possible today. Almost every manufacturer has its own technique for stacking dies, and a full set of different names are used. The result is that a study of different technologies is needed to better understand the needs in terms of Failure Analysis and reliability, which is the subject of this document. In fact, the Failure Analysis of 3D components is challenged by a large range f different technologies used to create the packages, and each of them chould be considered separately; an example of the problems that can be expectes is shown in [20].

Before moving on to the specific Failure Analysis challenges posed by 3D devices, it is mandatory to look at the general FA process, and at those techniques which could have an application in this domain, in order to determine what is lacking and hence needs to be developped.

CHAPTER I.2

Failure analysis and reliability

An electronic component can manifest a defect during its entire life: whenever this happens, a precise Failure Analysis needs to be performed. During the design stage, for example, it is needed in order to debug any possible design mistake or technological issue. In this scenario, the understanding of the root cause of the defect is necessary to make the right modifications and get a functional device.

As it is easily understandable, even the components which are already released on the market can fail due to defects: they are generally divided in "early stage", "random" and "end of life" failures [21]. In figure I.2.1 the qualitative curves for the failure rates due to the three different factors is shown.

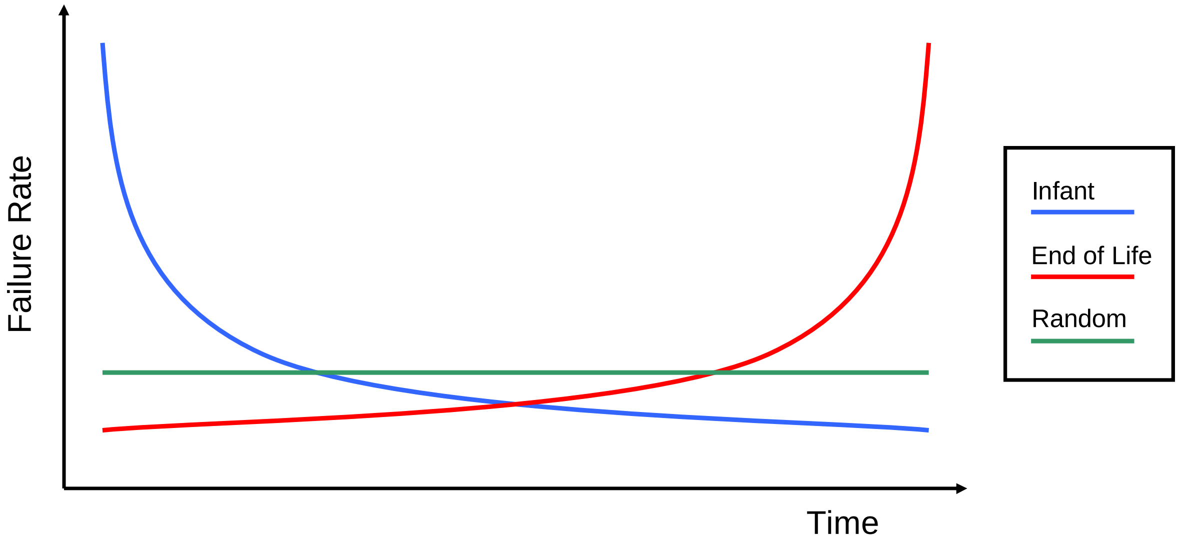

Figure I.2.1: Failure rates

Early stage failures are those which are usually referred to as infant mortality, as they appear in the very first moments of the life of the product. Their failure rate is therefore very high in the beginning, and quickly decreases after that, as shown by the blue curve of figure I.2.1. They are mostly due to failed processes or assembly. It is in fact possible to reduce the rate of these failures by increasing the design tolerances, or by decreasing the product specifications. This type of failure has to be avoided, as it results in the customer receiving an already defective part. It is possible therefore to apply a "screening" process and ageing the parts up to the point where the failure rate is low enough.

Random failures, shown in green in figure I.2.1, are not avoidable. They can arise from a large number of different factors which cannot be controlled.

Finally, the failures represented in figure I.2.1 with a red curve are due to the end of life of the product: in fact they occur more frequently with time, and become significant after the device reaches its End of Life (EoL).

The sum of the three curves explained above gives the total failure rate of the component. It is usually referred to as the "Bathtub curve", and is shown in figure I.2.2.

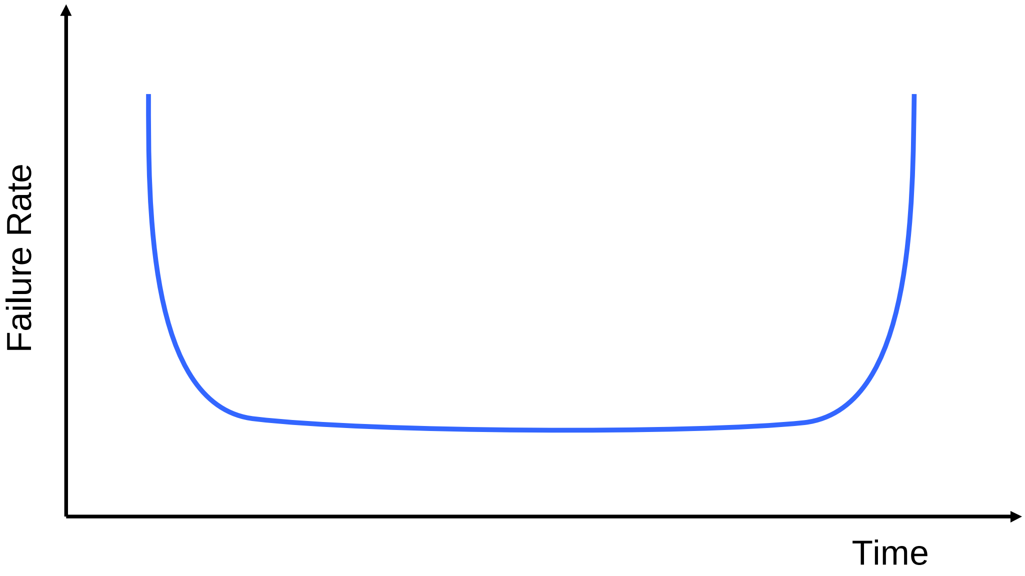

Figure I.2.2: Bathtub Curve

The figure shows how the higher failure rate occurs in the areas representing the early stage and the end of life; the component is then most reliable in the middle part of the curve, which therefore represents the period of its usefulness.

I.2.1 Failure Analysis outcomes

When a failure occurs, it is necessary to analyze it in order to understand its cause, and therefore increase the reliability of future products. Starting from the results of a successful Failure Analysis, it is possible to plan a corrective action which in turn can result in [22]:

- Correcting design errors
- Shortening product development
- Increasing yield
- Reducing the failure rate

Therefore the aim of the analyses is to increase the overall reliability, e.g., move downwards the curve of figure I.2.2.

I.2.2 Failure Analysis process flow

A good analysis always starts with the understanding of the problem: the failure mechanisms which intervene also depend on the zone of the Bathtub curve in which the component is situated [23]. There is an infinite set of possible failure modes which are due to a very broad range of possible defects. Finding the right solution to the particular problem is not a simple task: there is no right process which can be repeatedly applied for each case study. As explained by Ferrier in [24], there is not a single process flow which can be applied every time, but more a general scientific method metaprocess which in turn can generate the right particular process for the case under study.

For the purpose of clarification, however, it is not impossible to illustrate an example of process flow which is abstract enough to be applicable to a wide set of analyses. It will be shown here to define the different steps and the different techniques most widely used by failure analysts. In figure I.2.3 an example of process flow is shown.

Once an electronic component is found to be defective, the first step is that of reproducing the failure in the FA laboratory. To do that, a more or less extensive electrical test is performed. The electrical characterization is needed for different reasons: first of all, the failure has to manifest itself on the analysis site. Furthermore, the electrical signature of the defect gives relevant information regarding the failure itself. More precisely, it is possible to understand if the defect is logical, short or open circuit. In many cases the abnormal behavior of the device manifests itself only in a determinate bias mode: this information is vital then for using localization techniques in the right way.

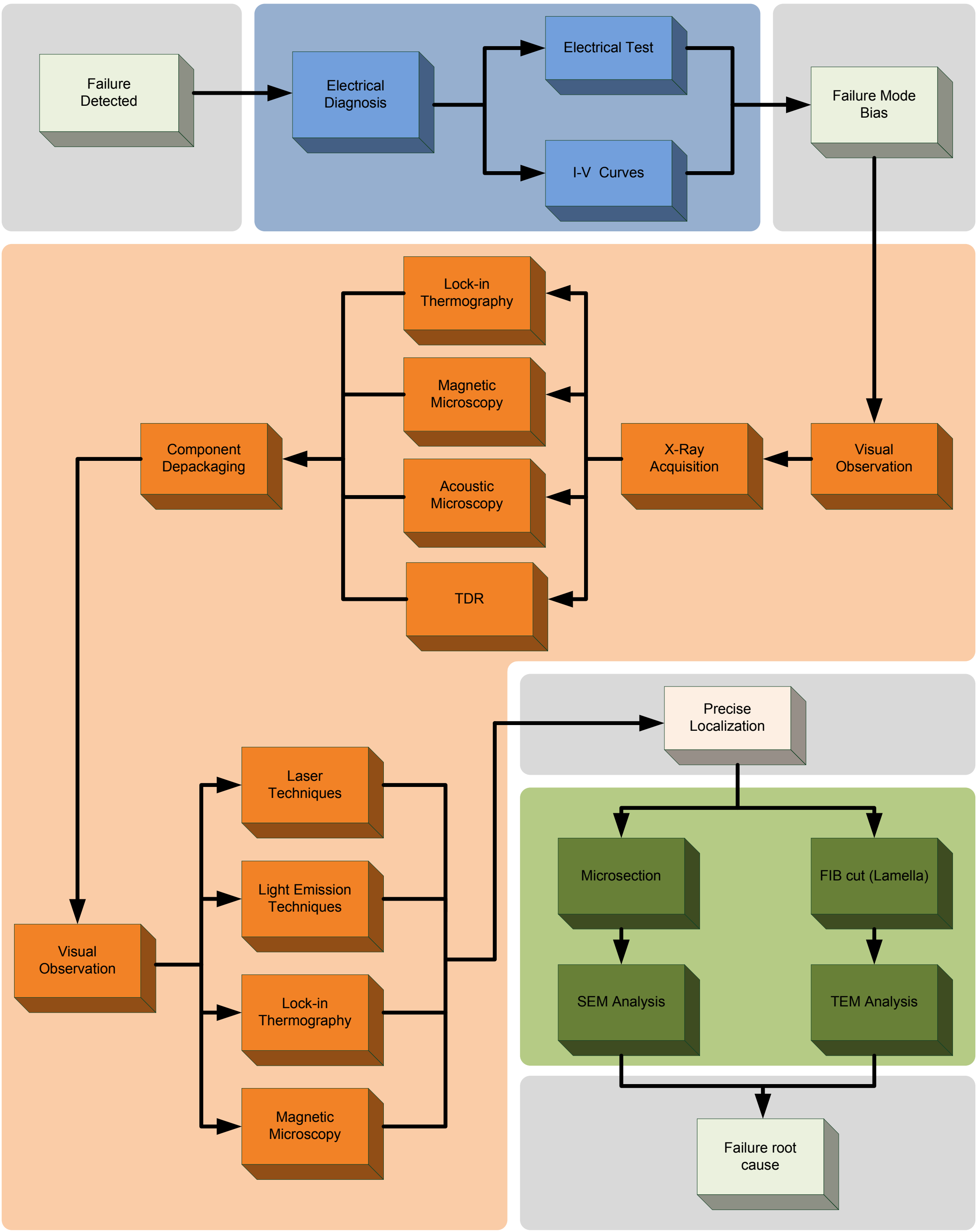

Figure I.2.3: Failure Analysis Process Flow

An optical inspection then is performed, followed by an X-Ray acquisition. The optical inspection gives information about the shape of the sample, so that the right de-packaging technique can be used later on in the process. The pictures taken in this step will also be used coupled together with some localization techniques. The X-ray acquisition is a fundamental part of the initial process of examining the internal structure of the sample, as for example the shape of the lead frame, the number of dies or the position of the dies. In case a decapsulation technique needs to be used, this acquisition is also needed to know how to proceed with the de-packaging process.

The next step is to perform the actual defect localization. For this purpose, a wide range of techniques can be used. They will be explained in more detail in the next chapter. The first step of failure localization is performed by using one or more of the techniques which do not require any sample de-processing, so that any defect at assembly level is not lost.

Component de-packaging is therefore performed by keeping in mind the first results obtained by localization techniques. The part can be opened either on frontside or on backside. The backside analysis allows for a better application of some localization techniques, but is more complex to perform. The X-Ray acquisition previously obtained also gives the information relevant to the die position, and therefore to the right de-processing steps to apply. Following this, a further visual observation is used to gather information about the surface of the die.

In this phase, one face of the bare die is exposed, and more precise localization techniques, such as laser or light emission, can be used. Also the same techniques used before, such as thermal or magnetic techniques, can be re-used now to get a better spatial resolution.

At this point, the defect is precisely localized. In order to verify the localization, the die has to be de-processed. Two different possibilities are available: a simple cross section, followed by a Scanning Electron Microscope (SEM) analysis, or a FIB (Focused Ions Beam) cut used to extract a lamella, which in turn will be analyzed with a Transmission Electron Microscope (TEM) to get a better resolution. This final inspection will contribute to the understanding of the root cause of the failure, which is the main goal of the failure analyst.

So far, the big challenge of defect localization has been outlined, as well as the complexity of interconnections in three-dimensional packages. The next step is to look at possible techniques, which are usually applied at package level, and which have been adapted to 3D defect localization.

CHAPTER I.3

Defect localization techniques

Failure Analysis for electronic technologies can be a very complex task. It has to take into account a huge number of parameters, like, for example, transistor sizes and voltage levels, in order to adapt to find the right solution for the right failure. This means that every case is unique, and has to be treated accordingly. That is why, depending on the type of failure and on the type of circuit, a number of techniques has been developed.

There are different types of localization techniques, which use different physical phenomena in order to extract information from the defective device. The techniques can be classified in several different ways by taking into account different parameters. A classification example could be that of separating them into those directly linked to the electrical behavior of the device, and those which are not. Or, they can be divided into non-destructive, semi-invasive and destructive techniques. For the purpose of this document, the decision was taken to separate the techniques according to the possibility to apply them to three-dimensional components. In this chapter a brief description of the most commonly used techniques for three-dimensional components will be given. For the other techniques, the reader can find plenty of literature elsewhere. A good and complete collection of documentation for Failure Analysis techniques can be found in [25].

The techniques described in this chapter are those related to package level defect localization which can be applied to three-dimensional devices. If the defect is located at die level, it is possible to go back to a more standard process, as described in the previous chapter.

I.3.1 Scanning Acoustic Microscopy

The Scanning Acoustic Microscope (SAM) is used for non-destructive detection of cracks and delaminations at package and assembly level [26]. It can be used for various types of assembly techniques, from wafer bonding to flip-chip. It uses the acoustic waves to image the materials inside the packages. The ultrasounds can in fact be transmitted through materials when light cannot. To do that, a piezoelectric transducer is used in order to transform an electric signal into a mechanical wave. In order to couple the transducer itself and the Device Under Test (DUT), the sample is immersed inside de-ionized water. The piezoelectric transducer is then coupled with a spherical lens which is used to focus the waves in one single spot, as shown in figure I.3.1. The best attainable resolution with this technique has been reported [27] to be in the order of the tens of nanometers.

I.3.1.1 SAM setup

In the simplest setup, the transducer is also a sensor for the waves: for the microelectronics applications, the used frequencies are in the range of $15-300MHz$. The ultrasonic energy is emitted as a short duration pulse, which presents an infinite spectre of frequencies distributed in a Gaussian shape [28]. There are three different setups which can be established for the use of the acoustic microscope: A-scans, B-scans and C-scans. The three of them can be used in the same analysis to obtain more information.

A-scan

The A-scan, shown in figure I.3.2, consists in placing the transducer on top of a fixed point of the Device Under Test (DUT). The emitted signal is partly reflected and partly transmitted on the internal surfaces of the circuit. The acquisition of the reflected waves at the transducer level gives the information of the depth of the surfaces, once the wave velocity is known. It is therefore possible in this way to measure the thicknesses and to set the transducer focus.

B-scan

The B-Scan is a virtual cross-section of the DUT. It is performed by plotting together a series of A-Scans on a line by using gray scale imaging, as shown in figure I.3.3. This scan is very effective to reveal die tilts, or to determine whether some defects on the surface of the sample are interfering with the acoustic signals.

C-scan

Finally, the C-Scan is used to obtain information about a single horizontal plane inside the sample, as shown in figure I.3.4. The basic idea is that of filtering in the time domain just one part of the signal

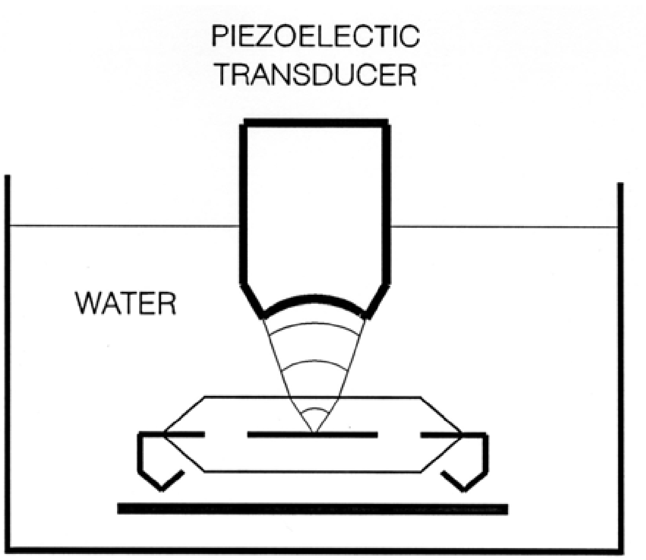

Figure I.3.1: Scanning Acoustic Microscopy setup

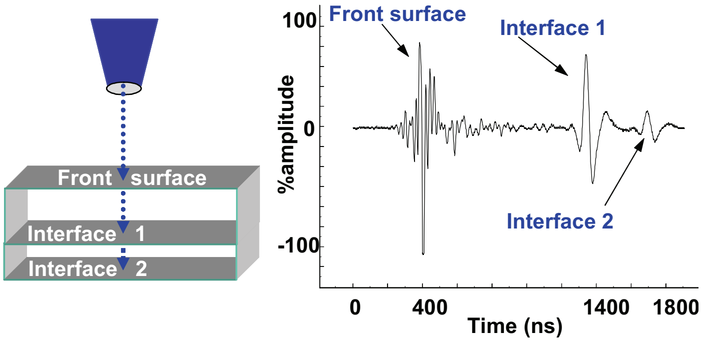

Figure I.3.2: Setup for A-Scan [26]: the wave reflected at each interface is acquired so that the depth of each surface is evaluated

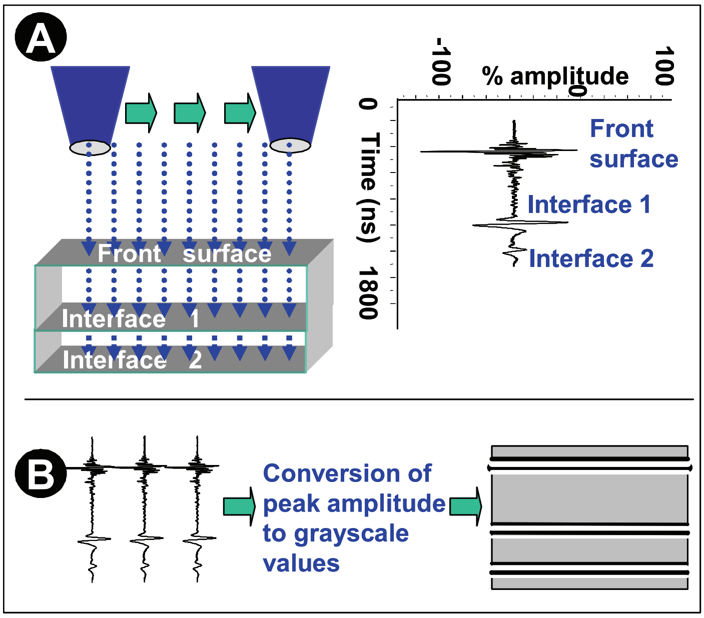

Figure I.3.3: Setup for B-Scan [26]: it consists of a sequence of A-Scans performed on a line of points on top of the sample. The reconstructed image is a virtual cross-section.

obtained by the A-Scan. The gated time then represents a specific surface at a certain depth. The scan is performed on an x-y surface in order to obtain a bi-dimensional map of the desired object.

I.3.1.2 SAM applications

This technique is used for localizing mostly packaging defects. It is principally used for the verification of the different connection for the presence of voids or delaminations. It can therefore be used to study the adherence of the different materials on the die, and to verify the characteristics of the materials, like elasticity and homogeneity. In figure I.3.5 an example of the application of Scanning Acoustic Microscopy for the localization of delaminations is shown.

I.3.1.3 Picosecond SAM

When a laser beam pulse is directed at the surface of an Integrated Circuit, several different phenomena appear. The most common ones are the photo-electric and the thermic carrier generation, which are used by a number of localization techniques at die level. Furthermore, the interaction of the semiconductor with the beam also leads to a secondary effect: an acoustic pulse is produced. The precise characteristics of the wave depend on the physical parameters of the matter and on the laser pulse. The acoustic wave

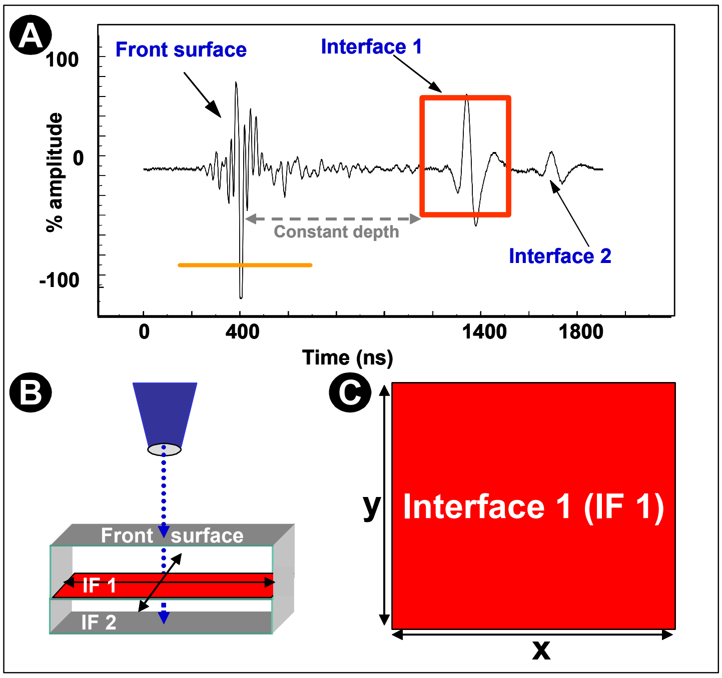

Figure I.3.4: Setup for C-Scan [26]: a sequence of acquisitions is performed on an x-y plane on top of the sample. The acquisitions are then filtered in time so that only one surface is plotted.

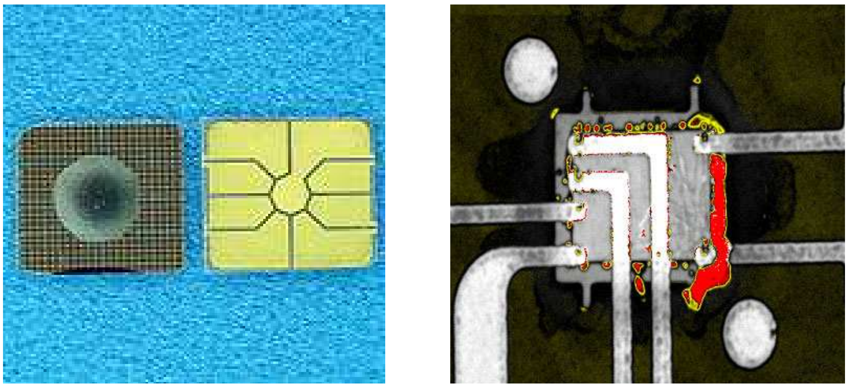

Figure I.3.5: SAM analysis of a microchip [27] propagates as usual in the IC, and is partially reflected at the interfaces. The acoustic wave is able to alter the optical characteristics of the materials locally, so that the optical reflectivity on the surface changes. This variation can be measured by sending a second laser pulse, working in probe mode. The reflected wave of this second pulse is measured with the use of a photodetector [29].

The wavelength of the acoustic wave is in this case in the order of the picoseconds, which allows for a much higher spatial resolution. However, the penetration depth is not significant enough to be able to perform full 3D analyses.

Therefore, one of the big limitations of acoustic microscopy is the trade-off between resolution and absorbtion. High frequency scans give the accuracy needed for 3D (TSV), which is approximately $10\mu m$ in all directions (x, y and z), but it also results in higher absorption, making the analysis of thick 3D systems impossible.

I.3.2 X-Ray Microscopy

One of the most powerful imaging systems for Failure Analysis is X-Ray microscopy. This kind of equipment, which is widely used in other fields (like medicine), is very useful to visualize the internal structure of the sample.

I.3.2.1 Physical principles

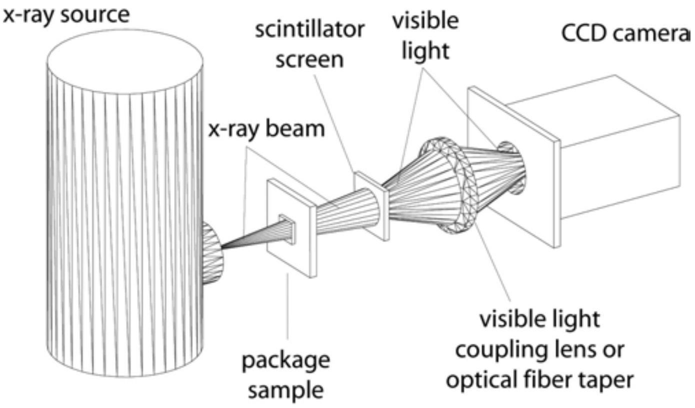

Figure I.3.6: Typical X-Ray System [30]

In figure I.3.6 a typical projection imaging system is shown. The X-Ray radiation is produced by the source and transmitted through the sample. The radiation is projected to a detecting system, typically composed of a scintillator screen, an optical coupling and a CCD camera. The X-Ray source, typically a tungsten bar, is bombarded with high energy electrons. The tungsten core therefore generates a radiation in the wavelength of the nanometer.

The resolution which can be achieved with this technique depends on two main factors: the X-Ray source spot and the detector resolution. As explained by Wang in [30], two different geometrical setups are possible. In the proximity mode, the sample is placed as close as possible to the X-Ray source, there is no optical magnification, and the resolution depends entirely on detector resolution. This approach is the one used for film based radiography, as the recording medium has very high resolution. The problem for this approach is that for Failure Analysis an energy of approximately $50KeV$ is usually needed for the X-Rays to penetrate the packaging materials. In order to get a good detector resolution, the efficiency is usually very low, in the order of 10%.

The other approach, the projection mode, does not need to have a good detector resolution, as the projected image is highly magnified. Therefore, the detector can achieve a high level of efficiency. However, the source spot size needs to be very small. This is the most commonly used mode for most FA commercial tools, and allows for a resolution of smaller than $1\mu m$.

I.3.2.2 Field of application

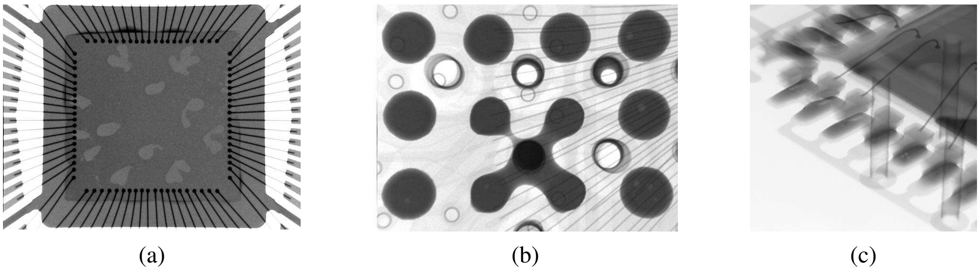
(a) (b) (c)

Figure I.3.7: Examples of X-Ray applications [31]

The possible applications of X-Ray imaging techniques for Failure Analysis are multiple. They are most frequently used to inspect the sample for any packaging defect. In figure I.3.7 some examples are shown. Figure I.3.7a shows a die attach defect, figure I.3.7b a ball-bonding defect, and figure I.3.7c a wire-bonding one. A wide range of further assembly defects can be detected with this technique.

I.3.2.3 Die level X-Ray

In more recent times, X-Ray systems have been developed to increase the imaging resolution up to $30 - 60nm$, allowing its use not only for the failure analysis at package level, but also for detecting defects in the die [32]. Even though the X-Ray analysis cannot reach the high resolution of the SEM/TEM analyses, it has various advantages. The X-rays have in fact a large penetration length, so that no de-processing is needed to visualize the internal structure of the die. Furthermore, the fluorescence emission varies much between different elements, so that it is possible to use this information to obtain high sensitive material analysis.

I.3.2.4 X-Ray Tomography

This application of X-Ray imaging was firstly developed for medical purposes. As X-Rays can penetrate most of the materials, it is straightforward to use this peculiarity to generate a 3D reconstruction of the sample structures. To do that, the sample needs to be imaged at different tilt angles, and a computing algorithm is used to reconstruct the sample. This technology is very useful both to inspect the sample once the defect area is approximately localized, or understand the internal structure of a sample when the CAD information is missing. However, the downside is that the whole process is widely time-consuming: several hours are needed to analyze even a small sample.

Once the three-dimensional structure is built by the software, it will be possible to create virtual cross-sections, or sample delayering in a non-destructive way. An example of a cross-section is shown in figure I.3.8.

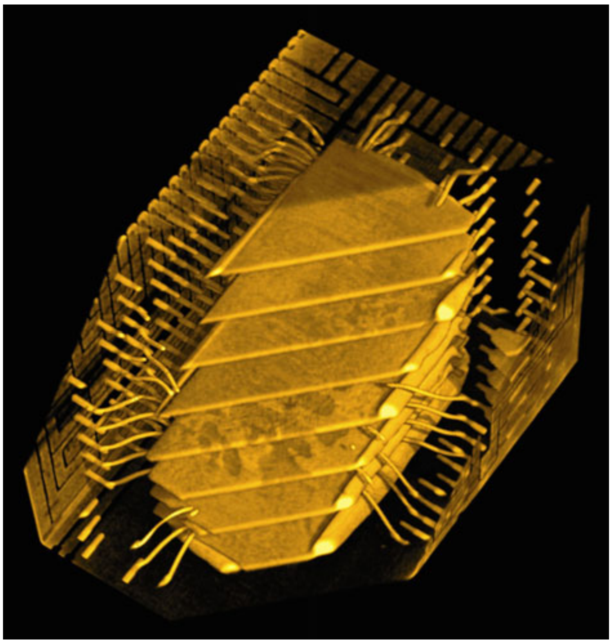

Figure I.3.8: Virtual cross section of a three-dimensional die stack [30]

In this way it is also possible to visualize in three dimensions many assembly defects like voids or shorts in soldering joints, as shown in figure I.3.9

This technique is applicable to 3D defects, but one of the big challenges is where to start looking for them. If a complex SiP contains tens of thousands of interconnections (balls, TSVs, ...) it becomes impossible to locate the defect related to the abnormal electrical behaviour. This is why there is a need for defect localization techniques able to link the physical defect position in the three-dimensional structure and the abnormal electrical behaviour of the analyzed defect.

I.3.3 Time Domain Reflectometry (TDR)

The most common effects of defects are short and open circuits. Time Domain Reflectometry is a powerful technique able to localize them at package level by sending an electric pulse to the sample and reading the resulting reflected wave. It was firstly developed to localize defects inside long cables. It has since been adapted to find defects on electronic devices.

A TDR system is composed of a pulse generator, a probing or fixturing setup, an analysis software and a very large band oscilloscope. In order to localize the defect with better resolution, the electrical setup needs to be adjusted so that every part is of very high quality. The usual TDR instrument is an oscilloscope which can generate a pulse with a very short rising time.

I.3.3.1 Physical principle

The typical TDR setup is shown in figure I.3.10. The TDR instrument is connected through adapted cables and probes/fixtures to the DUT. In order not to filter the higher frequencies of the high frequency pulse, cables and connectors need to be of very high quality. The step waveform sent to the DUT partly propagates through the system and partly is reflected at each impedance discontinuity. The signal which will be measured by the oscilloscope will be the superposition of all the reflected waves.

The electrical diagram of figure I.3.11 represents the equivalent circuit for a TDR system. The cables used to connect the DUT need to be adapted to the internal resistance of the oscilloscope: they both have a 50Ω impedance. In this way the reflected wave at the cable/DUT interface is minimized, and it is therefore easier to discriminate the wanted signal. As the internal impedance of the DUT is unknown, and mostly varies at several intersections, there will always be a first reflected wave at the cable/DUT interface. Its amplitude will be half that of the incident wave, while its duration will be that of the time the wave takes to go to the end of the cable and back, as it is shown in figure I.3.12. Then, depending on the impedance of the DUT, the rest of the wave can be reflected back (open circuit), or there could theoretically be no other reflected wave (short circuit). In reality, there is a wide range of possibilities, and the reflected wave amplitude can vary between $0V$ and the amplitude of the incident wave.

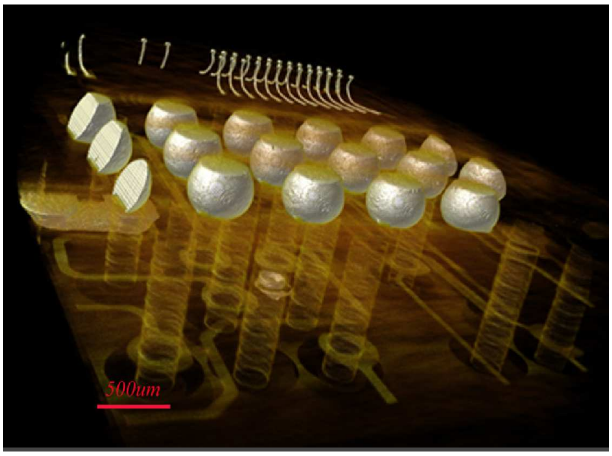

Figure I.3.9: X-Ray tomography reconstruction of solder balls [33]

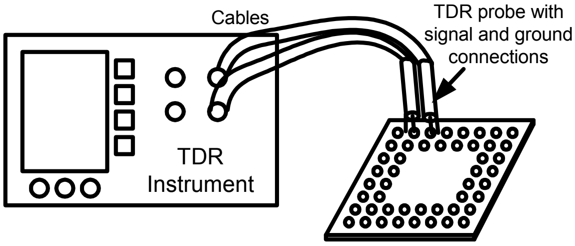

Figure I.3.10: Example of a TDR electrical setup [34]

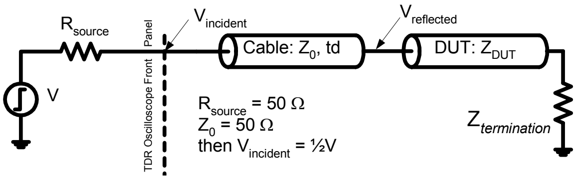

Figure I.3.11: Equivalent circuit of a typical TDR electrical setup [34]

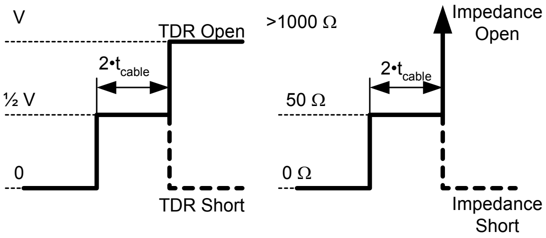

Figure I.3.12: TDR signatures for an open and a short circuit [34]

Once the signal arrives to the oscilloscope, it is converted from a voltage wave to impedance and delay values. These are the important parameters which are used to extract the information about the defect location, and therefore they influence the resolution of the technique.

I.3.3.2 Interconnect analysis

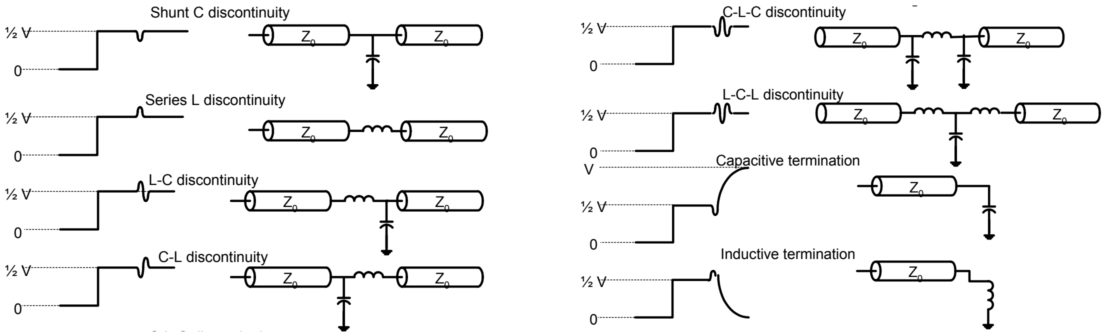

Figure I.3.13: TDR interconnect analysis [34]

Thanks to the analysis of the reflected wave, it is not only possible to detect shorts and opens, but also other types of L, R and C signatures. In figure I.3.13 some examples are shown. However, the fact that the incident signal after the interconnections might be severely filtered has to be taken into account, and any discontinuity coming after the measured ones are not easily interpreted.

I.3.3.3 Multiple reflections

Once the signal is sent to the DUT, there is no reason for the device not to have multiple impedance discontinuities inside. As shown in figure I.3.14, each of the discontinuities generates an incident wave and a reflected wave. All the reflected waves are then added up, so that the measured signal is a combination of all the reflected waves. Furthermore, the reflected waves can be treated themselves as incident waves: when they travel back towards the oscilloscope, they are partly transmitted and partly re-reflected. As a result, the measured waveform is not of easy interpretation without any data analysis. Up to date TDR equipment involves a deconvolution algorithm which provides the so called true impedance profile by separating the single reflected waves from each other.

An example of how the deconvolution algorithm can be very useful to isolate the location of the defect is shown in figure I.3.15. The example refers to a TDR analysis performed on a BGA packaged device showing a open circuit defect. The TDR signature is not precise enough to give the precise location of the open circuit, as more waveforms are added up and confused. However, with the true-impedance-profile method, it is easy to pinpoint the exact location of the open circuit.

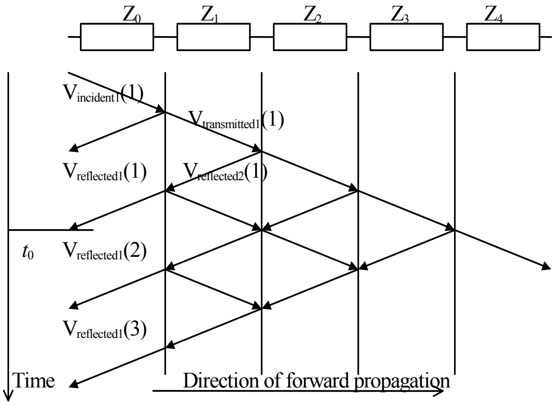

Figure I.3.14: Multiple discontinuities generate multiple reflections [34]

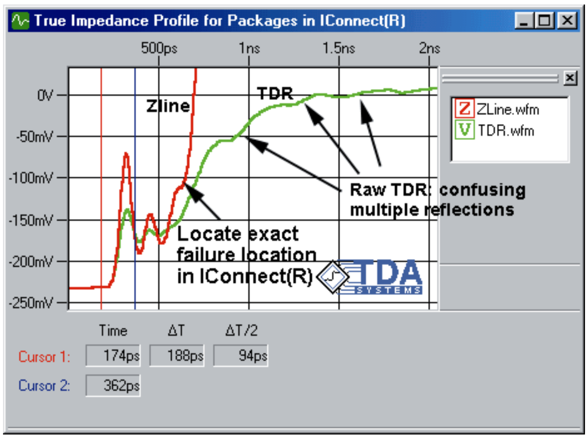

	Time	ΔT	ΔT/2
Cursor 1:	174ps	188ps	94ps
Cursor 2:	362ps		

Figure I.3.15: TDR signature of an open circuit in a BGA package [34]

I.3.3.4 TDR resolution

TDR resolution depends on many parameters. The most important is the rise time of the incident waveform. To isolate two different discontinuities located next to each other, their separation in terms of time has to be at least half of the rising time. Therefore a rising time of $40ps$ would give a resolution of approximately $3mm$. However, in most cases it is needed only to localize a single discontinuity inside the DUT. In this case the time localization can be between 1/10 and 1/5 of the rising time, and a localization accuracy of less than $1mm$, which is not enough for the needed $10\mu m$ target, unless terahertz range TDR is used [35].In addition, TDR only gives the electrical distance (time between echoes and echo shape). The biggest difficulty is to move from the electrical information to the spatial position of the defect.

I.3.4 Lock-in Thermography (LiT)

Thermography techniques use the basic physical principles of Infrared (IR) radiation to measure the actual temperature of a sample spot. As silicon is transparent in IR light, this technique is very useful for detecting hot spots due to a short circuit or a resistive open inside the die.

I.3.4.1 Physical principle

The principle of LiT is that every material has its own emissivity, which is defined as the ratio between the energy radiated by that material with the energy radiated by a blackbody at the same temperature. More information about blackbodies radiation can be found in [36]. The spectral radiance of the blackbodies at temperatures close to the those usually found on electronic components is shown in figure I.3.16.

The peak of the radiance, and therefore that of the emissivity, is in the range of $3\mu m - 12\mu m$. Depending on the temperature range then the right type of camera should be chosen.

When a current flows inside a resistive path, it generates a local heating of the sample which can be detected with an Infrared Camera. The resolution attainable with this technique, as stated in [36], is of the order of $15\mu m$.

I.3.4.2 Lock-in Technology

Lock-in Thermography uses the physical principle of lock-in technology. Instead of applying a static DC voltage to the device, an alternating signal is applied at a so-called lock-in frequency, usually with a duty cycle of 50%, as explained in [37]. This methodology allows for noise reduction in a very sensible way, and therefore for an increase of spatial resolution. While the voltage is applied, the infrared camera acquires images from the sample surface. The images which are acquired are weighed with two different correlation functions, a sinus and a cosinus one. The total signal will be therefore separated in an *in* *phase* and an *out of phase* (with a 90° phase shift) signals, which are called respectively S^{0° and S^{90°, evaluated pixel-wise.

To evaluate the amplitude and the phase signals, the following equations stand:

$$\begin{aligned} Amplitude &= \sqrt{(S^{90^\circ})^2 + (S^{0^\circ})^2} \\ Phase &= \arctan\left(\frac{S^{90^\circ}}{S^{0^\circ}}\right) \end{aligned} \tag{I.3.1}$$

These two signals are very useful if compared to the in phase and out of phase ones. The amplitude phase, in fact, takes into account the difference in the emissivity of the materials due to the change in temperature. What is of fundamental importance is that, by adding together the two signals, the Signal to Noise Ratio (SNR) is sensibly increased. The phase signal is therefore noisier; however, as in this case the two starting signals are divided by each other, the influence of the difference in emissivity for the different materials is eliminated. Therefore both the amplitude and the phase images are used to obtain the localization information. An example of application of this technique is shown in figure I.3.18.

From this picture it can be noted that for the amplitude image there is a strong influence of the emissivity of the different materials which are generating a thermal signal even if they are not locally heated. This effect is completely avoided in the phase image: here the only visible spot is due to a local heating of the device. The phase signal represents the time delay of the thermal heating wave. If this signal is properly studied, it can be used to obtain information about the distance from the hot spot to the source of the wave. Both amplitude and phase signals can then be used to acquire information about the location of the defect.

I.3.4.3 Application to the 3D

As explained in [37] and [39], Lock-in Thermography technique can be used to obtain three dimensional information about the localization of a defect. The thermal source, which is usually a short circuit or a resistive open, is periodically stimulated with an electrical wave. This wave can then propagate through the component and through the molding compound, until it reaches its surface. The package is not usually transparent to the infrared light, but the desired information can be acquired from the diffusion of the thermal wave.

The thermal wave does not propagate in the same way through every material. Its speed depends on the thermal diffusion length, which is defined as the length where the thermal wave amplitude drops to e^{-1}:

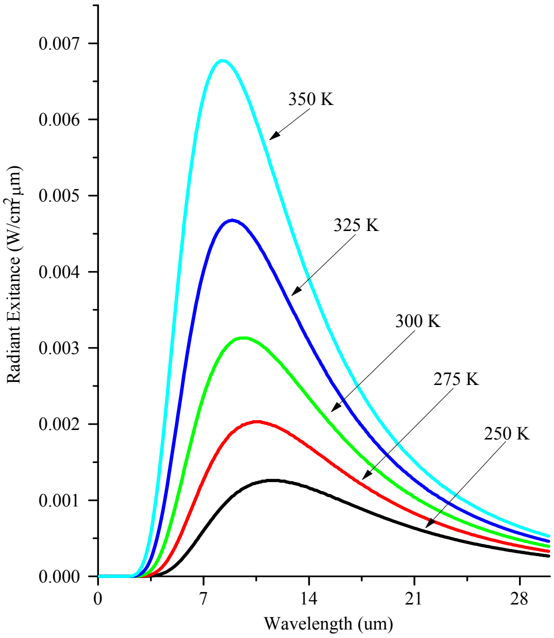

Figure I.3.16: Spectral radiance of the blackbodies [36]

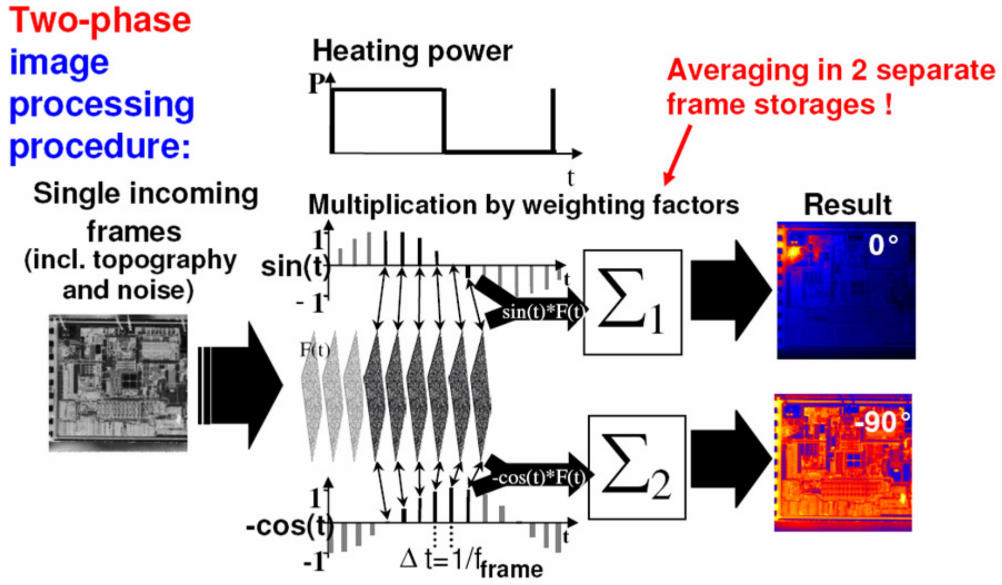

Figure I.3.17: Lock-in signals reconstruction [38]

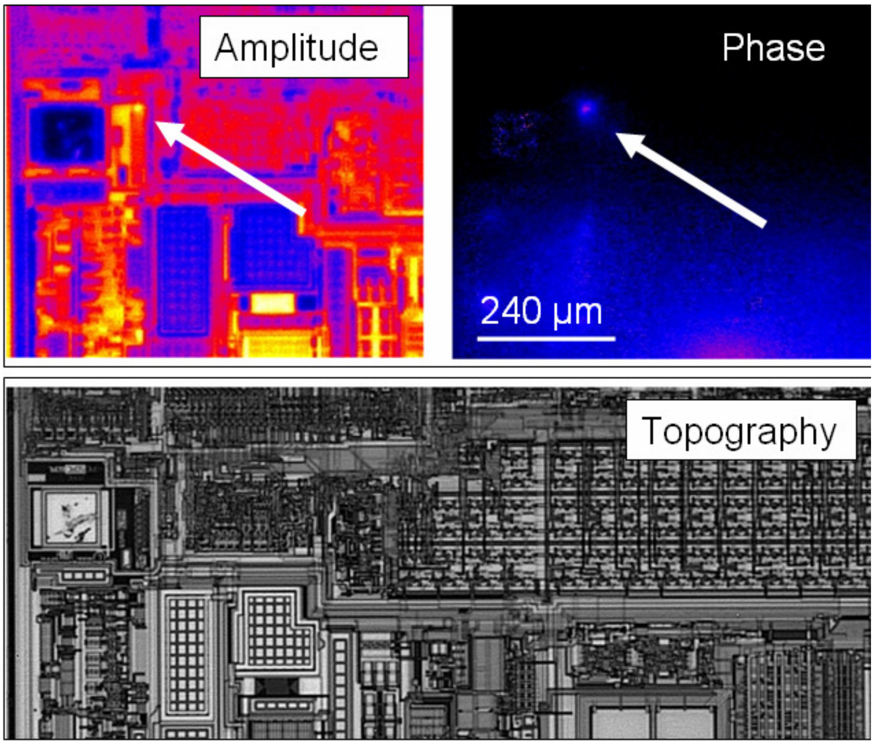

Figure I.3.18: Example of application of Lock-in Thermography [37]

$$\mu = \sqrt{\frac{2\lambda}{c_p \cdot \rho \cdot 2\pi \cdot f_{lock-in}}} = \sqrt{\frac{2a}{2\pi \cdot f_{lock-in}}} \tag{I.3.2}$$

where λ is the heat conductivity, c_p the heat capacity, ρ the density, $f_{lock-in}$ the lock-in frequency and a is the thermal diffusivity. The diffusion length in function of the lock-in frequency for different materials shows how differently the heat propagates, for a given frequency, inside the materials. In figure I.3.19 an example for the silicon and the molding compound is shown.

Once the thermal diffusion length, given by equation I.3.2, is known, it can be used to obtain depth information. The diffusivity affects not only the thermal amplitude, but also the phase. The ratio between the z value and the phase is given by:

$$\Phi = \frac{z}{\mu}\frac{180}{\pi} \tag{I.3.3}$$

The resulting phase shift for a given material, in function of the lock-in frequency is then plotted for both silicon and molding compound in figure I.3.20.

The fitting of the acquired data on real devices with the theoretical curves gives the precise z distance from the heat source, which represents the defect, to the surface of the sample.

Even though defect localization in the third dimension is challenging, LiT appears, like terahertz TDR, to be a potential solution for defect localization. However, it can only be applied to dissipative defects.

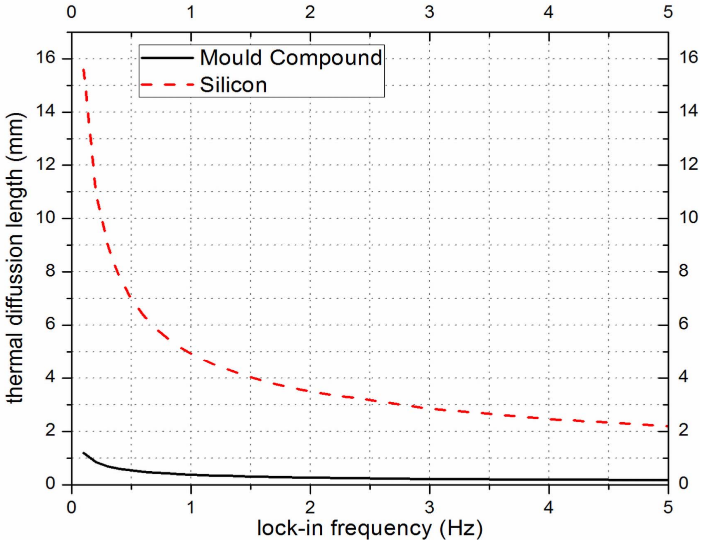

Figure I.3.19: Thermal diffusion length [37]

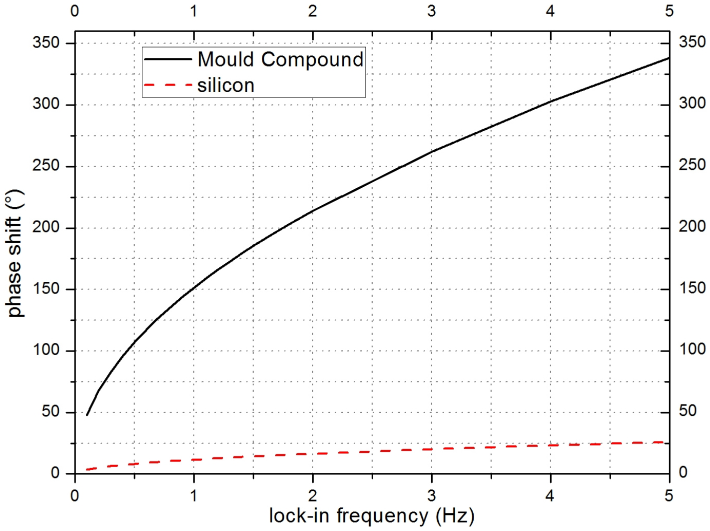

Figure I.3.20: Phase shift in function of the frequency [37]

I.3.5 Magnetic Microscopy

Magnetic Microscopy is a non-destructive technique for failure isolation and localization [40][41]. It uses the property of the magnetic fields which is not shielded by any non-ferromagnetic material, so that useful information can be gathered through both the silicon and the molding compound, without any need to de-package the component. Furthermore, it is a technique which can be used at different levels: at board level, it can be used to map the currents flowing in the different tracks. It can then be used at assembly level, to identify the wrong connections between the die and the lead frame. Finally, it is used to locate faults on the die itself.

As the main work described in this document is based on MM techniques for defect localization, the reader is directed to chapters II.3 and III.2 for further details of this technique.

I.3.5.1 Physical principle

Every time a current flows inside an electrical conductor, it generates a magnetic field according to Biot-Savart's law. Since this field is not shielded by any material used in standard electronic devices, it can be measured above the component. The data post-treatment allows for the magnetic field to be transformed into the map of the magnetic sources. In the case of electronic devices, magnetic sources can be identified as electrical current flows. The map of the current, then, can be used to localize precisely short circuits or resistive opens [42].

The main advantages of Magnetic Microscopy are the direct link between the magnetic field and the current flowing in 3D structures, and the device transparency to the field.

I.3.6 Conclusion

In this chapter, the challenge of defect localization for three-dimensional components has been underlined, with reference to a spatial resolution of $10\mu m$ on the three axes (x, y and z) for devices that could be more than $1cm$ thick. Localization techniques must be able to link the abnormal electrical behaviour to the physical position of the defect and with the mandatory resolution. Three techniques were therefore identified: TDR, LiT and MM. From those, Magnetic Microscopy was selected for its higher versatility, giving a high number of possibilities. In part II, Magnetic Microscopy state of the art related to the 3D defect localization challenge is shown.

Part II

Magnetic Microscopy: State of the art

CHAPTER II.1

Magnetic Fields Theory

II.1.1 Maxwell Equations

To understand magnetic fields theory it is necessary to start with Maxwell equations, which are at the very base of each electromagnetic phenomenon. The two Maxwell equations that refer to the magnetic field are, in their differential form:

$$\nabla \times \mathbf{H} = \mathbf{J} + \frac{\partial(\varepsilon_0 \mathbf{E})}{\partial t} \tag{II.1.1}$$

$$\nabla \cdot \mu_0 \mathbf{H} = 0 \tag{II.1.2}$$

The source of the magnetic field intensity, **H**, is the current density, **J**. For the analysis of the study the case of static magnetic field will be considered, since the electric field is constant during the time. Furthermore, the case of not magnetizable matter is studied, so that the relation between the magnetic field **H** and the magnetic induction **B** is:

$$\mathbf{B} = \mu_0 \mathbf{H} \tag{II.1.3}$$

Under this hypothesis II.1.1 and II.1.2 become:

$$\nabla \times \mathbf{B} = \mu_0 \mathbf{J} \tag{II.1.4}$$

$$\nabla \cdot \mathbf{B} = 0 \tag{II.1.5}$$

Equation II.1.4 is usually also referred to as the Ampere's law. In the case of static magnetic fields, and in no magnetizable matter, the laws II.1.4 and II.1.5 uniquely determine the magnetic induction field **B**. From equation II.1.5, this is solenoidal at all space.

II.1.2 The law of Biot-Savart

One of the ways to find the solution of equation II.1.5 is that of using a potential approach:

$$\mathbf{B} = \nabla \times \mathbf{A} \tag{II.1.6}$$

where **A** is the *vector potential*. The vector potential is invariable with respect to the sum with a gradient of any arbitrary function: it is possible to modify the equation II.1.6 as follows:

$$\mathbf{A}' = \mathbf{A} + \nabla\psi \tag{II.1.7}$$

The curl of **A** is in fact the same as the curl of **A**′. It has been proven on[43] that to uniquely specify a vector field both its curl and its divergence must be given. The divergence of **A** can be chosen according to the specific needs of the application. It is a convenient convention to make the vector potential solenoidal:

$$\nabla \cdot \mathbf{A} = 0 \tag{II.1.8}$$

It is possible then, from Ampere's law, to evaluate **A** and consequently **B**. Substituting II.1.6 into II.1.4 gives:

$$\nabla \times (\nabla \times \mathbf{A}) = \mu_0 \mathbf{J} \tag{II.1.9}$$

Since the following identity holds:

$$\nabla \times (\nabla \times \mathbf{A}) = \nabla(\nabla \cdot \mathbf{A}) - \nabla^2 \mathbf{A} \tag{II.1.10}$$

then, having fixed the solenoidality of the vector potential, II.1.9 is reduced to the *Poisson's Equation*:

$$\nabla^2 \mathbf{A} = -\mu_0 \mathbf{J} \tag{II.1.11}$$

The first member of II.1.11 is a vectorial laplacian; thus, each of its cartesian components are scalar laplacians. Therefore the equation II.1.11 is equivalent to three scalar Poisson's equations:

$$\begin{aligned}\nabla^2 A_x &= -\mu_0 J_x \\ \nabla^2 A_y &= -\mu_0 J_y \\ \nabla^2 A_z &= -\mu_0 J_z\end{aligned} \tag{II.1.12}$$

As an example, the solution of the equation for the z component will be discussed here.

In cartesian coordinates, from the expressions of the divergence and gradient operators, it follows that:

$$\frac{\partial^2 A_z}{\partial x^2} + \frac{\partial^2 A_z}{\partial y^2} + \frac{\partial^2 A_z}{\partial z^2} = -\mu_0 J_z \tag{II.1.13}$$

To find the solution of Poisson's equation for any given current density J_z, the superposition principle will be used. It is possible to represent the current density J_z as the sum of a number of elementary contributions. Therefore the cartesian space is divided into elementary volumes $dx' \cdot dy' \cdot dz'$. These elements will then be the center of the cartesian coordinates (x', y', z'), as shown in figure II.1.1.

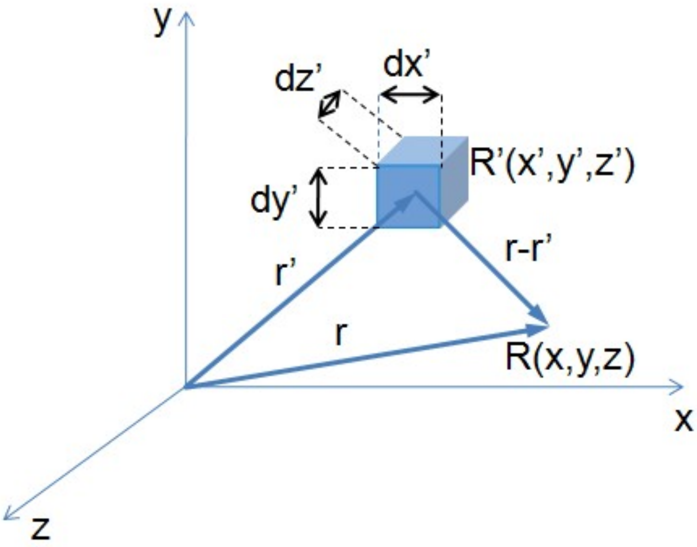

Figure II.1.1: Different coordinate systems

Thus, considering a generic current distribution:

$$dA_z(\mathbf{r}, \mathbf{r}') = \frac{\mu_0 J_z(\mathbf{r}')}{4\pi \left|\mathbf{r} - \mathbf{r}'\right|} dv \tag{II.1.14}$$

where

$$\left|\mathbf{r}-\mathbf{r}'\right| = \sqrt{(x-x')^2+(y-y')^2+(z-z')^2} \tag{II.1.15}$$

Equation II.1.14 depends on two sets of Cartesian coordinates: (x, y, z), which refers to the point $\mathbf{r}$ at which the potential is evaluated and (x', y', z') which refers to the point $\mathbf{r}'$ at which the elementary current is positioned. In order to obtain the potential, the differential potential generated by the elementary currents need to be added together in the (x, y, z) reference system. The sum of the differential potential becomes a volume integral over the coordinates (x', y', z'):

$$A_z = \frac{\mu_0}{4\pi}\int_{V'}\frac{J_z(\mathbf{r}')}{|\mathbf{r}-\mathbf{r}'|}dv' \tag{II.1.16}$$

The same conclusion can be derived for the other two equations. In order to obtain the complete vector potential $\mathbf{A}$, then, it is needed to add the three components A_x, A_y and A_z, all multiplied by their respective unitary vector, i_x, i_y and i_z:

$$\mathbf{A}(\mathbf{r}) = \frac{\mu_0}{4\pi}\int_{V'}\frac{\mathbf{J}(\mathbf{r}')}{|\mathbf{r}-\mathbf{r}'|}dv' \tag{II.1.17}$$

Once the vector potential has been determined from the superposition integral, the magnetic flux density follows from an evaluation of the curl of $\mathbf{A}$. The field superposition integral follows by operating on the vector potential as given by II.1.17 before the integration has been carried out:

$$\mathbf{B} = \nabla\times\mathbf{A} = \frac{\mu_0}{4\pi}\nabla\times\int_{V'}\left[\frac{\mathbf{J}(\mathbf{r}')}{|\mathbf{r}-\mathbf{r}'|}\right]dv' \tag{II.1.18}$$

While the integration is with respect to the source coordinates denoted by $\mathbf{r}'$, the curl is applied on the (x, y, z) coordinates. Therefore it is possible to exchange the order of the curl and integration operations, so II.1.18 becomes:

$$\mathbf{B} = \frac{\mu_0}{4\pi}\int_{V'}\nabla\times\left[\frac{\mathbf{J}(\mathbf{r}')}{|\mathbf{r}-\mathbf{r}'|}\right]dv' \tag{II.1.19}$$

The curl is therefore applied to the product of the vector $\mathbf{J}$ and the scalar:

$$\psi = \left|\mathbf{r}-\mathbf{r}'\right|^{-1} \tag{II.1.20}$$

The following vectorial identity holds:

$$\nabla\times(\psi\mathbf{J}) = \psi\nabla\times\mathbf{J} + \nabla\psi\times\mathbf{J} \tag{II.1.21}$$

Since $\mathbf{J}$ is independent from $\mathbf{r}$, the first term of the right member is zero. Thus, II.1.19 becomes:

$$\mathbf{B} = \frac{\mu_0}{4\pi} \int_{V'} \nabla\left(\frac{1}{|\mathbf{r} - \mathbf{r}'|}\right) \times \mathbf{J} dv' \tag{II.1.22}$$

The best way to evaluate the gradient of II.1.22 is to use spherical coordinates, as the vector $\mathbf{r}$ is very easily represented when the origin of this system is $\mathbf{r}'$:

$$\nabla(1/r) = -\frac{1}{r^2}\mathbf{i}_r \tag{II.1.23}$$

being $\mathbf{i}_r$ is the unit vector. By changing the center of the reference system to the arbitrary location $\mathbf{r}'$, the distance r in II.1.23 is replaced by $|\mathbf{r} - \mathbf{r}'|$. The new unit vector will then be defined as $\mathbf{i}_{r'r}$. In this case II.1.23 becomes:

$$\nabla\left(\frac{1}{\mathbf{r} - \mathbf{r}'}\right) = -\frac{\mathbf{i}_{r'r}}{|\mathbf{r} - \mathbf{r}'|^2} \tag{II.1.24}$$

The combination of the equations II.1.24 and II.1.22 gives the *Biot-Savart Law* for the magnetic induction field:

$$\mathbf{B} = \frac{\mu_0}{4\pi} \int_{V'} \frac{\mathbf{J}(\mathbf{r}') \times \mathbf{i}_{r'r}}{|\mathbf{r} - \mathbf{r}'|^2} dv' \tag{II.1.25}$$

which in differential form becomes:

$$\mathbf{dB} = \frac{\mu_0}{4\pi} \frac{\mathbf{J}(\mathbf{r}') \times \mathbf{i}_{r'r}}{|\mathbf{r} - \mathbf{r}'|^2} dv' \tag{II.1.26}$$

II.1.3 Conclusion

In this chapter the possibility to extract the magnetic field B from the current density J has been demonstrated. The problem to be addressed now is the opposite: is it possible, by measuring the magnetic field, to rebuild J? This will be investigated in the next chapter.

CHAPTER II.2

The inversion of the magnetic induction field

From the theory on magnetic fields it has been proven that, in the quasi-static case, starting from the knowledge of the current distribution over all the space, it is possible to univocally evaluate the magnetic induction field. This can be performed through the use of the Biot-Savart law, and it has been referred to by Roth et al. in [44] as the forward problem. The magnetic inverse problem, on the contrary, involves obtaining the current distribution starting from the knowledge of the magnetic induction field. The inverse problem is not of easy solution; it can be proven that its solution is not unique unless a certain number of hypotheses are taken into account. To perform the inversion, a number of approaches has been studied, as shown in [45]. The most common application of the magnetic approach is the detection of flaws in metal layers, such as hidden cracks or corrosion. This technique consists on injecting in the metal plate some eddy currents; these will vary their distributions depending on the metal geometry, and so the magnetic field generated by them. The study of the magnetic field can therefore reconstruct the flows inside the metal layers. The inversion techniques for this type of application take advantage of the formulation of the Biot-Savart law in terms of the curl of the current distribution as follows:

$$\mathbf{B}(\mathbf{r}) = \frac{\mu_0}{4\pi}\int_S \frac{\mathbf{J}(\mathbf{r}')\times\hat{\mathbf{n}}}{|\mathbf{r}-\mathbf{r}'|}d^2r' + \frac{\mu_0}{4\pi}\int_V \frac{\nabla'\times\mathbf{J}(\mathbf{r}')}{|\mathbf{r}-\mathbf{r}'|}d^3r' \qquad \text{(II.2.1)}$$

where $\hat{\mathbf{n}}$ is the unity vector normal to the surface surrounding the object S, and V is the volume of the object. With this formulation, in the case of eddy currents, the magnetic induction is divided into two main contributions: the first one represents the discontinuity of the tangential component of the current on the surface S, and the second is generated by any curl of the current inside the volume V. This last component is in fact null for each ohmic current contribution, which can be written as the gradient of its potential:

$$\mathbf{J}(\mathbf{r}) = -\sigma\nabla\varphi \tag{II.2.2}$$

and the curl of any divergence is always null.

The inversion problem which will be treated here is different in the sense that the current to be mapped is always a DC or AC ohmic current, which therefore has no contribution in the curl component of equation II.2.1. The inversion technique which is used is called the spatial filtering approach, and it uses a Fourier approach to solve the problem.

II.2.1 The forward problem

Starting from the Biot-Savart law, it is possible to determine the magnetic induction **B** once given the current density **J**. This will later be referred to as the *forward problem*. This step is fundamental to understand how to obtain the current density given the magnetic field.

While the forward problem, once given all the boundary conditions, has a unique solution, it is not the same for the inverse problem. To make unique the solution of the inverse problem, two hypotheses have to be taken into account. The first is that the current density **J** is restricted to a thin layer of thickness d on the $x - y$ plane. Therefore the current distribution will be approximated to as bi-dimensional. Furthermore, it will be assumed that the current is quasistatic, and so its divergence is zero:

$$\nabla\mathbf{J} = 0 \tag{II.2.3}$$

This last hypothesis will make the Biot-Savart law valid as described in the equation II.1.25. This can also be formulated as follows:

$$\mathbf{B}(\mathbf{r}) = \frac{\mu_0}{4\pi}\iiint \frac{\mathbf{J}(\mathbf{r}') \times (\mathbf{r} - \mathbf{r}')}{|\mathbf{r} - \mathbf{r}'|^3} d^3\mathbf{r}' \tag{II.2.4}$$

The magnetic induction field is generally measured on a $x - y$ plane parallel to the plane of the currents. In the following calculations, the distance between the two planes will be z_0, as it is shown in figure II.2.1.

The current distribution is therefore approximated to a planar distribution on the plane $z' = 0$. It follows that the Biot-Savart law of equation II.2.4 can be simplified by carrying out the integration on the z' axis:

$$
\begin{aligned}
\mathbf{B}(\mathbf{r}) &= \frac{\mu_0}{4\pi}\int_{-\infty}^{+\infty}\int_{-\infty}^{+\infty}\int_0^d \frac{\mathbf{J}(x',y')\times(x-x',y-y',z)}{[(x-x')^2+(y-y')^2+z^2]^{3/2}}dx'dy'dz' \\
&= \frac{\mu_0}{4\pi}\int_{-\infty}^{+\infty}\int_{-\infty}^{+\infty}\frac{\mathbf{J}(x',y')\times(x-x',y-y',z)}{[(x-x')^2+(y-y')^2+z^2]^{3/2}}dx'dy'\int_0^d dz' \\
&= \frac{\mu_0 d}{4\pi}\int_{-\infty}^{+\infty}\int_{-\infty}^{+\infty}\frac{\mathbf{J}(x',y')\times(x-x',y-y',z)}{[(x-x')^2+(y-y')^2+z^2]^{3/2}}dx'dy'
\end{aligned}
\tag{II.2.5}
$$

From equation II.2.5, the x component of the magnetic induction field is generated by two components of the cross product: the scalar product of the z component of $\mathbf{r}-\mathbf{r}'$ with the y component of the current distribution, and the scalar product of the y component of $\mathbf{r}-\mathbf{r}'$ with the z component of the current distribution. However, as stated before, the current distribution has been approximated to a two-dimensional one, having no z component. Therefore the only remaining term is the first one:

$$
B_x(x,y,z) = \frac{\mu_0 d}{4\pi}z\int_{-\infty}^{+\infty}\int_{-\infty}^{+\infty}\frac{J_y(x',y')}{[(x-x')^2+(y-y')^2+z^2]^{3/2}}dx'dy' \tag{II.2.6}
$$

Equation II.2.6 can be seen as the convolution between $J_y(x',y')$ and the Green function:

$$
G(x-x',y-y',z) = \frac{\mu_0 d}{4\pi}z\frac{1}{[(x-x')^2+(y-y')^2+z^2]^{3/2}} \tag{II.2.7}
$$

To solve the integral of equation II.2.6 it is best to work in the Fourier space. Indeed, from the convolution theorem, the convolution in the Euclidean space becomes a scalar product in the Fourier space. Therefore, the following identities holding:

$$
\begin{aligned}
b_x(k_x,k_y,z) &= \mathcal{F}\Big\{B_x(x,y,z)\Big\}(k_x,k_y) \\
g(k_x,k_y,z) &= \mathcal{F}\Big\{G(x,y,z)\Big\}(k_x,k_y) \\
j_y(k_x,k_y) &= \mathcal{F}\Big\{J_y(x,y)\Big\}(k_x,k_y)
\end{aligned}
\tag{II.2.8}
$$

being b_x, g and j_y the two-dimensional Fourier transform on the x and y spatial variables of B_x, G and J_y, the convolution product of equation II.2.6 becomes, in the Fourier space:

$$
b_x(k_x,k_y,z) = g(k_x,k_y,z)\cdot j_y(k_x,k_y) \tag{II.2.9}
$$

The two spatial frequencies, k_x and k_y, are the components on x and y of the frequency vector $\mathbf{k}$. Given the transform of Green's function:

$$g(k_x, k_y, z) = \int_{-\infty}^{-\infty} \int_{-\infty}^{-\infty} \frac{\mu_0 d}{4\pi} z \frac{1}{[x^2 + y^2 + z^2]^{3/2}} e^{-i(k_x x + k_y y)} dxdy = \frac{\mu_0 d}{2} e^{-\sqrt{k_x^2 + k_y^2} z} \tag{II.2.10}$$

It is then possible to write the transform of B_x in function of the transform of the current density:

$$b_x(k_x, k_y, z) = \frac{\mu_0 d}{2} e^{-\sqrt{k_x^2 + k_y^2} z} j_y(k_x, k_y) \tag{II.2.11}$$

The same passages can be applied to the y component of B, obtaining:

$$b_y(k_x, k_y, z) = -\frac{\mu_0 d}{2} e^{-\sqrt{k_x^2 + k_y^2} z} j_x(k_x, k_y) \tag{II.2.12}$$

For the z component of b, the remaining terms are two; in this case, in fact, J_z does not appear in the product. The resulting transform is therefore [44]:

$$b_z(k_x, k_y, z) = -\frac{\mu_0 d}{2} e^{-\sqrt{k_x^2 + k_y^2} z} \left(\frac{k_y}{\sqrt{k_x^2 + k_y^2}} j_x(k_x, k_y) - \frac{k_x}{\sqrt{k_x^2 + k_y^2}} j_y(k_x, k_y) \right) \tag{II.2.13}$$

The easiest component of the magnetic induction field to measure is the z; most of the magnetic sensors, in fact, pick up just this component. It can be easily proven that in the quasi-static regime, for planar current distributions, the z component is enough to reconstruct the current map. For the quasi-stationarity of the bi-dimensional current, the continuity equation II.2.3 can be rewritten:

$$\frac{\partial \mathbf{J}_x(x, y, z)}{\partial x} + \frac{\partial \mathbf{J}_y(x, y, z)}{\partial y} = 0 \tag{II.2.14}$$

In the Fourier space equation II.2.14 becomes:

$$-ik_x j_x(k_x, k_y) - ik_y j_y(k_x, k_y) = 0 \tag{II.2.15}$$

The equation system is now complete: for two unknowns, $j_x(k_x, k_y)$ and $j_y(k_x, k_y)$, there are two equations, II.2.13 and II.2.15. Being the system linear, the solution exists and is unique. The same applies for the other components of B: each and any of them can give both components of the current density J.

II.2.2 The Inverse Problem

The inverse problem is just the opposite of the forward problem. The unknown of the problem is the bi-dimensional current distribution, while the variable which can be measured is the magnetic induction field over an $x-y$ plane. From an analytical point of view, this problem is of easy solution. For example, starting from the measurement of b_x, the equation II.2.9 can be inverted:

$$j_y(k_x, k_y) = \frac{b_x(k_x, k_y, z)}{g(k_x, k_y, z)} \tag{II.2.16}$$

However, this approach can be used as long as the denominator of equation II.2.16, i.e. the Fourier transform of the Green function, is not equal to zero, otherwise the solution will diverge. The Green function can be considered as an inverse filtering function; it is necessary that the filter does not approach either zero or infinity. A better understanding of the behavior of the filtering function is given by the relationship between b_x and j_x. This relationship can be obtained by combining the equation II.2.11 with the continuity condition given by II.2.15:

$$j_x(k_x, k_y) = \frac{-2}{\mu_0 d} \frac{k_y}{k_x} e^{z\sqrt{k_x^2+k_y^2}} b_x(k_x, k_y, z) \tag{II.2.17}$$

It is interesting to see that, when k_x is zero, and therefore the current is uniform on the x direction, b_x will be zero too. Thus, by measuring B_x it is not possible to have a unique solution, as uniform currents on the x axis will not be detected. The same reasoning applies for B_y. However, the knowledge of B_z is enough to obtain a unique solution, given that the current is constrained to an $x-y$ plane and has therefore no z component. Another thing to be noted in equation II.2.17 is that the solution diverges when $\sqrt{k_x^2 + k_y^2}$ tends towards infinity. This happens when one or both the spatial frequencies diverge; furthermore, this term appears inside an exponential, meaning that it will diverge much sooner than the spatial frequencies themselves. The computed current is therefore a high-pass filtered version of the magnetic induction field.

Due to the low-pass filtering given by the Biot-Savart law, the solution to the inversion problem given before tends to be unstable, unless the working distance z is very small. In order to prevent equation II.2.16 from diverging, it is necessary to apply a spatial filtering function to the acquired magnetic field, therefore cutting all the higher spatial frequencies. One way of doing that is to pull down to zero all the spatial frequencies $k > k_{max}$. In the space domain, this is equivalent to applying a windowing filter $f(k)$ to the magnetic field. By doing so, the information given by the high spatial frequencies is lost, but in compensation the solution does not diverge anymore. The trade-off between an high k_{max} and a stable inversion is what prevents the possibility of having a good spatial resolution when the working distance increases. In addition to this, the measurement of B contains a certain amount of noise, which increases with z. It therefore becomes impossible to obtain good resolutions at long working distances.

A very interesting conclusion is that it is possible to evaluate both components of the current distribution by using only the knowledge of b_z. This is due to the continuity conditions given by the equation

II.2.15. Therefore, the two components of the current distribution in the Fourier space, once applied the already mentioned filter, become:

$$\begin{aligned} j_x(k_x, k_y) &= \frac{-2i}{\mu_0 d}\frac{k_y}{k}e^{kz}b_z(k_x, k_y, z)f(k) \\ j_y(k_x, k_y) &= \frac{2i}{\mu_0 d}\frac{k_x}{k}e^{kz}b_z(k_x, k_y, z)f(k) \end{aligned} \tag{II.2.18}$$

II.2.3 The inversion problem for three-dimensional current distributions

In the case of current densities which are distributed over the three-dimensional space, the equation II.2.3 for the continuity of the current in the case of quasi-static fields becomes:

$$\frac{\partial \mathbf{J}_x(x, y, z)}{\partial x} + \frac{\partial \mathbf{J}_y(x, y, z)}{\partial y} + \frac{\partial \mathbf{J}_z(x, y, z)}{\partial z} = 0 \tag{II.2.19}$$

In the Fourier space this equation becomes:

$$-ik_x j_x(k_x, k_y, z) - ik_y j_y(k_x, k_y, z) + \frac{\partial \mathbf{j}_x(k_x, k_y, z)}{\partial z} = 0 \tag{II.2.20}$$

It has to be noted that the Fourier transform has been applied only on the x and y axes as the measurement of B is performed only on a plane of constant z. The number of equations needed to solve this problem are now therefore three, as the z component of the current distribution has been added. At the same time, the equations regulating the z component of the magnetic induction field are modified by the presence of a vertical current J_z. The resulting equation, obtained by processing the Biot-Savart law of equation II.1.25, is the following:

$$B_z(x, y, z) = \frac{\mu_0}{4\pi}\int_{-\infty}^{+\infty}\int_{-\infty}^{+\infty}\int_{-\infty}^{+\infty}\frac{(y - y')J_x(x', y', z') - (x - x')J_y(x', y', z')}{[(x - x')^2 + (y - y')^2 + (z - z')^2]^{3/2}}dx'dy'dz' \tag{II.2.21}$$

There are two direct consequences of this equation. The z component of B does not carry any information about the vertical currents. This is due to the fact that currents and magnetic fields are always perpendicular to each other as B is the result of a vectorial product involving the current. Furthermore, this equation on its own is not enough to gather information about the current distribution, as the variables are now three, while only two equations have been studied.

The Fourier transform of B_z can then be obtained from equation II.2.21 by application of the convolution theorem:

$$b_z(k_x, k_y, z) = \frac{i\mu_0}{2} \int_{-\infty}^{+\infty} e^{-\sqrt{k_x^2+k_y^2}(z-z')} \left(\frac{k_y}{\sqrt{k_x^2 + k_y^2}} j_x(k_x, k_y, z') - \frac{k_x}{\sqrt{k_x^2 + k_y^2}} j_y(k_x, k_y, z') \right) dz' \qquad \text{(II.2.22)}$$

The problem of this equation is that it cannot be solved for either j_x or j_y, but it needs to be solved for the entire integral, so that it would not be possible to separate the components as it was possible for two-dimensional distributions.

It can be easily proven [44] that different current distributions can generate the same magnetic field measurement on a plane above the current: in other words, the solution for the three-dimensional problem is not unique. The only way to be able to reconstruct a full three-dimensional current would be to obtain the measurement of the magnetic field over the whole space, and mostly at points which are internal between different magnetic sources, altough this is impossible in practice. This reasoning, however, does not mean that it is never possible to analytically reconstruct a three-dimensional current map, but that there will be simply some cases where the solution will not be unique.

By applying a certain number of geometrical and/or electrical constraints to the analytical model, it is possible to demonstrate that the number of solutions to the inversion problem can be drastically reduced, until, for the right number of constraints, the solution can be unique. From this starting point, and knowing that for the real case of failure analysis the possible current paths are not infinite, but depend on the sample to be analyzed, a new approach based on a simulation model has been developed and will be shown in the part III.

II.2.3.1 The inward continuation

In a perfect world, where there is no noise involved, it would be possible to measure the magnetic induction field on a plane parallel to the bi-dimensional current distribution at any distance z and obtain the same result from the inversion algorithm. This is the consequence of what has been called the inward continuation [44]. To understand the analytical meaning of this sentence, it is sufficient to study better equation II.2.13 for two given working distances z_1 and z_2:

$$\begin{aligned} b_z(k_x, k_y, z_1) &= -\frac{\mu_0 d}{2} e^{-\sqrt{k_x^2+k_y^2} z_1} \left(\frac{k_y}{\sqrt{k_x^2 + k_y^2}} j_x(k_x, k_y) - \frac{k_x}{\sqrt{k_x^2 + k_y^2}} j_y(k_x, k_y) \right) \\ b_z(k_x, k_y, z_2) &= -\frac{\mu_0 d}{2} e^{-\sqrt{k_x^2+k_y^2} z_2} \left(\frac{k_y}{\sqrt{k_x^2 + k_y^2}} j_x(k_x, k_y) - \frac{k_x}{\sqrt{k_x^2 + k_y^2}} j_y(k_x, k_y) \right) \end{aligned} \qquad \text{(II.2.23)}$$

Therefore, once the value of b_z has been measured on a plane z_1, it can be analytically evaluated on any other plane parallel to it: on the plane z_2, for example, it is:

$$b_z(k_x, k_y, z_2) = e^{-\sqrt{k_x^2+k_y^2}(z_1-z_2)} b_z(k_x, k_y, z_1) \tag{II.2.24}$$

From equation II.2.24 it is clear that, from the knowledge of the magnetic field on a plane at constant z, it is possible to evaluate the magnetic field in any other plane parallel to it, and therefore in the whole space, on condition that there is no additional source. This means that there is no additional information that can be gained by measuring the magnetic field on more than one plane. What can be done, however, is to use this technique to obtain the evaluation of the magnetic field on a plane very close to the sources, so that the filtering function to be applied to obtain the inverse calculation can use an higher k_{max}, and therefore keep in the calculation much higher spatial frequencies. In any case, this technique is always limited by the noise level at the measurement points: even if it is possible then to evaluate analytically the magnetic field on a plane closer to the sources given the measurement on a plane further away, the SNR stays at the level of the measurements, which is obviously higher at higher working distances.

II.2.4 Noise and spatial resolution

In this section the results obtained by [46] will be reported and discussed. It is of fundamental importance to understand that the best spatial resolution which can be obtained is strongly dependent on the SNR on the magnetic measurement. There are two different sources of magnetic noise: from the environment, and from the magnetic sensor itself. In order to perform a complete noise analysis it is therefore necessary to refer to the actual sensor that is used to acquire the magnetic field. However, there are some assumptions that can be made independently from the sensor used. The analyses performed in [44] and [45] take into account the noise produced inside a SQUID sensor. A more generic analysis can be conducted to understand how the noise in the magnetic acquisition propagates through the inversion algorithm to the final current map, so that the result is a noisy current distribution. In conclusion, the noise present at the acquisition limits the spatial resolution achievable by the inversion technique.

II.2.4.1 Current inversion noise

The noise analysis can be performed starting from a simple case of a magnetic field acquisition which is zero at all points but at the origin, where it contains a noise spike:

$$B_z(x, y, z) = B_0 A \delta^2(x, y) \tag{II.2.25}$$

As the acquisition is performed at a discrete number of points, it is possible to talk about a magnetic image composed by single pixels. In this case, A is the area of the pixel, and B_0 is the root mean square value of the noise. As the Fourier transform of an impulse is one, b_z will be constant at all points and equal to $B_0 A$: the noise spike generates a noise value which is constant at all the spatial frequencies. The evaluated x component of the current density in the Fourier space is given by the substitution of equation II.2.25 into the first part of equation II.2.18:

$$j_x(k_x, k_y) = \frac{-2i}{\mu_0 d}\frac{k_y}{k}e^{kz}B_0 A f(k) \tag{II.2.26}$$

and its inverse Fourier transform will be the filtered version of the x component of the current distribution generated by the noise spike:

$$J_x^F(x,y) \approx \frac{-1}{(2\pi)^2}\frac{2i}{\mu_0 d}\int_{-\infty}^{+\infty}\int_{-\infty}^{+\infty}\frac{k_y}{k}e^{kz}B_0 A e^{-i(k_x x + k_y y)} f(k) dk_x dk_y \tag{II.2.27}$$

By choosing a windowing filter for $f(k)$ with k_w the cut off frequency, equation II.2.27 can be solved as explained in [46]:

$$J_x^F(x,y) \approx -\frac{B_0 A}{\pi\mu_0 d}\frac{y}{r}J_1(k_w r)\left(\frac{e^{k_w z}(k_w z - 1) + 1}{z^2}\right) \tag{II.2.28}$$

and similarly:

$$J_y^F(x,y) = -\frac{B_0 A}{\pi\mu_0 d}\frac{x}{r}J_1(k_w r)\left(\frac{e^{k_w z}(k_w z - 1) + 1}{z^2}\right) \tag{II.2.29}$$

with J_1 the Bessel function of the first kind. The module of the complete current density can be obtained by adding together the square values of the two components:

$$\left|J^F(x,y)\right|^2 \approx \left(\frac{B_0 A}{\pi\mu_0 d}\right)^2 J_1^2(k_w r)\left(\frac{e^{k_w z}(k_w z - 1) + 1}{z^2}\right)^2 \tag{II.2.30}$$

The approximations in the equations II.2.27,II.2.29 and II.2.30 are valid for $k_w << 1$. If this function is plotted, as shown in figure II.2.2, it is possible to see how the magnetic impulse at the origin is generated by a series of circulating currents.

The same reasoning can be applied to a more generic case where the noise is present at every point. The magnetic field can therefore be rewritten by using the superposition principle:

$$B_z(x,y,z) = \sum_i^N B_i A\delta^2(x - x_i, y - y_i) \tag{II.2.31}$$

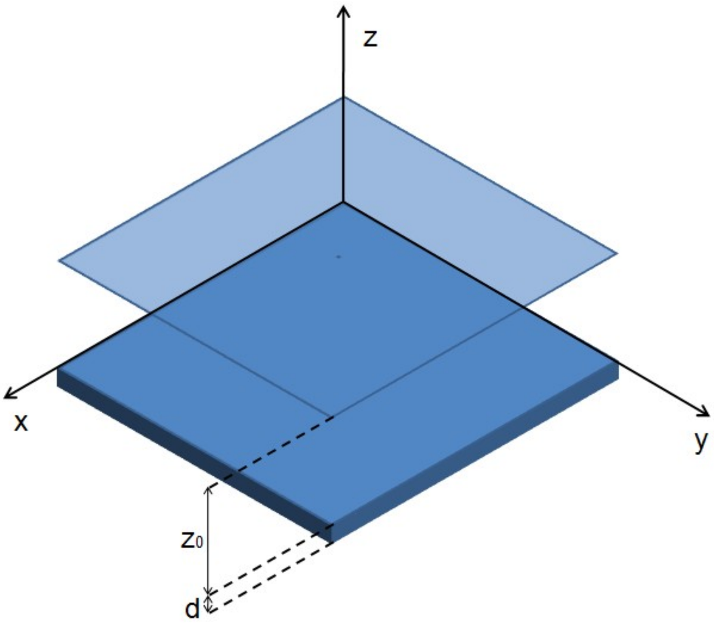

Figure II.2.1: The measuring plane. All the current distribution is limited in the space of thickness d

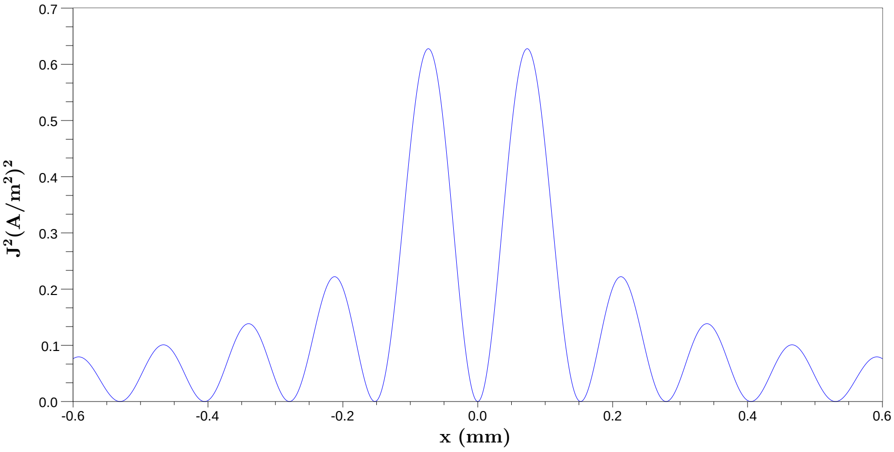

Figure II.2.2: Current image generated by a magnetic spike noise

As equation II.2.31 is a simple superposition of single contributors to the magnetic noise, the same method can be applied to evaluate the image of the current generated by the noise:

$$J_x(x,y) = \sum_i^N J_x^F(x - x_i, y - y_i)\frac{B_i}{B_0} \tag{II.2.32}$$

and the mean square deviation for the x component will be:

$$[\Delta J_x(x,y)]^2 = \sum_i^N \left|J_x^F(x - x_i, y - y_i)\right|^2 \left(\frac{\Delta B}{B_0}\right) \tag{II.2.33}$$

and therefore the total mean square deviation:

$$[\Delta J(x,y)]^2 = \sum_i^N \left|J^F(x - x_i, y - y_i)\right|^2 \left(\frac{\Delta B}{B_0}\right) \tag{II.2.34}$$

The sum can be approximated as an integral if the pixel size is very small compared to the inverse of the cut off spatial frequency. For an image of area L^2 and with $n_x \times n_y = N$ pixels equation II.2.34 becomes:

$$[\Delta J(x,y)]^2 = \left(\frac{\Delta B}{B_0}\right) \int_{-\frac{L}{2}}^{\frac{L}{2}} \int_{-\frac{L}{2}}^{\frac{L}{2}} \left|J^F(x - x_i, y - y_i)\right|^2 \frac{n_x n_y}{L^2} dx' dy' \tag{II.2.35}$$

As the noise distribution is the same all over the image, it can be evaluated at the origin:

$$[\Delta J(0,0)]^2 = \left(\frac{\Delta B}{B_0}\right) \frac{N}{L^2} \int_{-\frac{L}{2}}^{\frac{L}{2}} \int_{-\frac{L}{2}}^{\frac{L}{2}} \left|J^F(x,y)\right|^2 dxdy = \frac{1}{2\pi} \left(\frac{\Delta x \Delta B}{\mu_0 dz}\right)^2 \left[e^{2k_w z}(2k_w z - 1) + 1\right] \tag{II.2.36}$$

Where the last identity of equation II.2.36 has been evaluated by using Parseval's theorem. What is important to see from this last equation is the relationship between the magnetic noise ΔB and the noise of the current image ΔJ. It is possible to see that the noisiness of the current image increases with that from the magnetic field, as expected; furthermore, the current noise increases with the product $k_w z$, and the relationship is exponential. In other words, if in the inversion algorithm very high spatial frequencies are taken into account, or if the working distance increases too much, the current image becomes too noisy to be of any meaning.

II.2.4.2 Spatial resolution

In order to understand how the acquisition noise can influence the space resolution, this needs to be first defined. The spatial resolution is the Full-Width at Half Maximum (FWHM) of the square value of the current density, as it is represented in figure II.2.3.

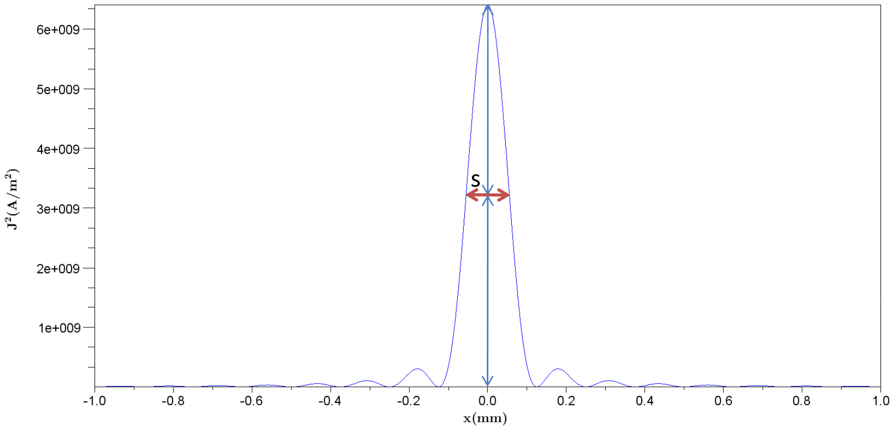

Figure II.2.3: Definition of the spatial resolution s as the full-width at half-maximum of the square value of the current profile

To find the relationship between the spatial resolution and the magnetic acquisition noise, a simple case of an infinite wire carrying a current I and flowing in the y direction, with a thickness d will be studied.

The two components of the current distribution on the plane are:

$$\begin{aligned} J_x(x,y) &= 0 \\ J_y(x,y) &= \left(\frac{I}{d}\right)\delta(x) \end{aligned} \tag{II.2.37}$$

The Fourier transform of the y component of the current is then independent of the space frequencies, if not for the filtering function:

$$j_y(k_x,k_y) = \frac{I}{d} f(k_w) \tag{II.2.38}$$

If the filter function is a hard cut-off windowing function, the inverse Fourier transform of the current is:

$$J_y(x,y) = \frac{I}{d\pi}\frac{\sin(k_w x)}{x} \tag{II.2.39}$$

To evaluate the spatial resolution, it is necessary to evaluate the maximum of the square of II.2.39, which can be rewritten as follows in terms of the sinc function:

$$J_y^2(x, y) = \left(\frac{Ik_w}{d\pi}\right)^2 \left(\frac{\sin(k_w x)}{k_w x}\right)^2 = \left(\frac{Ik_w}{d\pi}\right)^2 sinc^2(k_w x) \tag{II.2.40}$$

The maximum of II.2.40 is at the origin, and its value is:

$$J_y^2(x, y)_{MAX} = \left(\frac{Ik_w}{d\pi}\right)^2 \tag{II.2.41}$$

and therefore to evaluate the FWHM, the following equation needs to be solved:

$$\frac{J_y^2(x, y)}{J_y^2(x, y)_{MAX}} = \frac{1}{2} \Rightarrow sinc(k_w x) = \frac{1}{\sqrt{2}} \tag{II.2.42}$$

the two solutions of equation II.2.42 can be found numerically and are for $K_w x_{1,2} = \pm 1,391$. The spatial resolution is therefore:

$$s = \frac{2.782}{k_w} \tag{II.2.43}$$

which is inversely proportional to the cut-off spatial frequency k_w.

It is now possible to evaluate the signal to noise ratio of a pixel for the previous example by using the equation II.2.36 for the noise and the equation II.2.40 for $x = 0$ for the signal:

$$SNR = 2\pi \frac{\left(\frac{\mu_0 I k_w z}{\pi \Delta x \Delta B}\right)^2}{\left[e^{2k_w z}(2k_w z - 1) + 1\right]} \tag{II.2.44}$$

The SNR decreases exponentially with both the working distance z and the cut-off frequency k_w. The equation II.2.44 can be rewritten in terms of the ratio between the working distance and the spatial resolution by substituting into it equation II.2.43:

$$SNR = 2\pi \frac{\left(\frac{2.782\mu_0 I}{\pi \Delta x \Delta B} \frac{z}{s}\right)^2}{\left[e^{5.564\frac{z}{s}}\left(5.564\frac{z}{s} - 1\right) + 1\right]} \tag{II.2.45}$$

From this last equation it is clear that the signal to noise ratio is an implicit function of the ratio z/s: at SNR constant, the increase of the working distance gives a linear decrease of the spatial resolution.

II.2.5 Conclusion

In this chapter the use of the measurement of B_z to produce the values of J_x and J_y in a bi-dimensional structure has been shown. Having the current distribution on the plane is enough to determine where the defect, for instance a short circuit, is located. This technique, Magnetic Current Imaging, can be achieved using Magnetic Microscopy, which has been studied in this work. Magnetic Current Imaging will be described further in the next chapter.

CHAPTER II.3

Scanning SQUID Microscopy

Scanning SQUID Microscopy is the technique which links the Magnetic Current Imaging algorithm to the use of a SQUID sensor. As the SQUID is the most sensitive magnetic sensor known today, it is the most suitable one for mapping currents which are flowing relatively far away from it. The SQUID sensor is therefore today the only sensor which can be used to generate current maps in three dimensions. The Magnetic Microscope used for this work is the Neocera Magma C20[47], and it is shown in figure II.3.1.

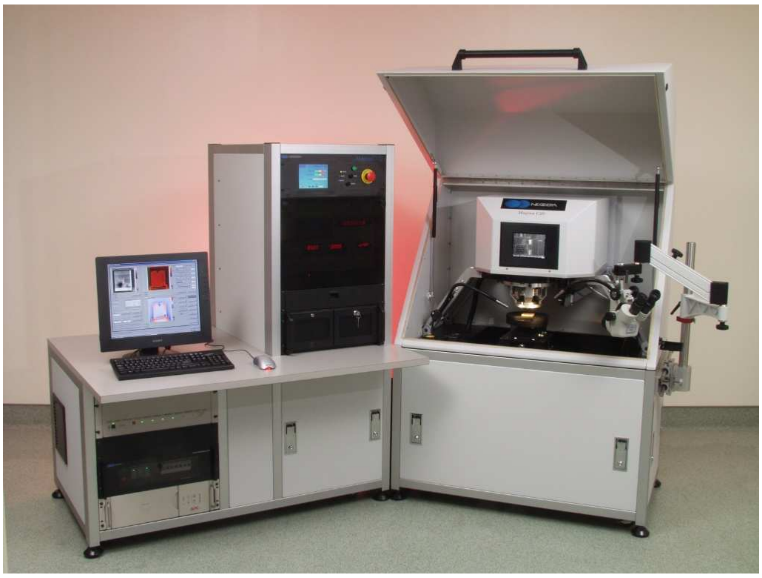

Figure II.3.1: Neocera Magma C20

II.3.1 SQUID system

A Superconducting QUantum Interference Device, or SQUID, needs to be cooled down to its superconducting state to be working properly [48]. The sensor used in this work is a high temperature SQUID: it needs to reach a temperature of approximately $80 - 90K$, with respect to the low temperature SQUIDS which need to work at temperatures as low as $4k$.

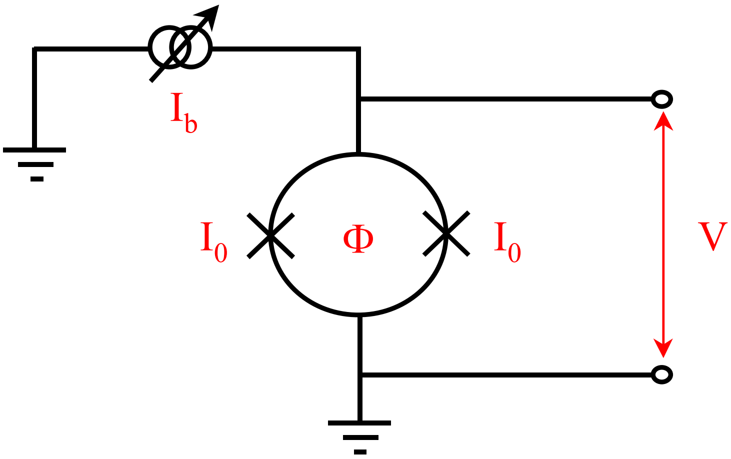

Figure II.3.2: Schematic diagram of a SQUID sensor

The sensor is made up of a superconducting loop interrupted by two Josephson junctions, as in figure II.3.2. A Josephson junction consists of two superconducting mediums with a thin insulating layer interposed between them. When kept at low temperature, the voltage drop across the junction is zero up to a certain value of the current, called the critical current I_0.

When the current flowing inside the loop, formed from the two junctions, exceeds the critical current, the voltage on the junctions is not zero anymore, but becomes dependent on the magnetic flux interjected in the loop. The current in function of the voltage is shown in figure II.3.3.

ΔV is the so-called modulation depth of the SQUID when external fields are applied to the sensor. In other words, ΔV is the voltage range that can be measured across the loop. The Josephson junctions are maintained in the normal conducting area by applying to them a bias current I_b[50][51].

Furthermore, the voltage on the loop is a periodic function of the magnetic flux, with the flux quantum as the period. This relationship is shown in figure II.3.4. In order to keep the working point in the same period, an external magnetic flux is constantly applied to the SQUID with a negative feedback system, the flux-locked loop. The applied magnetic flux will therefore be related to the external magnetic field in a linear way, and will provide the information regarding the measured field.

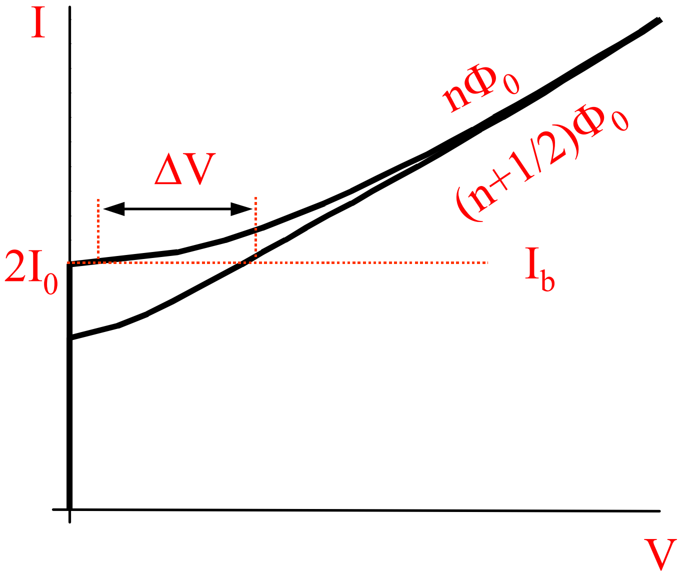

Figure II.3.3: Voltage-Current characteristic of a SQUID [49]

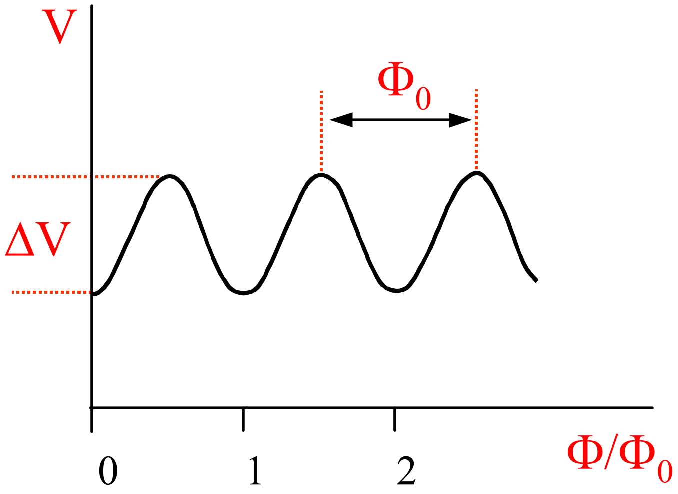

Figure II.3.4: Voltage drop across the SQUID loop in function of the magnetic flux [49]

II.3.2 Lock-in mode

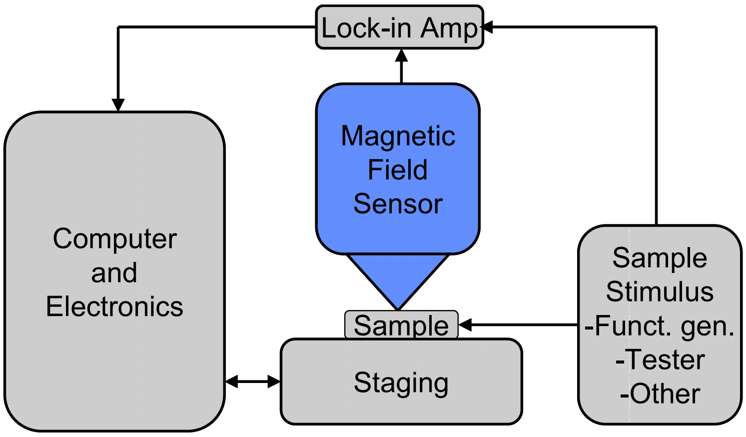

Figure II.3.5: MCI system diagram [49]

In order to obtain the highest Signal-to-Noise Ratio, the DUT is powered up with an AC signal, which will be synchronized with a lock-in amplifier. The same amplifier will receive the magnetic signal from the SQUID, as in figure II.3.5, and will filter out all the unwanted frequencies. In this way most of the magnetic noise, which is either DC or some fixed frequencies, will be filtered out.

II.3.3 MCI sample application

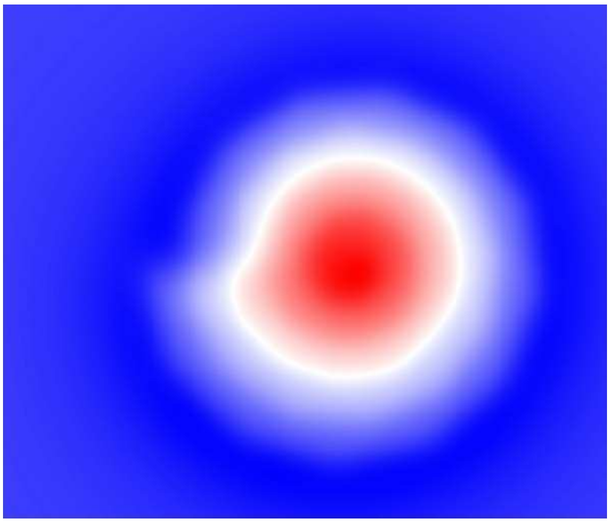

Figure II.3.6: Magnetic acquisition of a patch antenna

The magnetic scan for a simple application of the MCI algorithm using the Scanning SQUID Microscopy is shown in figureII.3.6. This image shows the acquisition performed over a patch antenna. What is interesting to notice is that in this case a simple look at the map of the magnetic field does not give any information regarding the currents flowing in the sample. It is clear that there is some magnetic activity generated from the antenna, but without the application of the MCI algorithm it is impossible to say where the currents are flowing.

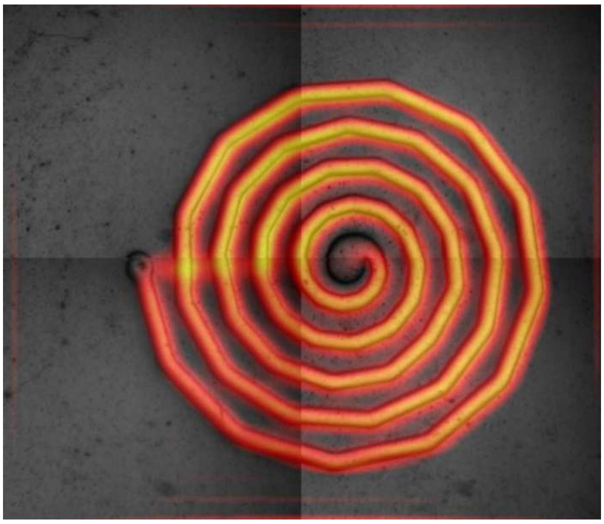

Figure II.3.7: Current flowing inside the patch antenna

In figure II.3.7 the result of the MCI algorithm is shown. In this figure the path followed by the current over the antenna is clearly shown.

Magnetic Current Imaging with a scanning SQUID is therefore a great tool for failure localization, as it is able to generate the map of the currents flowing inside a package without the need to open it [52]. A number of applications, by using both SQUID and other sensors, can be found in [53][54][55][56][57][58][59][60][61][62][63][64][65][66].

CHAPTER II.4

Conclusion

In this part the link between the magnetic field and the current density has been shown. Thanks to the MCI technique, it is possible to rebuild bi-dimensional current maps from the measurement of B_Z. The sensor used for acquiring the magnetic field is the SQUID, chosen for its high sensitivity, allowing the reconstruction of currents flowing at a large distance from it. The main limitation of the MCI technique is its inability to work on 3D structures [67]. This is why a specific approach, studied expressly for 3D currents, was developed. This will be shown in part III.

Part III

3D Magnetic Microscopy

CHAPTER III.1

Introduction

Magnetic Microscopy techniques are very useful to localize buried currents inside non-ferromagnetic materials. However, as it has been seen in the part II, this technique has a certain number of limitations due to the intrinsic use of both hardware and software tools. In order to overcome these limitations, the solution is to adopt a simulation approach: the idea is that the amount of information contained in the magnetic acquisitions is reduced by the operations needed in order to visualize the current (the MCI technique). The logical solution is therefore that of avoiding any calculation on the acquired data: the raw data is used, so that no filtering can reduce the amount of information. In order to fully exploit the raw data obtained with the acquisitions, the magnetic field generated by the currents flowing inside the device are simulated and compared to the acquisitions. In this way it is possible to extract more details about the currents locations, and therefore to increase the localization accuracy.

In chapter II.2 it has been shown how it is possible to generate a bi-dimensional reconstruction of the currents flowing on an $x - y$ plane from the measurement of the only z component of the magnetic induction field $\mathbf{B}$. Therefore, all the magnetic microscopy techniques used nowadays are focused on the measurement of this component, and do not take into account the others. This approach works perfectly as long as the geometry of the currents is bi-dimensional. However, as soon as the currents flow out of the chosen $x - y$ plane, the results given by the inversion algorithm are either missing or wrong. As a simple example a vertical current flowing on the z axis can be taken into account: it does not generate any contribution to the z component of magnetic field. The only possibility of generating the map of these currents is that of acquiring the other components of $\mathbf{B}$. The proposed solution is to tilt the sample on both the x and y axes, as will be explained in the next chapters. A full data acquisition will therefore contain three separate magnetic acquisitions, one for each component of $\mathbf{B}$. Some examples of the application of this new methodology will be shown at the end of this document.

In order to make the simulation process less time-consuming, a new model for generating the magnetic field distribution from the current distributions was developed. The simulation model was first developed to increase the localization accuracy of the standard technique by only using the information of the z component of $\mathbf{B}$. By applying the same algorithm, however, it is possible to produce the simulation of the other components, and obtain all the information needed.

To reduce the simulation time, an hypothesis of filiform currents was made, so that all the currents are mono-dimensional. This approximation is justified by the fact that the dimensions of the conductors inside an electronic device are normally very small compared to the distance from the probe to the current itself. Once the problem was simplified in this way, the analytical evaluation of the magnetic induction field could be obtained from a particular integration of the Biot-Savart law.

CHAPTER III.2

The simulation model

The main goal of the simulation model is to generate fast and reliable simulations. The simulations which are performed with a Finite Elements Method (FEM) simulator are too time-consuming, and therefore cannot be used for more complicated current distributions. From this starting point, a simulation software based on the analytical simulation model was developed. In this way long and tedious Finite Elements simulations would be avoided. Furthermore, the results produced are directly related to the magnetic acquisitions, and not to the MCI results; it is therefore possible to evaluate quickly the correlation between measurements and simulations to localize all the currents.

III.2.1 The fast simulation

The solution found to avoid long simulations was that of using an analytical model: the laws of physics which govern the generation of the magnetic field are integrated according to specific needs.

III.2.1.1 Linear currents approximation

As stated before, simulated currents are approximated to filiform wires. This approximation is validated by the fact that the ratio between the working distance, which is the distance between the sensor and the current, and the current width is very high, as shown in figure III.2.1. For standard SQUID sensors, the z distance is always above $200\mu m$, while the line width is below $30\mu m$, which is the usual size of a bonding wire. Furthermore, when considering current lines flowing in the middle layers of a three-dimensional component, the working distance can easily increase above a few millimeters, and the working distance to line width ratio increases over 100. In this case, the linear approximation chosen for this study gives no appreciable error in the final results.

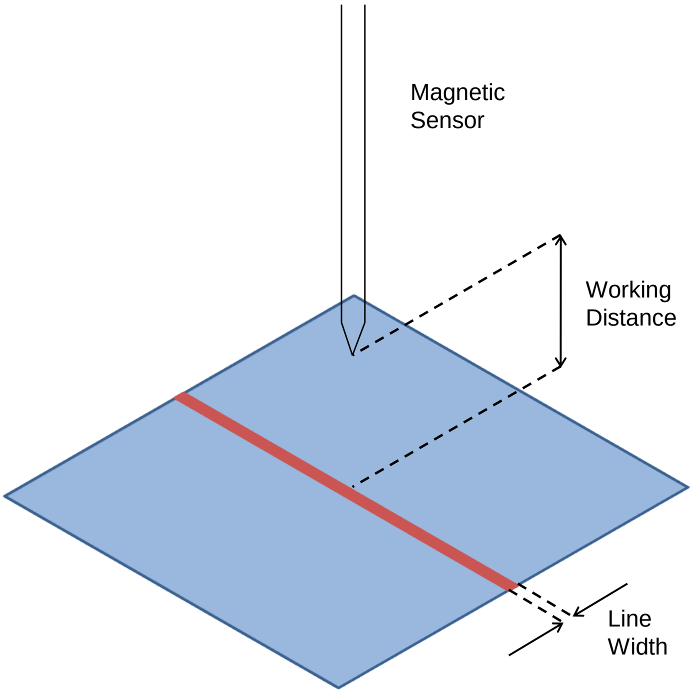

Figure III.2.1: Definition of the ratio between the working distance and the line width

III.2.1.2 Simplification of Biot-Savart's law

It has been shown in chapter II.1.2 that when a current flows through a filiform conductor as in figure III.2.2, it generates a magnetic induction field according to the law of Biot-Savart, which has been written in the differential form in equation II.1.26. When considering a mono-dimensional current line approximation, the current distribution can be written as:

$$\mathbf{J}dv' = I\mathbf{dl} \tag{III.2.1}$$

Therefore the Biot-Savart law can be simplified as follows:

$$\mathbf{dB} = \frac{\mu_0 I}{4\pi}\frac{\mathbf{dl}\times\mathbf{i}_{r'r}}{|\mathbf{r}-\mathbf{r}'|^2} \tag{III.2.2}$$

III.2.1.3 Magnetic field generated by a finite current line

If the case of a current flowing on the x axis is taken into account, the generality of the equation is not lost as the study can be reduced to a generic current flowing on an arbitrary axis by applying rotation matrices. The current is represented in figure III.2.2, where X is the distance along the x axis between the middle point of the current line and the origin of the cartesian reference. The new reference system is now centered on the middle point of the current line: the z component of the **B** vector on the $x-y$ plane at a distance z from the current line is:

$$dB_z(x,y,z) = \frac{\mu_0 I}{4\pi}\frac{y}{\sqrt{[(l-x)^2+y^2+z^2]^3}}dl \tag{III.2.3}$$

where $\sqrt{[(l-x)^2+y^2+z^2]^3}$ is the distance between the current element dl and the point **P** where the field is evaluated.

The equation III.2.3 must be integrated between $-L$ and L in order to obtain the full contribution of the current line on the z component of the magnetic induction field:

$$B_z(x,y,z) = \frac{\mu_0 I}{4\pi}\int_{-L}^{L}\frac{y}{\sqrt{[(l-x)^2+y^2+z^2]^3}}dl \tag{III.2.4}$$

To solve the integral of equation III.2.4, the following substitutions are carried out:

$$\begin{aligned} l-x &= k \Rightarrow dl = dk \\ y^2+z^2 &= a^2 \end{aligned} \tag{III.2.5}$$

so that the integral becomes:

$$B_z(x,y,z) = \frac{\mu_0 I}{4\pi}\int_{-L-x}^{L-x}\frac{y}{\sqrt{[k^2+a^2]^3}}dl \tag{III.2.6}$$

The solution of the integral of equation III.2.6 is obtained by a further substitution using trigonometrical functions:

$$\begin{aligned} k &= a\tan\theta \\ (k^2+a^2)^{\frac{1}{2}} &= \frac{a}{\cos\theta} \\ dk &= \frac{a}{\cos^2\theta}d\theta \end{aligned} \tag{III.2.7}$$

so that:

$$\begin{aligned} k = L - x &\Rightarrow \theta = \tan^{-1}\left(\frac{L-x}{a}\right) \\ k = -L - x &\Rightarrow \theta = \tan^{-1}\left(\frac{-L-x}{a}\right) \end{aligned} \tag{III.2.8}$$

In this way the induction field can be evaluated as follows:

$$\begin{aligned} B_z(x,y,z) &= \frac{\mu_0 I y}{4\pi}\int_{\tan^{-1}(\frac{-L-x}{a})}^{\tan^{-1}(\frac{L-x}{a})} \frac{\cos^3\theta}{a^3}\frac{a}{\cos\theta}d\theta = \\ &= \frac{\mu_0 I y}{4\pi a^2}\int_{\tan^{-1}(\frac{-L-x}{a})}^{\tan^{-1}(\frac{L-x}{a})} \cos\theta d\theta = \\ &= \frac{\mu_0 I y}{4\pi a^2}\Big[\sin\theta\Big]_{\tan^{-1}(\frac{-L-x}{a})}^{\tan^{-1}(\frac{L-x}{a})} = \\ &= \frac{\mu_0 I y}{4\pi a^2}\left[\frac{L-x}{\sqrt{(L-x)^2+a^2}} + \frac{L+x}{\sqrt{(L+x)^2+a^2}}\right] = \\ &= \frac{\mu_0 I}{4\pi}\frac{y}{y^2+z^2}\left[\frac{L-x}{\sqrt{(L-x)^2+y^2+z^2}} + \frac{L+x}{\sqrt{(L+x)^2+y^2+z^2}}\right] \end{aligned} \tag{III.2.9}$$

where the integral has been solved considering the trigonometrical substitution:

$$\sin\theta = \frac{\tan\theta}{\sqrt{1+\tan^2\theta}} \tag{III.2.10}$$

III.2.1.4 Magnetic field generated by an infinite current line

In some cases it might be interesting to consider the line as an infinite line, which simplifies the whole calculation. This happens mostly when the current line is sensibly longer than the area of interest where the magnetic field is evaluated. In this case equation III.2.9 can be modified according to the fact that:

$$L \to \infty \tag{III.2.11}$$

in which case:

$$\frac{L-x}{\sqrt{(L-x)^2+y^2+z^2}} + \frac{L+x}{\sqrt{(L+x)^2+y^2+z^2}} \to 2 \tag{III.2.12}$$

Equation III.2.9 can therefore be simplified as follows:

$$B_z(x, y, z) = \frac{\mu_0 I}{2\pi} \frac{y}{y^2 + z^2} \tag{III.2.13}$$

III.2.1.5 Generation of the simulation plane

In order to simplify the calculations, the current has been considered as flowing on the x axis. This means that a certain number of transformations to the working space will be needed in order to report the real current line, which obviously flows on a generic axis, to the real x axis.

The magnetic induction field generated at an arbitrary point P from a current flowing on an arbitrary direction can be easily evaluated by applying a set of transformations to the working reference system; the magnetic field of equation III.2.9 is generated from a current flowing on the x axis and evaluated at a point $P(x, y, z)$. Therefore, to apply this equation, the generic current line needs to be translated to the x axis, with the consequent transformation of the P point coordinates.

A current flowing on an arbitrary line is considered in figure III.2.3:

It can be noted that the measurement plane (corresponding to the simulation plane) is on a constant z plane. The current line is represented by the segment P_1P_2, and is identified by its middle point M and its direction. The generic point of the simulation plane, noted here as P_{ij}, has the following coordinates:

$$P_{ij}(x_i, y_j, Z) \tag{III.2.14}$$

where Z is constant, and x_i and y_j are the i^{th} and j^{th} place on the x and y axis of the simulation grid. When l_x and l_y are the lengths in meters of the measurement grid and n_x and n_y are the number of simulation points respectively on the x and y directions, and $P_0(x_0, x_0, Z)$ is the origin of the simulation grid, the following equations stand:

$$\begin{aligned} x_i &= x_0 + i * \frac{l_x}{n_x - 1} \\ y_j &= y_0 + j * \frac{l_y}{n_y - 1} \end{aligned} \tag{III.2.15}$$

In order to be able to apply the simplified formula III.2.9, valid for a current flowing on the x axis, used to evaluate the magnetic induction field at a point P_{ij} of the measurement grid, the segment needs to be lying on the x axis. Therefore the first transformation needed is a simple translation of the reference system to the middle point of the current line M. The generic point P' of the new system becomes therefore:

$$P' = P - M \tag{III.2.16}$$

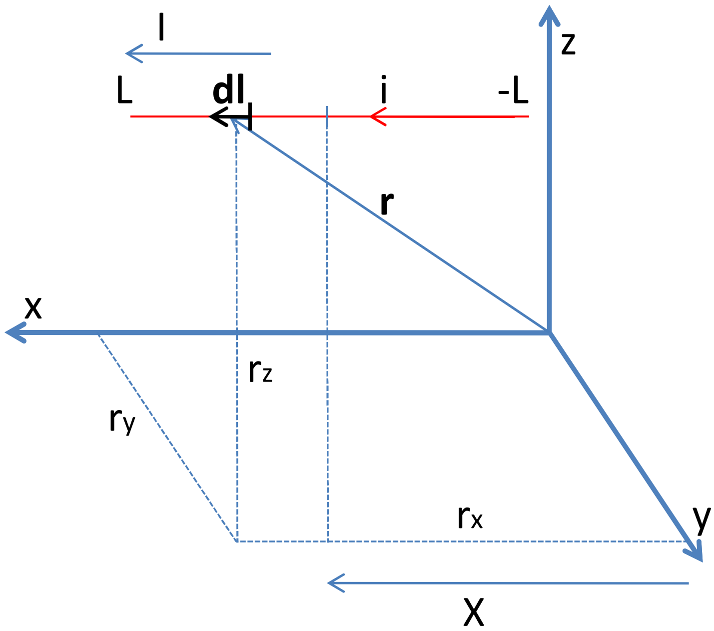

Figure III.2.2: Current through a finite wire

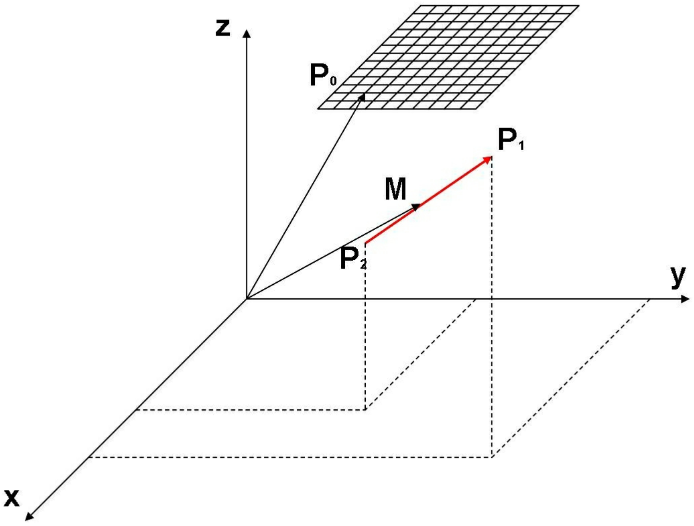

Figure III.2.3: Simulation model

The resulting system is shown in figure III.2.4.

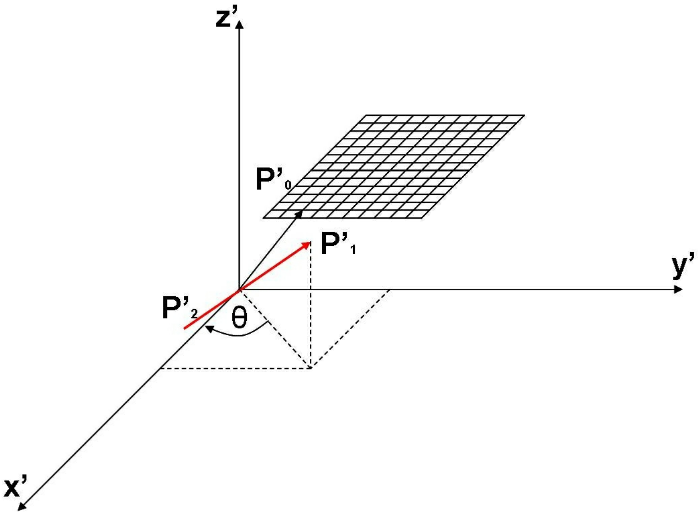

Figure III.2.4: System translation

The position of one of the extremes of the current segment, for example P'_1, gives the angles between the segment itself and the reference system. A first rotation of an angle θ around the y axis is needed in order to have a new system where the current is lying on the $x - z$ plane, as shown in figure III.2.5:

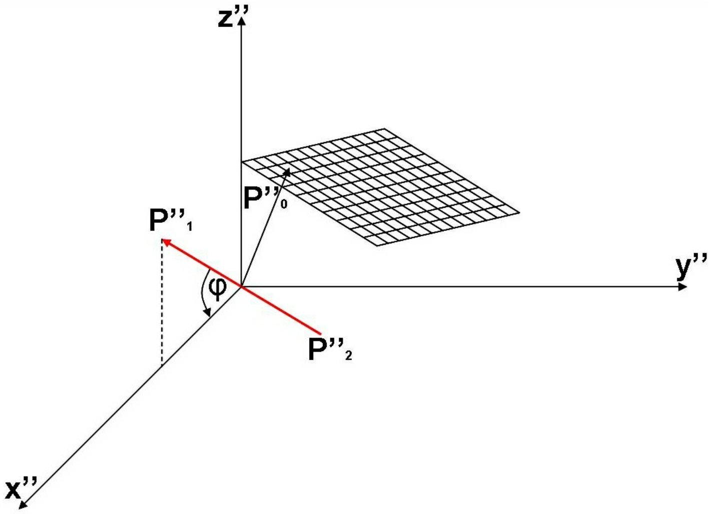

Figure III.2.5: Rotation on the y axis

The rotation matrix is therefore the following:

$$Q_y(\theta) = \begin{bmatrix} cos(\theta) & 0 & sin(\theta) \\ 0 & 1 & 0 \\ -sin(\theta) & 0 & cos(\theta) \end{bmatrix} \tag{III.2.17}$$

so that the generic point in the new reference system P'' is:

$$P'' = Q_y(\theta)P' = Q_y(\theta)(P - M) \tag{III.2.18}$$

The last rotation to be performed is around the z axis, and is needed in order for the segment to lie only on the x axis, as it is shown in figure III.2.6.

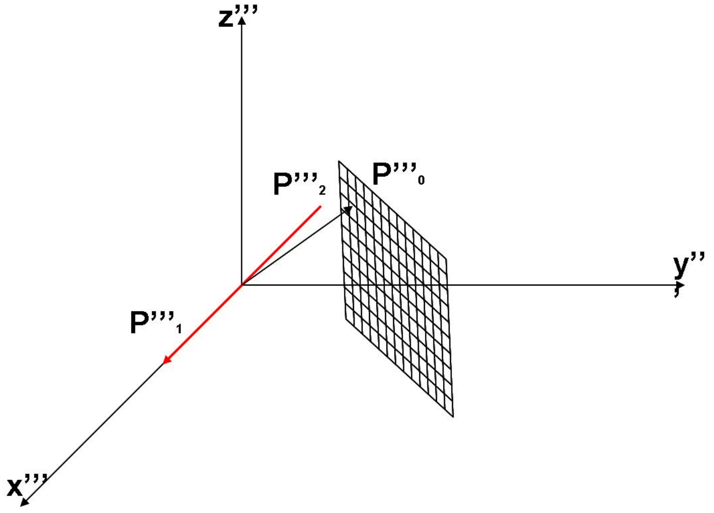

Figure III.2.6: Rotation on the z axis

The angle ϕ between the x and y axis defines the rotation matrix Q_z as follows:

$$Q_z(\phi) = \begin{bmatrix} cos(\phi) & -sin(\phi) & 0 \\ sin(\phi) & cos(\phi) & 0 \\ 0 & 0 & 1 \end{bmatrix} \tag{III.2.19}$$

so that the resulting generic point P''' is:

$$P''' = Q_z(\phi)P'' = Q_z(\phi)Q_y(\theta)P' = Q_z(\phi)Q_y(\theta)(P - M) \tag{III.2.20}$$

Now, thanks to the transformations of equation III.2.20 it is possible to move from the a particular reference system, lying on the current, to the reference system of the simulation model, which has the measurement plane lying on a $x - y$ plane. This methodology can be easily extended to the evaluation of the three components of the magnetic field, and not only to its z component. For example, to evaluate the z component, it is in general sufficient to apply the scalar product between the magnetic field and the unity vector $\hat{k} = (0, 0, 1)$:

$$B_z(x, y, z) = B(x, y, z) \cdot \hat{k} \tag{III.2.21}$$

As this product needs to be performed with respect to the initial reference system, the transformations of equation III.2.20 can be applied to the unity vector $\hat{k}$ too: the resulting unity vector , $\hat{k}'''$, will still have a modulus of 1, but will have an arbitrary direction in the new system. It will then be multiplied by $\mathbf{B}'''$, the transformed version of **B** in the new system, to obtain the value of B_z. The same logic can be applied to the other unity vectors $\hat{i}$ and $\hat{j}$.

By applying the equation III.2.20 to each point of the measurement plane in a matricial way, a much faster evaluation of **B** is obtained, with the best possible precision, since an analytical calculationwas used. By using the superposition principle, it is then very easy to generate the resulting **B** field by adding together all the single contributions brought by each current line.

III.2.1.6 Simulation methods comparison

In order to verify the usefulness of the simulation model, it was compared to some results obtained on a Finite Element simulator. The algorithm showed for the simulation model was implemented in an open source environment named Scilab. This software implements a free platform for numerical computation. It was chosen because of its versatility and customizability. All the results presented here were obtained with the use of this software.

The advantage of using an analytical simulator instead of a finite elements one is the amount of time saved. In order to prove the feasibility of this technique, the first simulations were performed with FEM software. Even though the results were satisfactory (varying only slightly from those obtained with the model presented here), the calculation time was much higher. In order to generate a matrix of 100000 points, a number of three-dimensional meshes of the system were performed, each with approximately 1000000 nodes. Each mesh took between 2 and 5 hours to generate, depending on the geometry to be discretized, while each simulation took between 30 min and 1 hour. The main drawback of this method is that as soon as the geometry of the current to be simulated changes, the Finite Element software must re-evaluate the mesh. This adds hours to the calculation time. Therefore just localizing one current with precision (which with the simulation approach involves the generation of tens of simulations), can take days if not weeks. The solution presented here does not involve meshes, and is therefore faster than the FEM simulation by several orders of magnitude. For the simulation model developed for this work, the calculation time depends on just two parameters: the number of points in the acquisition matrix, and the number of current lines which need to be simulated. Furthermore this method also allows the direct calculation of the correlation to the measurement, giving as an output the correlation curve together with the exact position of the current. The simulation time with this method, which varies according to the matrix size, took only a few seconds per line. The time taken for the simulations and the time needed to evaluate the correlation for each matrix are shown in table III.2.1: the time for evaluating the correlation is not significant if compared to the time taken for the simulations. All these values were evaluated as a mean time on a large number of simulations, as the precise simulation time can vary depending on the computer's activities at the time. In order to calculate the amount of time taken to evaluate the exact location of the current, it is enough to multiply the time for each simulation by the number of simulations needed.

Points	Simulation (s)	Correlation (s)
68706	2.51565	0.015625
97965	3.664773	0.025568
109998	4.089489	0.029578
130510	4.846591	0.036932
481347	17.680398	0.134943

Table III.2.1: Average time (in seconds) taken by the simulation and the evaluation of the correlation in function of the number of points

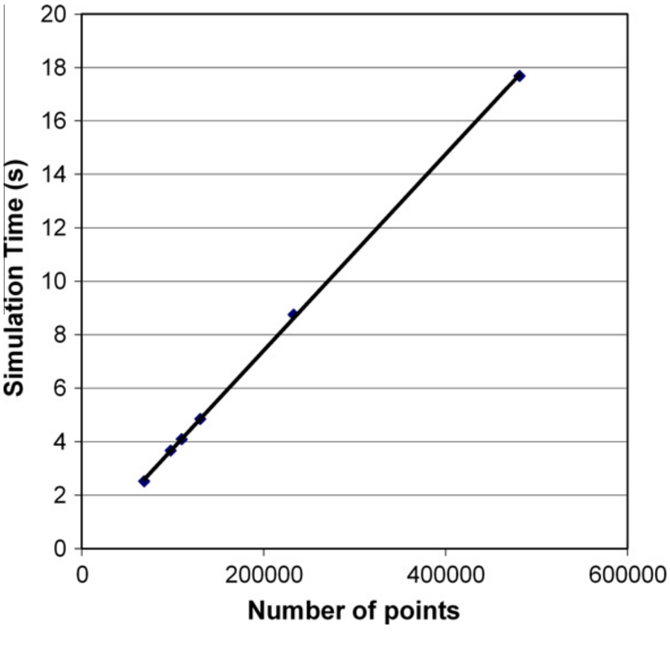

Figure III.2.7: Simulation time in function of the number of points

It can be noticed that there is a linear relationship between the number of points of the acquisition matrix and the simulation time. This can be seen clearly in figure III.2.7.

III.2.2 Localization of the most probable current paths

Once a fast simulation result of the magnetic field can be generated, it needs to be used to evaluate the correlation with the measured data. In this way it is possible to localize the current precisely. The basic idea is that, even though the number of possible paths is infinite, by using the knowledge of the internal structure of the sample (gathered in different ways: from CAD, optical acquisitions or X-Ray, both bi-dimensional and three-dimensional) it is possible to imagine a set of current path hypotheses. All of them will be simulated, and the resulting field will be compared to the magnetic acquisitions.

CHAPTER III.3

Application of the model to a current path localization

The simulation model described in chapter III.2 allows for the generation of the magnetic induction field in a fast way at any point, generated by any filiform current. The application of this model to current localization is straightforward: the measurement and the simulation are compared to each other through a correlation function.

The comparison between the measurements and the simulations can be carried out by using different methods, as for example the maximization of the likelihood or the minimization of the least square error. The function to compare the two sets of data which was chosen was a simple correlation one, as it is faster in terms of computing calculation. This is the function which will be used for all the comparisons explained in this document, unless expressly stated otherwise. The correlation function is described in Equation III.3.1:

$$Corr(M, S) = \frac{\overline{M \cdot S} - \overline{M} \cdot \overline{S}}{\sqrt{\left(\overline{M^2} - \overline{M}^2\right)\left(\overline{S^2} - \overline{S}^2\right)}} \tag{III.3.1}$$

where M is the measurement data, S is the simulation data, and the overline symbol signifies the mean value of the data set. This function can then be varied to obtain different types of information regarding the similarity of the two data sets. For example, instead of the standard correlation, which is applied to the first degree statistical moment, the higher degrees of moments can be used in order to obtain information about non-linear similarities.

The methodology developed for the localization of the currents comprises a number of transformations applied to the simulated current lines in order to obtain the highest correlation. This methodology uses the superposition principle to simplify a complex problem. As the magnetic field generated by all the currents flowing inside the sample can be evaluated by simulating the single contributions and by adding them together, the same rule applies to the correlation.

III.3.1 Localization of a current segment

As the magnetic field generated by a complex current path can be generated by using the superposition principle adding up the single elements, it is possible to consider a current path as a chain of single current lines. Each of the current lines can be identified by its parameters:

- Start point P_1
- End point P_2
- Current amplitude

where each point has three coordinates. There are therefore 7 parameters which are needed for the identification of each line. From this starting point, a number of geometrical transformations can be applied to the line, in order to obtain the highest possible correlation.

In the next sections, an example of the transformations which were developed in the simulation software will be shown. For each of them, a step and a range, both positive and negative, need to be defined, as will be explained in more detail for each of them. All of the examples will use a test vehicle to show the results obtainable.

III.3.1.1 Horizontal Line Shift

Once the current amplitude is fixed, the only parameters which can be varied are the two points. The most obvious way to move the line is to shift it horizontally; the line is moved in a direction perpendicular to itself. Negative and positive ranges can then be chosen together with the simulation step: the simulation will then be performed for all the lines going from the negative range to the positive one, at intervals of the step as shown in figure III.3.1. For each of these lines, the magnetic field will be generated and compared to the magnetic measurements; the resulting correlation will be stored in relation to the line position.

A typical result for this type of evaluation is shown in figure III.3.2. The final result will be the position of the current, given by the position of the maximum of the correlation curve.

III.3.1.2 Line rotation

Another transformation of the geometry of the current line is the line rotation. In this case, the negative and positive ranges are the two angles α and β which are shown in figure III.3.3. The step s is expressed

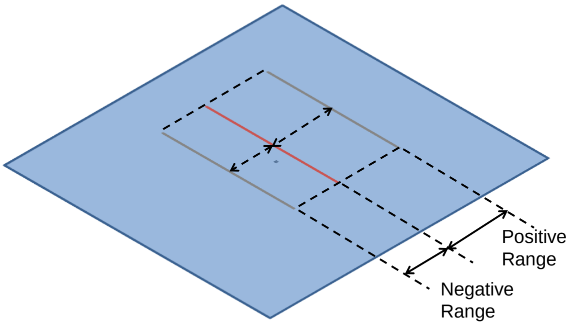

Figure III.3.1: Simulation of the horizontal shift of a line

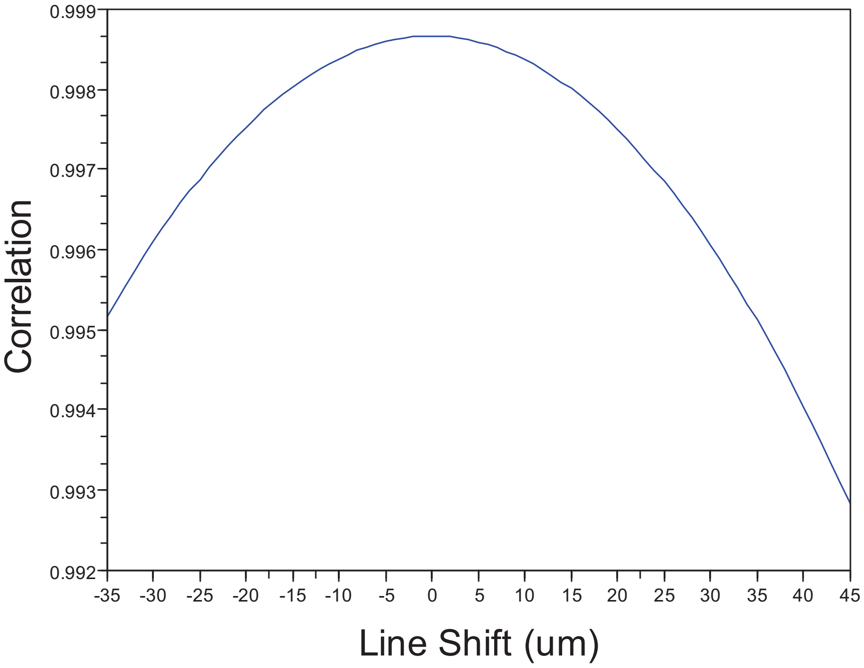

Figure III.3.2: Correlation results for a horizontal shift in degrees, so the number of simulations n which will be generated is given by the ratio between the total range and the step, in degrees, as explained in equation III.3.2:

$$n = \frac{\alpha + \beta}{s} \tag{III.3.2}$$

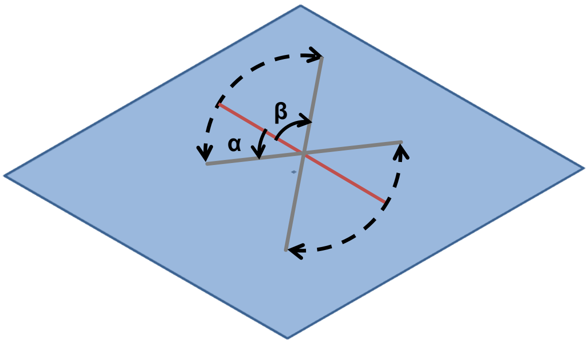

Figure III.3.3: Simulation of the rotation of a line

The rotation is applied to the line on the $x - y$ plane around its center. A typical result for this type of transformation is shown in figure III.3.4. As before, the peak of the curve represents the line rotation with the highest correlation to the measurement, and therefore the most probable direction of the real current line.

III.3.1.3 Line elongation

Another possible transformation applicable to the current line, still keeping it in the same $x - y$ plane, is a modification of the line length; to achieve that, both the start and end point can be shifted, either one at a time or simultaneously.

In figure III.3.5 this type of transformation is shown. The two points P_1 and P_2 can be moved in the direction of the line, and at each step a simulation and the consequent correlation with the measurement are evaluated. In this case the resulting curve of the correlation is not as precise as for the previous ones. This is due to the very small change in the distribution of the magnetic field for this transformation. However, as shown in figure III.3.6, there is still a peak representing the best line assumption. To create the curve of figure III.3.6, both points P_1 and P_2 were shifted the same length at the same time.

III.3.1.4 Influence of the current amplitude

In general, all transformations to the current lines are possible. What has not been covered in the previous sections was mostly the variation of the current amplitude and the z depth. These two parameters can be

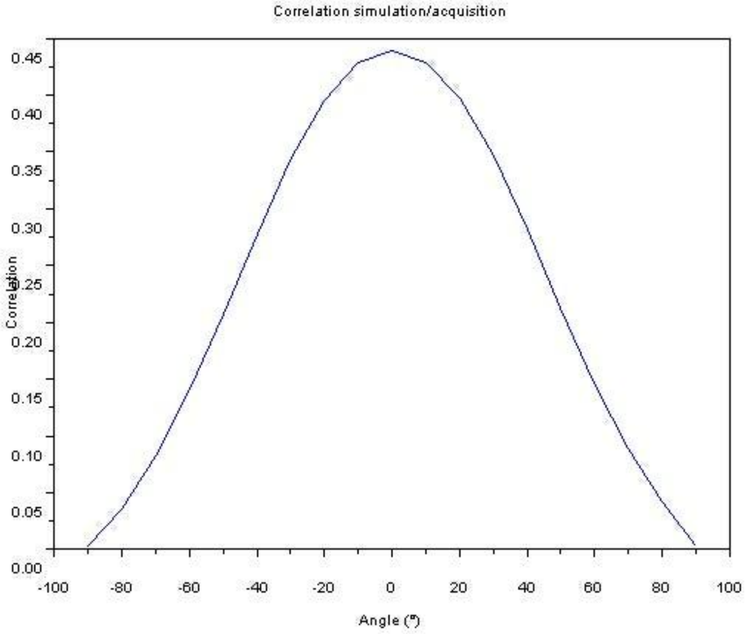

Figure III.3.4: Correlation results for a line rotation

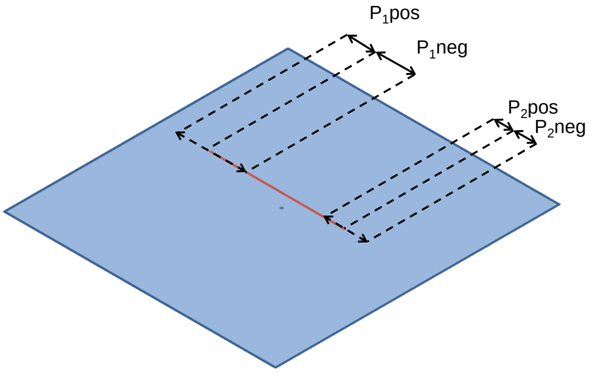

Figure III.3.5: Simulation of a line elongation

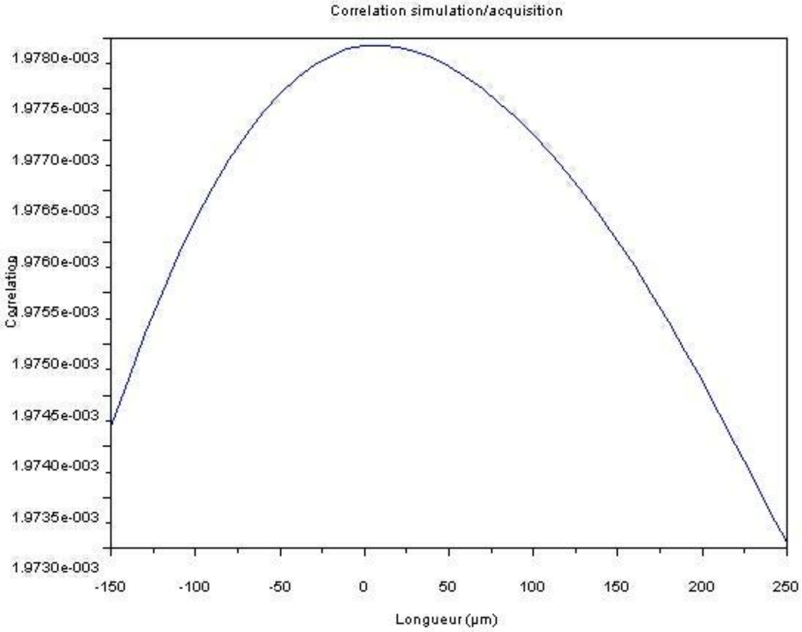

Figure III.3.6: Correlation results for a line elongation

used to obtain more information from the simulations; however, they need to be handled with care, as they do not always give the desired solution.

The correlation formula shown in equation III.3.1 of independent from any linear change of the variables:

$$Corr(M,kS) = \frac{\overline{M \cdot kS} - \overline{M} \cdot \overline{kS}}{\sqrt{\left(\overline{M^2} - \overline{M}^2\right)\left(\overline{(kS)^2} - \overline{kS}^2\right)}} = \frac{k(\overline{M \cdot S} - \overline{M} \cdot \overline{S})}{\sqrt{k^2\left(\overline{M^2} - \overline{M}^2\right)\left(\overline{S^2} - \overline{S}^2\right)}} = Corr(M,S) \qquad \text{(III.3.3)}$$

The k parameter of equation III.3.3 can be considered as the current amplitude of the simulated line. The amplitude of the first simulated current is therefore not important for the correlation value. However, what is taken into account is the relationship between the different simulated current lines:

$$Corr(M, k \cdot (k_1 \cdot S_1 + k_2 \cdot S_1)) = Corr(M, k \cdot k_1 \cdot S_1 + k \cdot k_2 \cdot S_1) \qquad \text{(III.3.4)}$$

Equation III.3.4 shows the usefulness of the correlation function. In fact it only takes into account the relationship between the different variables which are added together, but is invariable with the amplitude. This allows for minor calibration error between the measurement of the current applied to the device and the amplitude of the simulated magnetic field. However, if there is more than one current flowing inside the sample, the difference in the amplitudes will be considered.

III.3.1.5 Vertical depth simulation

The simulation of the variation of the vertical depth of the current lines does not always give the desired results. It is, though, still possible, in some cases, to obtain the z value of the current line by shifting it vertically in the same way as is done horizontally. This can be explained from the study of equation III.2.13: a variation of the value of z does not give a high variation of B_z, as a variation of y would. When considering for example a variation of z of 10% of its value, that is, for equation III.3.5, $z_2 = 1.1z_2$:

$$\begin{aligned} B_z(x, y, z_1) &= \frac{\mu_0 I}{2\pi} \frac{y}{y^2 + z_1^2} \\ B_z(x, y, z_2) &= \frac{\mu_0 I}{2\pi} \frac{y}{y^2 + z_2^2} = \frac{\mu_0 I}{2\pi} \frac{y}{y^2 + (1.1z_1)^2} \end{aligned} \tag{III.3.5}$$

The highest value of B_z is obtained for $y = z$, which also corresponds to the highest variation due to a variation in z. In this case equation III.3.5 can be simplified as follows:

$$\begin{aligned} B_z(x, y, z_1) &= \frac{\mu_0 I}{2\pi} \frac{z_1}{z_1^2 + z_1^2} = \frac{\mu_0 I}{2\pi} \frac{1}{2z_1} \\ B_z(x, y, z_2) &= \frac{\mu_0 I}{2\pi} \frac{z_1}{z_1^2 + 1.21z_1^2} = \frac{\mu_0 I}{2\pi} \frac{1}{2.21z_1} \end{aligned} \tag{III.3.6}$$

The variation of B_z can then be evaluated as:

$$\frac{\Delta B_z}{B_z} = 2z_1 \left(\frac{1}{2z_1} - \frac{1}{2.21z_1} \right) \approx 0.05 \tag{III.3.7}$$

From the above equations, it can be seen that the variation of the magnetic field is more substantial for a variation of y than for a variation of z. In conclusion, a variation of z usually results in a variation in B_z too small to obtain meaningful results for a vertical line shift. That is why the solution which was found was that of using a fitting algorithm in order to obtain the desired z values. This approach can only be used when there is one current line well separated from the others, so that the B_z curve can be considered equivalent to the theoretical one. In this case, the curve to be fitted will be:

$$f(x) = o + \frac{\mu_0 I}{2\pi} \frac{x - x_0}{(x - x_0)^2 + z^2} \tag{III.3.8}$$

where the parameters to fit are the offset o, the current amplitude I, the zero value of the curve x_0 and the z depth. A good fit, for a low-noise measurement of a single straight current line, can give a very precise result. What is most important for this type of analysis, is the determination of the z distance. An example of how to use this information is given in [68].

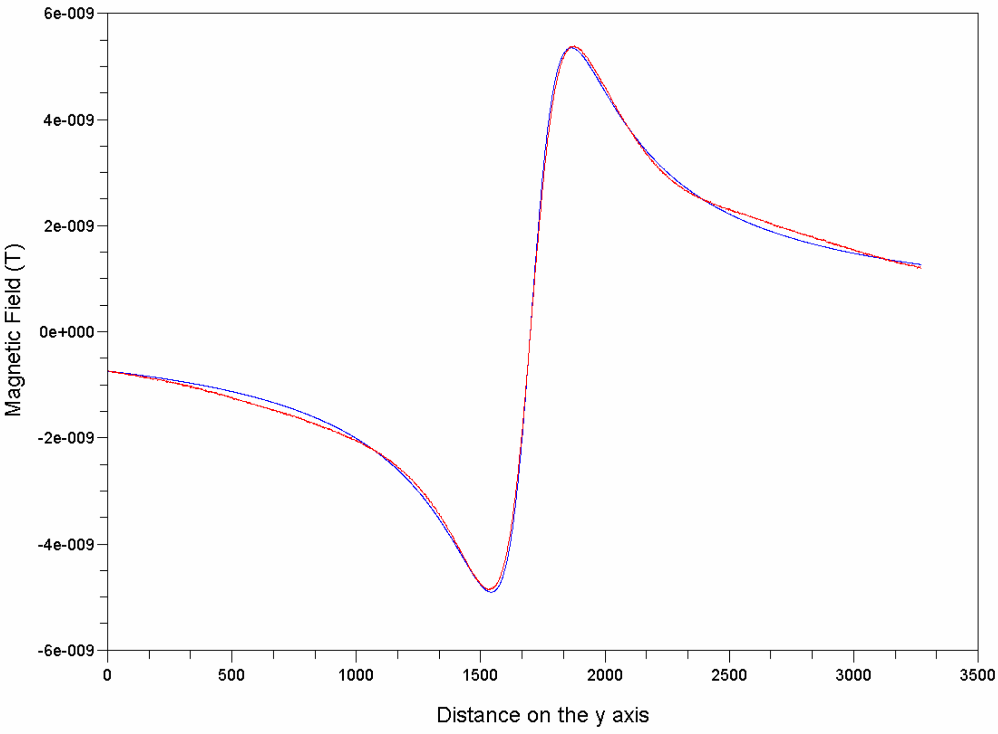

Figure III.3.7: Acquisition of the magnetic field (red) and fitted curve (blue)

In figure III.3.7 an example of line fitting is shown. The red curve is the magnetic acquisition above the current line, in a direction perpendicular to the line itself, while the blue curve is the result of the fitting algorithm. The resulting z value, in this case, is of $834\mu m$.

III.3.2 Current line localization

The simplest case for the currents localization is that of an infinite current line. For this case, an extensive study was carried out in order to understand the limitations of the simulation method for current localization.

In order to evaluate the best resolution for the currents localizations at different working distances, a set of acquisitions were performed at different distances on a simple current line. What could be noticed is that the best resolution limitations were due to hardware imprecision (SQUID to camera calibration, motorized micrometric stages resolution) for very small working distances, while they were due to the small signal to noise ratio for long working distances.

A number of magnetic acquisitions were performed on the current line referred to above. The main aim of the analysis was to see which was the maximum distance for localizing a current, and on the other hand to find a relationship between the correlation and the working distance. The scans performed were carried out from distances varying from $100\mu m$ to $2cm$. $2cm$ was evaluated as the maximum that could be found on a packaged three-dimensional Integrated Circuit.

III.3.2.1 Better localization accuracy

By working in this way, it was possible to increase remarkably the resolution of the Magnetic Microscopy technique, which would not be possible by using the MCI algorithm [69].

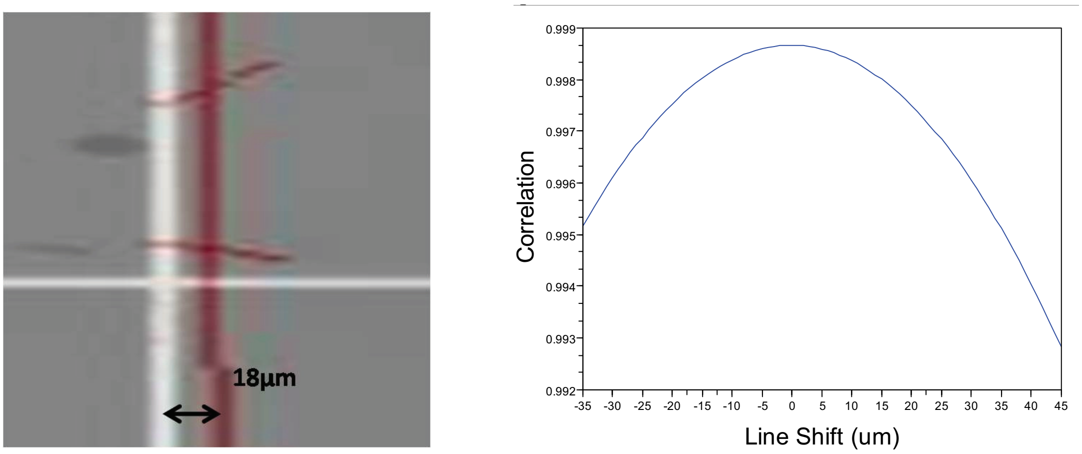

Figure III.3.8: Distance between the MCI result and the current line (left), and simulation results (right)

In figure III.3.8 an example of the improvements obtained is shown. On the left side an MCI analysis performed on a single current line is shown; the superposition of the optical acquisition with the result of the current inversion can be seen. The acquisition is taken from a distance of $320\mu m$ for a current amplitude of $1mA$. The MCI shows an error of $18\mu m$; in addition, this error increases exponentially with the working distance, so that if the object needs to be scanned from a great distance, the error will not be acceptable at all. Therefore a set of simulations of a current line were produced, positioned with different shifts on the x axis. The results are shown on the right side of figure III.3.8; the maximum of the correlation is exactly at the origin of the x axis, as this was chosen to be the curve reference. When this curve is superposed to the optical image of the magnetic acquisition, its maximum (the origin) is located precisely on top of the white line, which is the current track. Therefore, in this particular case, the accuracy of the technique was increased by 18 times.

III.3.2.2 Results

Working distance	Lines displacement	Localization accuracy
$100\mu m$	$3\mu m$	$1\mu m$
$250\mu m$	$10\mu m$	$1\mu m$
$320\mu m$	$18\mu m$	$1\mu m$
$500\mu m$	$11\mu m$	$1\mu m$
$750\mu m$	$5\mu m$	$1\mu m$
$1mm$	$15\mu m$	$1\mu m$
$2mm$	$30\mu m$	$5\mu m$
$5mm$	$50\mu m$	$5\mu m$
$7.5mm$	$30\mu m$	$10\mu m$
$1cm$	$20\mu m$	$10\mu m$
$1.2cm$	$130\mu m$	$30\mu m$
$1.4cm$	$300\mu m$	$50\mu m$
$1.6cm$	$300\mu m$	$50\mu m$
$1.8cm$	$-100\mu m$	$50\mu m$
$2cm$	$-400\mu m$	$50\mu m$

Table III.3.1: Lines displacement and localization accuracy in function of the working distances

As previously stated, the scans were performed from a distance of $100\mu m$ to $2cm$. The results of the current localization for a set of measurements can be found in table III.3.1. It has to be noted that, as the SQUID gets further away from the current, the optical acquisition is shifted more and more from the magnetic measurement, so that the MCI would soon not be applicable anymore.

Moreover, the simulation approach allows the mapping of currents up to $2cm$ away from the SQUID; the MCI, on the other hand, is not working anymore for working distances higher than a few millimeters.

In the figures III.3.9, III.3.10, III.3.11 and III.3.12, the evaluations of the correlation for some of the performed acquisitions are shown. The maximum of the curve is always placed on top of the real current line; however, it can be noted that the distance between the maximum and the origin of the x axis increases with the working distance. This means that the the difficulty of getting accurate current map superposed to the samples optical images becomes more and more complex, even though the resolution of the technique is increased.

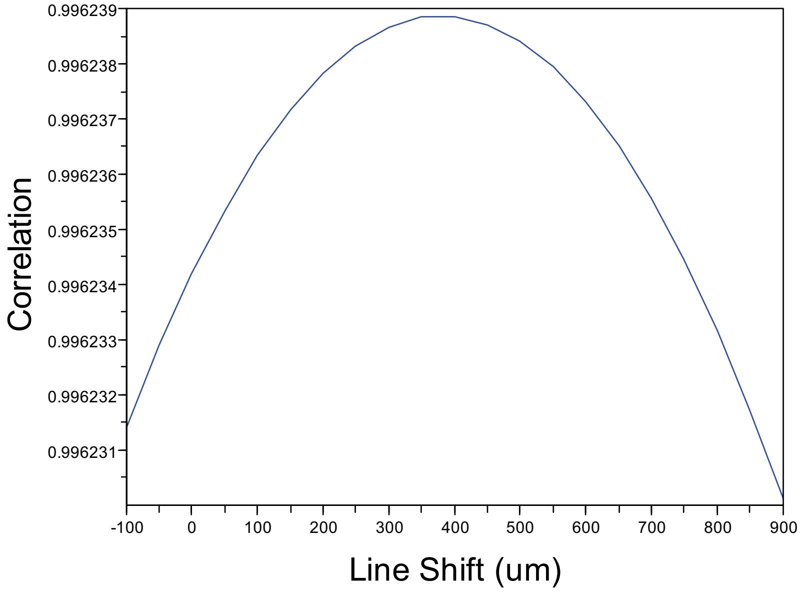

Figure III.3.9: Correlation between simulations and the measurement for a 100μm working distance

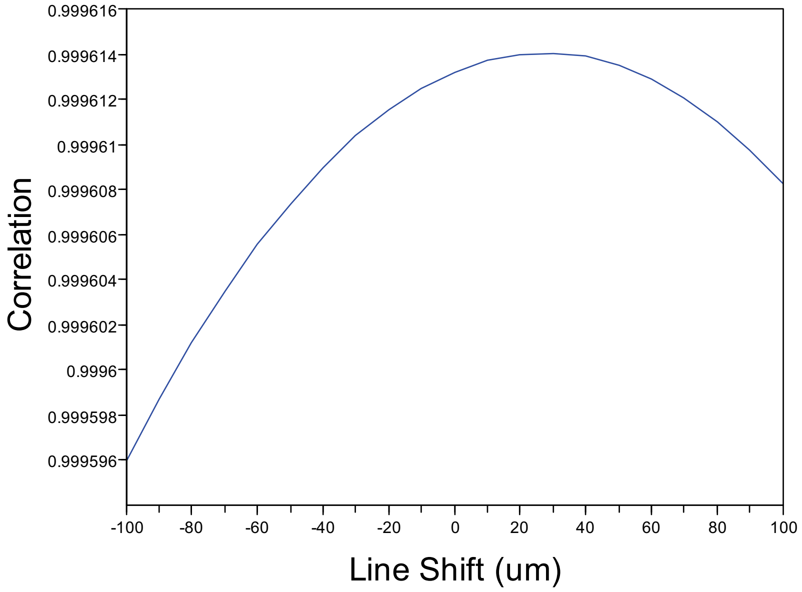

Figure III.3.10: Correlation between simulations and the measurement for a 750μm working distance.

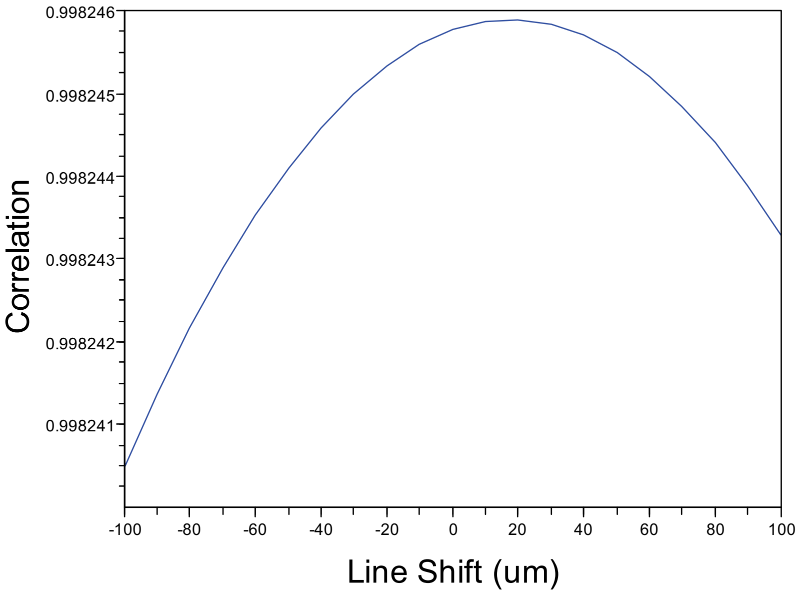

Figure III.3.11: Correlation between simulations and the measurement for a $1cm$ working distance.

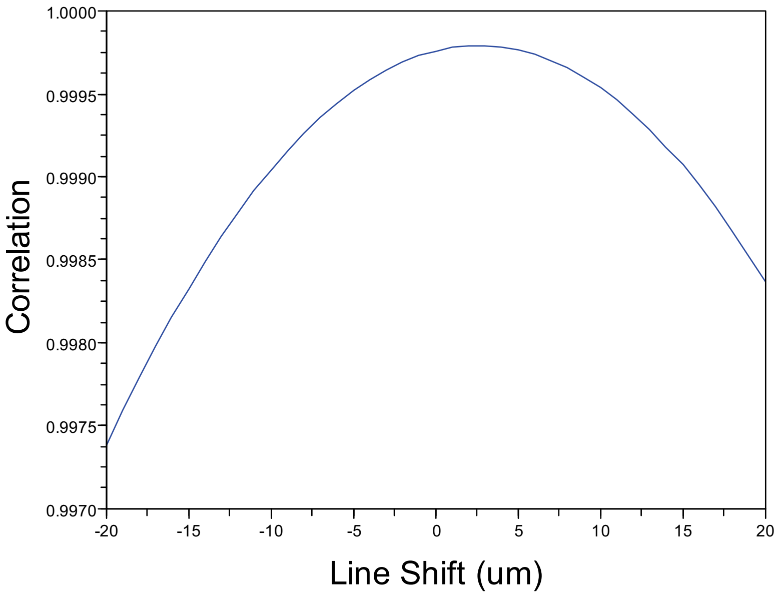

Figure III.3.12: Correlation between simulations and the measurement for $2cm$ working distance.

III.3.3 Conclusion

It has been shown in the previous sections that the MCI technique has some limitations. Those are mostly due to the number of operations which are necessarily performed on the magnetic field acquisition in order to obtain the desired map of the currents, as explained in II.2. When applying the inversion algorithm, the magnetic field is filtered of its higher frequencies, which still carry important information about the position of the sources.

These limitations can be overcome by using the simulation approach, as has been shown. In the next chapters it will be shown how this new approach can be used not only to improve standard technique resolution, but also to gather important information to reconstruct three-dimensional current paths.

CHAPTER III.4

Application to the 3D

In chapter III.3 it has been shown already how the model developed in chapter III.2 can be used to find some depth information about the current lines. Furthermore, in chapter II.1 it has been shown how impossible it is to to obtain information about the vertical currents when measuring the z component of the magnetic field, as they do not give any contribution in z. Finally, in chapter II.2 it was shown how the inversion problem is of no unique solution for three-dimensional current distributions: there exist more than one configuration of magnetic sources which generate the same distribution of the magnetic field, if this is measured above all the sources.

As a result, the first step to map the currents in a three-dimensional way is that of acquiring the other components of the magnetic field. These are the only ones generated by a current flowing in the z direction. This is however only a first step, as it is not sufficient to map all the currents, as the MCI technique is not suitable for the three dimensions.

III.4.1 Tilting the sample

There are a few reasons for which the Magnetic Current Imaging algorithm is not able to map the currents in three dimensions. The first, and most obvious, is that the acquired z component of the magnetic field does not carry any information about vertical currents. Moreover, the 3D problem, as explained in chapter II.2.3, has no unique solution, which means that there is no way to map the currents three-dimensionally.

III.4.1.1 Currents projection

In figure III.4.1 the problem of the three-dimensional nature of the currents is schematized. The currents, which can be seen from the measurement plane, can be considered as projected to this plane. Further-

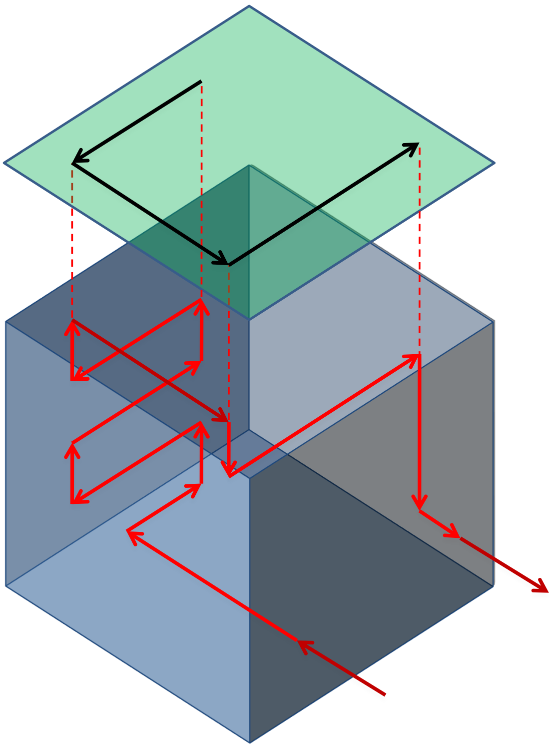

Figure III.4.1: Projection of the current lines on the measurement plane

more, the intensity of the projection decreases with the square value of the distance: the only currents which will be visualized with the MCI algorithm are only those flowing on the surface. It also has to be noted that the projection of the vertical currents on the measurement plane is only a point.

III.4.1.2 Projections on the tilted sample

If the sample of figure III.4.1 is tilted, the resulting measurement plane will be moved as in figure III.4.2. In this case all the currents flowing inside the sample have a projection on the measurement plane. Furthermore, there are no currents whose projections are overlapped as in the previous example. In this case, the vertical currents also can be mapped.

It has to be noted, however, that from a general point of view, the currents can be flowing on any direction on the three axes. In any case, the multiple measurements on three measurement planes, as it will be described in the next section, assure a full view of all the currents, in each direction. In real samples, on the other hand, the currents do not usually flow diagonally inside them. The currents are

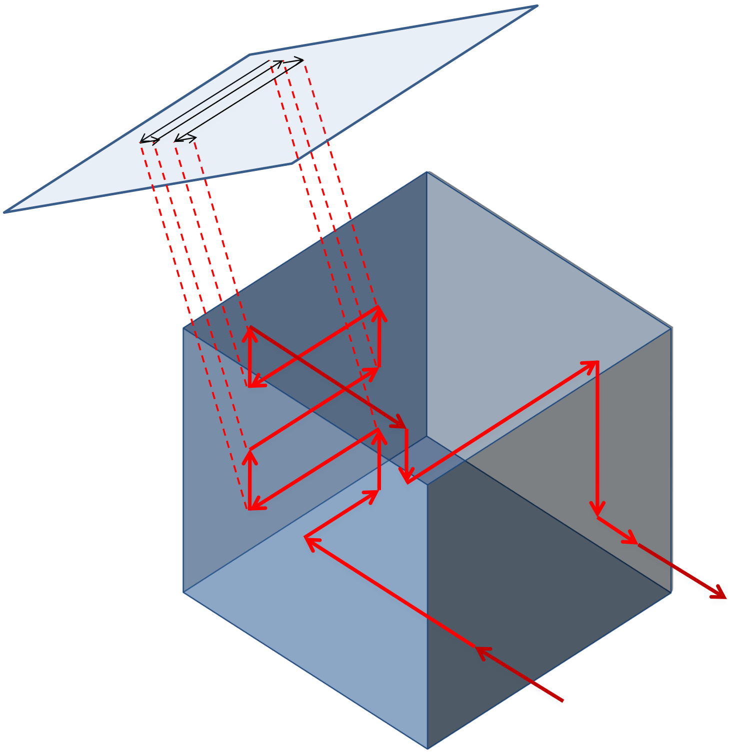

Figure III.4.2: Projection of the current lines on the measurement plane for a tilted sample

usually moving on either x or y directions inside a z plane (even if sometimes they might flow in a general direction in the plane), but most surely they move from z layer to z layer only in the z direction.

III.4.2 Full Magnetic Field acquisition

The SQUID sensor which was used for this study, like all the magnetic sensors normally used for the purpose of non-destructive studies, is only built to measure the z component of the field. In order to acquire the other components of B the sample needs to be tilted on two different axes separately, so that three consecutive acquisitions need to be performed.

III.4.2.1 Acquisition of the z component

To obtain the z component of the magnetic field, a first magnetic scan is performed on the top of the sample, which is placed flat under the SQUID, as it is shown in figure III.4.3.

In figure III.4.4 the acquisition of the z component on a real sample is shown. This is a standard acquisition, which can also be later used to apply the MCI algorithm and obtain some initial information about the currents flowing on the surface.

III.4.2.2 Acquisition of the x and y components of B

The x and y components of B can be acquired by tilting the sample as shown in the image III.4.5.

The angle that the device will be tilted depends on its geometry. If the sample is very wide, a narrow angle is preferable to avoid losing resolution due to the increased working distance. For smaller devices a wider angle can be used to allow for a better filtering of the the unwanted component of the magnetic induction field.

If, for example, the sample is tilted by an angle Θ on the x axis as shown in figure III.4.6, by applying the rotation matrices on the x axis, the measured field B_M will be:

$$B_M = -B_y \sin\Theta + B_z \cos\Theta \tag{III.4.1}$$

If the z component has previously been measured, the y component can then be easily extracted:

$$B_y = \frac{B_z \cos\Theta - B_M}{\sin\Theta} \tag{III.4.2}$$

The same equation applies for the x component of the magnetic induction field. If the sample is tilted by an angle Φ on the y axis as shown in figure III.4.7, the measured field B_M will be:

$$B_M = B_x \sin\Phi + B_z \cos\Phi \tag{III.4.3}$$

and therefore the x component of B can be evaluated as follows:

$$B_x = \frac{-B_z \cos\Phi + B_M}{\sin\Phi} \tag{III.4.4}$$

In figure III.4.8 the projection of the cube on the $y - z$ plane before and after it is tilted on the x axis is shown. In this way it is possible to see how the y component of the magnetic induction field can be extracted when the sample is tilted on the x axis by an angle Θ.

III.4.3 Use of the gathered information

The information which was acquired with the three components of the magnetic field needs then to be put together. In most of the cases, acquisitions of the three components are not performed exactly at the same points, even though some data analysis would allow the transfer of such acquisitions to the same points.

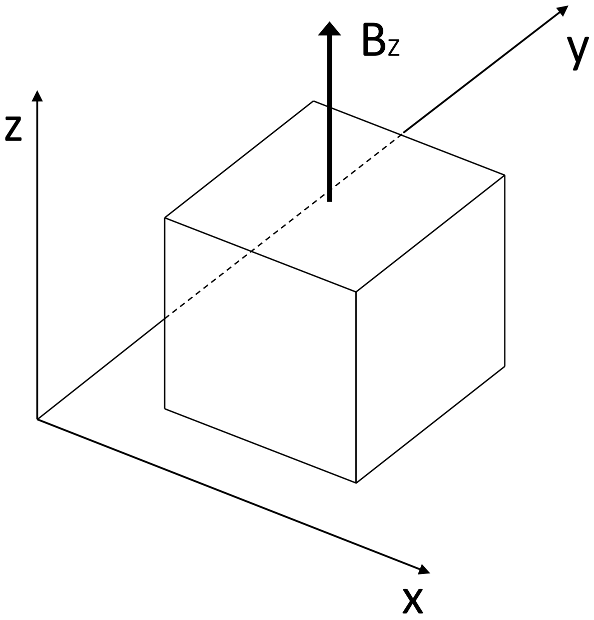

Figure III.4.3: z component of the magnetic field

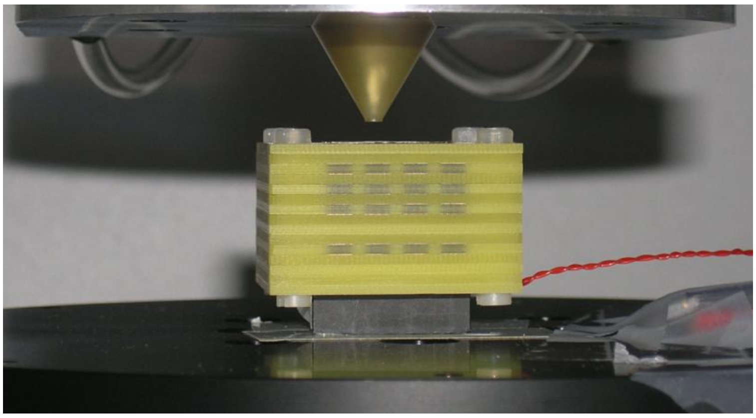

Figure III.4.4: Image of the SQUID measuring the z component of B

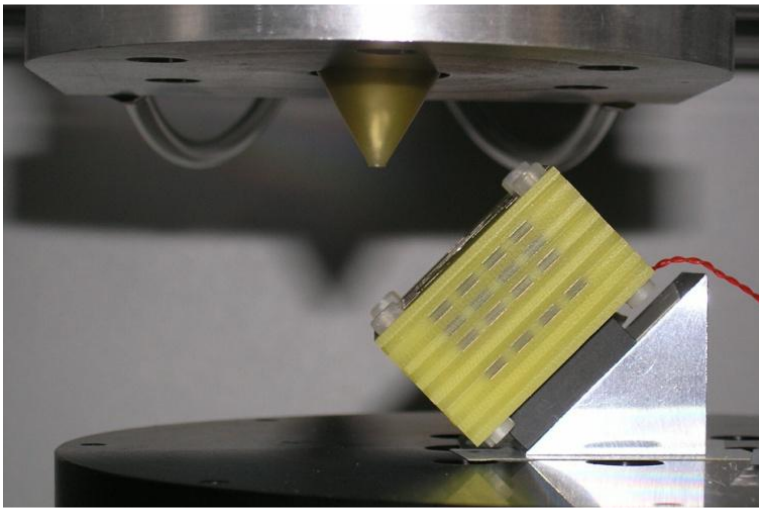

Figure III.4.5: Image of the SQUID scanning above a tilted sample

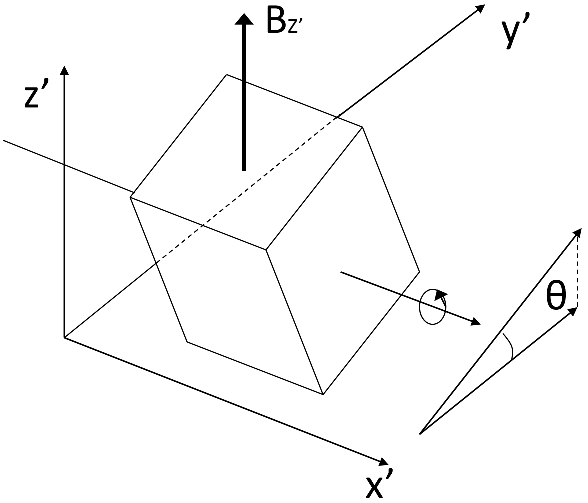

Figure III.4.6: Sample tilt on the *x* axis

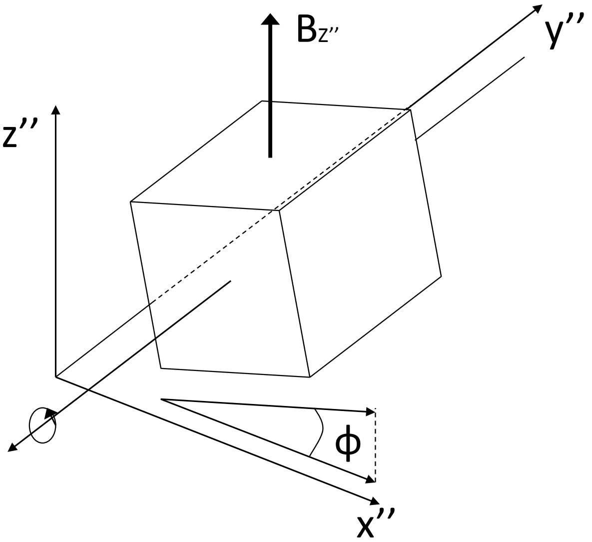

Figure III.4.7: Sample tilt on the *y* axis

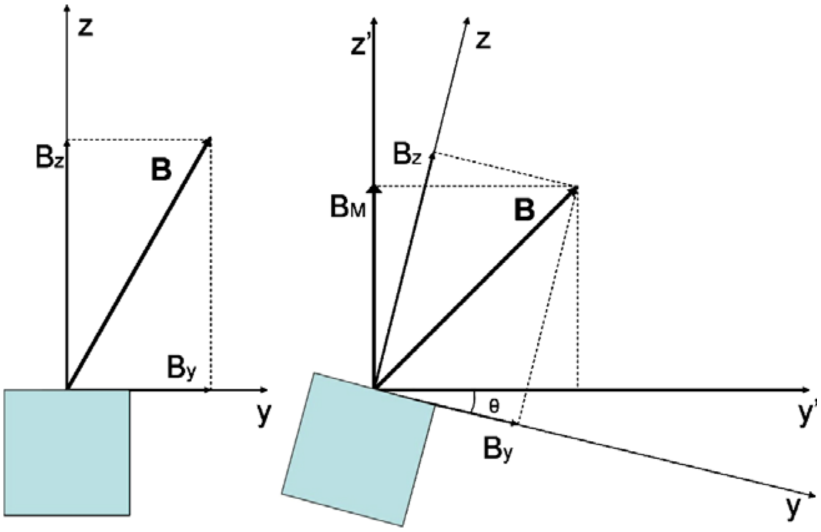

Figure III.4.8: Projection of the sample on the $y - z$ plane

The process, from a theoretical point of view, would be quite simple: it is the same as the one used by the technique called the "Inward Continuation", which has been briefly explained in II.2.3.1. The difference here is that the plane where the magnetic field is evaluated would not only need to be translated on the z axis, but also rotated and tilted. In other words, the easiest solution would be that of evaluating b_z of equation II.2.24 at each x, y point with a different z_2 value. And still some interpolation adjustment would be needed to evaluate the field in the exact same x, y positions as the reference acquisition. However, even if this method would provide a full data set of the magnetic field on a known $x - y$ plane, the data transformed in this way would not give any additional information about the currents when using a Simulation Approach: the noise of the measurement would be moved together with the movement itself. The Simulation Approach can evaluate the same field components of the magnetic acquisition on the same measurement planes.

CHAPTER III.5

The Ground Plane problem

The MCI technique has proven very useful in the localization of defects on bi-dimensional devices. Its great potentialities have already been discussed elsewhere in this document. However, in the presence of large metallic areas where currents are flowing, the MCI shows some strong limitations. This is the exact case of the presence of ground planes.

Up to now, it is still impossible to localize currents which are flowing inside wide areas such as leakages in the ground plane. In this case the current density at each point is very small; therefore, the MCI algorithm cannot be applied, as the overall magnetic induction field generated is not strong enough compared to noise.

III.5.1 The presence of the ground plane

Any operating electrical system can both emit and be subjected to perturbations, whatever their origin (electromagnetic, electrical, environmental noise etc.). Electronic and microelectronic components are no exception to this rule. Ground planes are used to determine the electrical reference of the assembly. The presence of a ground plane reduces the cross-talk (e.g. the pollution of an electrical signal by the presence of a second signal), electromagnetic interference and increases noise isolation. In a system with an analog and a digital part, two different ground planes are expected to provide two different references and therefore somewhat isolate the two parts. The ground plane, which has a local short circuit, poses a dramatic problem that can lead to the total destruction of the Integrated Circuit or component.

An example of a multilayer component, presenting a ground plane, is shown in figure III.5.1.

III.5.2 MCI for ground planes

One of the drawbacks of MCI techniques is the inability to generate cartographies of currents when they are distributed on a bi-dimensional plane. This happens when there is a current leakage on a ground plane, either at PCB or SiP level. When a current flows inside a conductor, the amplitude of the current distribution is inversely proportional to the width of the conductor itself. This means that when the current flows from a track or bonding wire to a ground plane, the current is widely distributed. Therefore the magnetic field generated by such a current is widely spread and very weak. When applying the MCI algorithm, a magnetic field, which is strong enough to visualize the current is needed. This is not the case for currents flowing inside ground planes. An example of a ground plane current is shown in figure III.5.2: here the only currents visible, after applying the MCI technique, are those flowing in and out of the plane. There is no way to visualize the currents inside the plane.

III.5.3 The simulation approach for the Ground Plane

The simulation model which has been developed throughout this document cannot unfortunately be applied to a ground plane, as it takes into account only current lines and not bi-dimensional current distributions.

This model is very useful as long as the currents flowing inside the system are all filiform. As soon as one or more currents leak inside a ground plane, the approximation of the current distribution to a line is no longer valid. For these cases, a similar approach has been developed, which is based on the discretization of a bi-dimensional current distribution as a network of resistors. The number of nodes used depends directly on the degree of precision required and is inversely proportional to the time needed to evaluate the solution. Once the entry and exit nodes of the net are chosen, Kirchhoff's circuit laws give the unique solution, which is the amplitude of the current flowing in each branch. With this information it is possible then to generate the magnetic field for each line. Then, by using the superposition principle, all the single contributions are added up in order to obtain the magnetic field generated by the whole plane.

An example with a small number of nodes is shown in figure III.5.3. Here it can be seen how a current flow is discretized with one entry and one exit point on a plane. The advantage of this approach is that to increase the number of nodes (in order to increase the technique resolution), it needs just to increase the dimensions of the matrices used in the solution equations.

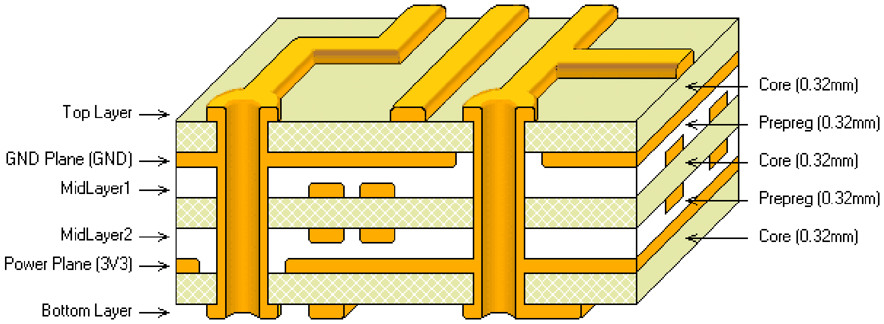

Figure III.5.1: Example of a multilayer component

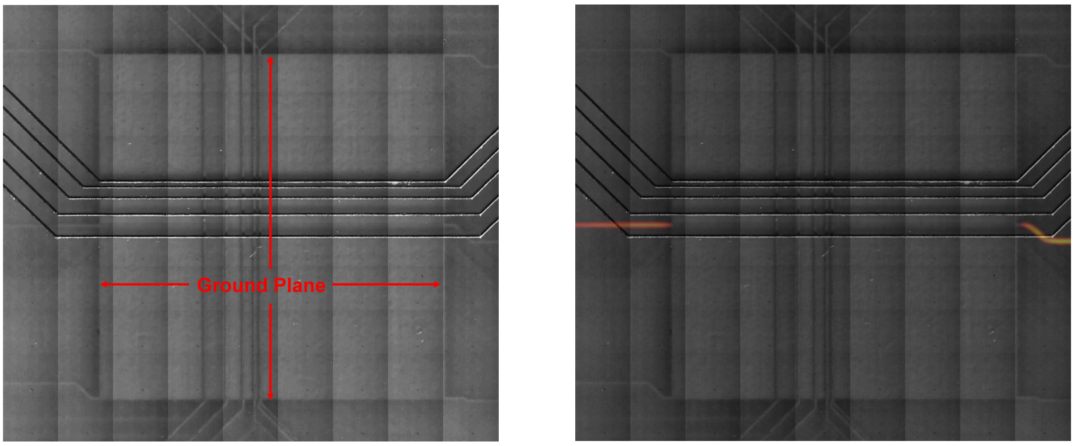

Figure III.5.2: Optical view of a ground plane (left) and the MCI results (Right)

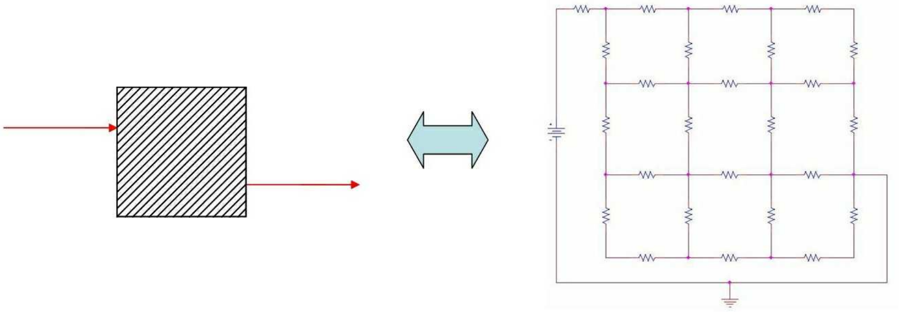

Figure III.5.3: Modelization of the Ground Plane

III.5.4 Wires network model

It is therefore necessary to prove the capability to model a ground plane as a wired network in order to estimate the leakage currents or short circuits. The starting point of this modeling is to generate a simple model in order to make the simulations as cheap as possible in terms of time. This model is valid as long as the wavelength of the signal is not of the same magnitude of the thickness of the tracks.

III.5.4.1 Resolution methods

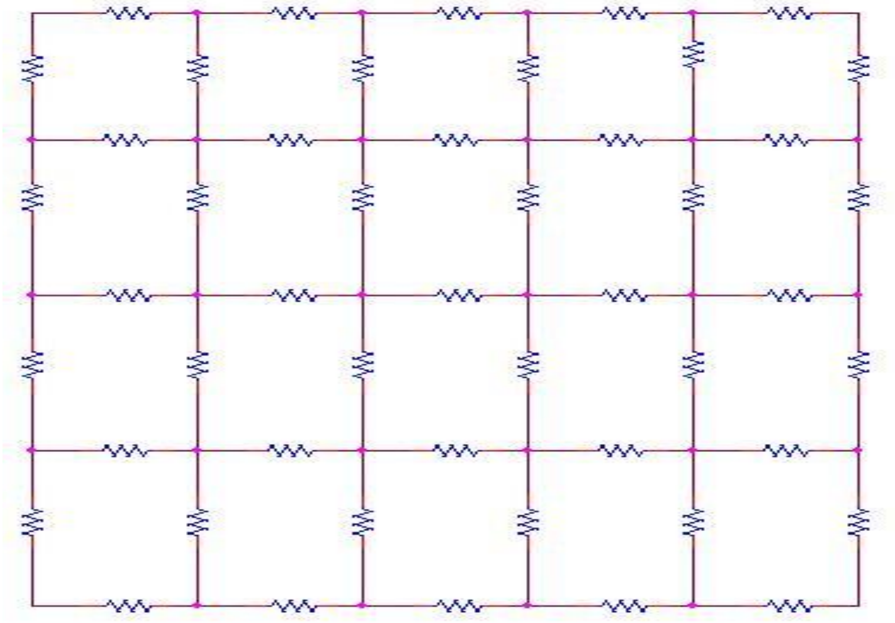

Figure III.5.4: Resistor network

The first step, once the Ground plane has been discretized as a network of resistors, is to evaluate the current flowing on each branch. To do that, there are two main methods which can be used: the Mesh Currents and the Node-Voltage. The Mesh Currents method would be the easiest and quickest to implement, as it would directly give the current values as a result. However, this method cannot take into consideration three-dimensional structures: in other words, if one of the contact points is a node in the middle of the network, this method is not applicable anymore. This would be the case of a vertical connection which short-circuits the ground plane on a generic point in its middle. This scenario can be taken account in the Node-Voltage analysis, which is therefore the one which will be used.

III.5.4.2 Node-Voltage Analysis method

A typical ground plane resistors network is shown in figure III.5.4. Then, between two or more points, a current generator can be applied in order to bias the structure. If there are n nodes, and the exit point for the current is the node n, the node voltages $V_1, \dots, V_{n-1}$ for the other $n-1$ nodes can be evaluated as follows:

$$\begin{bmatrix} a_{1,1} & a_{1,2} & \cdots & a_{1,(n-1)} \\ a_{2,1} & a_{2,2} & \cdots & a_{2,(n-1)} \\ \vdots & \vdots & \ddots & \vdots \\ a_{(n-1),1} & a_{(n-1),2} & \cdots & a_{(n-1),(n-1)} \end{bmatrix} \begin{bmatrix} V_1 \\ V_2 \\ \vdots \\ V_{n-1} \end{bmatrix} = \begin{bmatrix} b_1 \\ b_2 \\ \vdots \\ b_{n-1} \end{bmatrix} \tag{III.5.1}$$

where, knowing that the conductance is the inverse of the resistance:

- $i = j : a_{i,j} = -\sum$ conductances which have one end on the i$^{\text{th}}$ node
- $i \neq j : a_{i,j} = \sum$ conductances between the i$^{\text{th}}$ and j$^{\text{th}}$ nodes
- $b_i = -\sum$ current generators which have one end on the i$^{\text{th}}$ node

III.5.4.3 Node-Voltage method solution

As the ground plane is made up of just one homogeneous material, the resistors of the network can be considered as all having the same resistivity R, corresponding to the conductance Y. It is easy then to recover the values for the $a_{i,j}$ variables, as the number of resistors connected to one node goes from 2 on the four corners, to 3 on all the sides, up to 4 for all the middle nodes.

By inverting equation III.5.1 it is then possible to obtain the node-voltage values for each node. The currents flowing on the resistors are then easily evaluated by:

$$I_{i,j} = \frac{V_i - V_j}{R} \tag{III.5.2}$$

for all the nodes which have a branch in common, and it is zero for the others.

III.5.4.4 Evaluation of the magnetic field

Once the currents, with their physical positions, have been evaluated, they can be inserted in the simulation model developed in chapter III.2. Each current line then generates a magnetic contribution; all the contributions are then added together using the superposition principle.

III.5.4.5 Application to the Simulation Approach

This method is used to perform a set of hypotheses on the entry and exit points of the current inside the Ground plane. All the hypotheses are then simulated using the discretization technique; this process is quite time consuming, depending on the level of precision which is required by the problem. Once the hypotheses are simulated, they can be compared to the magnetic acquisitions previously taken on the sample. The hypothesis with the highest correlation will be the most probable current path.

CHAPTER III.6

The Simulation Approach process

The simulation approach has been explained in the previous chapters: in chapter III.2 it has been shown how to generate a fast and reliable simulation of the magnetic field, which would comply with both time and precision constraints given by the defect localization problem. This model can then be used to localize current lines with high precision, as explained in chapter III.3. It can then be used to overcome the standard limitations of the MCI technique, which, for the sake of the visualization, is obliged to omit some of the important information. Furthermore, once the mathematics of the simulation have been developed, it takes only one step more to use them for three-dimensional current paths. The current lines which need to be simulated do not necessarily need to have all their points at the same vertical level. Current lines can be simulated even if flowing in an arbitrary direction. The same possibility applies to the magnetic components: by multiplying the evaluated field modulus to the right unity vector, the simulation software is able to generate any component of the magnetic field. The problem of the measurement of such a field is presented in chapter III.4. The easiest and fastest way for carrying out the measurement is to tilt the sample and obtain the other components. The drawback of such approach is that if the sample is very wide, even a small tilt will result in a long working distance in one side of the surface. In some cases, however, the solution is to perform an acquisition of the field on the sides of the sample. That is the flexibility given by the Simulation Approach: any and each magnetic scan, either on top or on the sides, tilted or flat, far from or close to the sample, can be used and can add part of the information to the global model. The simulation software, in fact, can generate the field on any possible plane.

In this chapter, the steps to get a full current map will be summarized with the help of two flowcharts. However, it needs to be understood that a real, precise and complete process flow for such a complex problem does not really exist. This is due to the fact that every localization problem is unique in itself, and will follow its own steps depending on too many parameters.

III.6.1 Defect localization process including the Simulation Approach

The process presented here is close to a typical defect localization application. In part IV some examples of successful defect localizations will be given: it will be clear then that not all the steps of the process are performed, but just those which were necessary to reach the goal.

III.6.1.1 First acquisitions

The defect localization problem starts when the electrical test has shown the characterization of the component malfunctioning. Depending on the test output, the search will address a short circuit, an open circuit, a resistive open or a general current leak. The first step will be to obtain enough information about the internal structureof the component. This information can be gathered in different ways: the easiest is to take some pictures of the sample, and to superpose them to the magnetic acquisitions. This method is mostly suitable when the component has already been de-packaged, and the electronic die is directly exposed to the camera. In addition, the user might have useful information about the sample layout. This can be used later to define the paths where the currents are allowed to flow. Finally, some important information can be obtained from X-Ray acquisitions, both bi and three-dimensional, as explained in section I.3.2. The three imaging processes can be used separately or coupled, and need to be realigned together and to the magnetic field acquisitions.

A first set of magnetic scans is then performed. This step is generally iterated until the desired precision is reached. Each magnetic scan is followed by the application of the Magnetic Current Imaging algorithm, which allows the visualization of the currents flowing on the surface of the sample, and which will be the starting point for the generation of the simulations. In some standard cases, this first set of MCI applications will lead directly to the localization of the defect. This happens mostly for bi-dimensional components presenting a complete short circuit, and which do not need a better localization accuracy as the defects are considerable. These standard cases are however not the topic of this work.

III.6.1.2 Full Magnetic Field acquisition

If it is necessary to apply the Simulation Approach, there will then be a first separation between bi-dimensional and three-dimensional components. In the first case, the acquisition of the z component of the magnetic field is usually enough to obtain the desired solution, so that the Simulation Approach can be directly applied. For the three-dimensional components, it will be necessary to acquire the other components of the field.

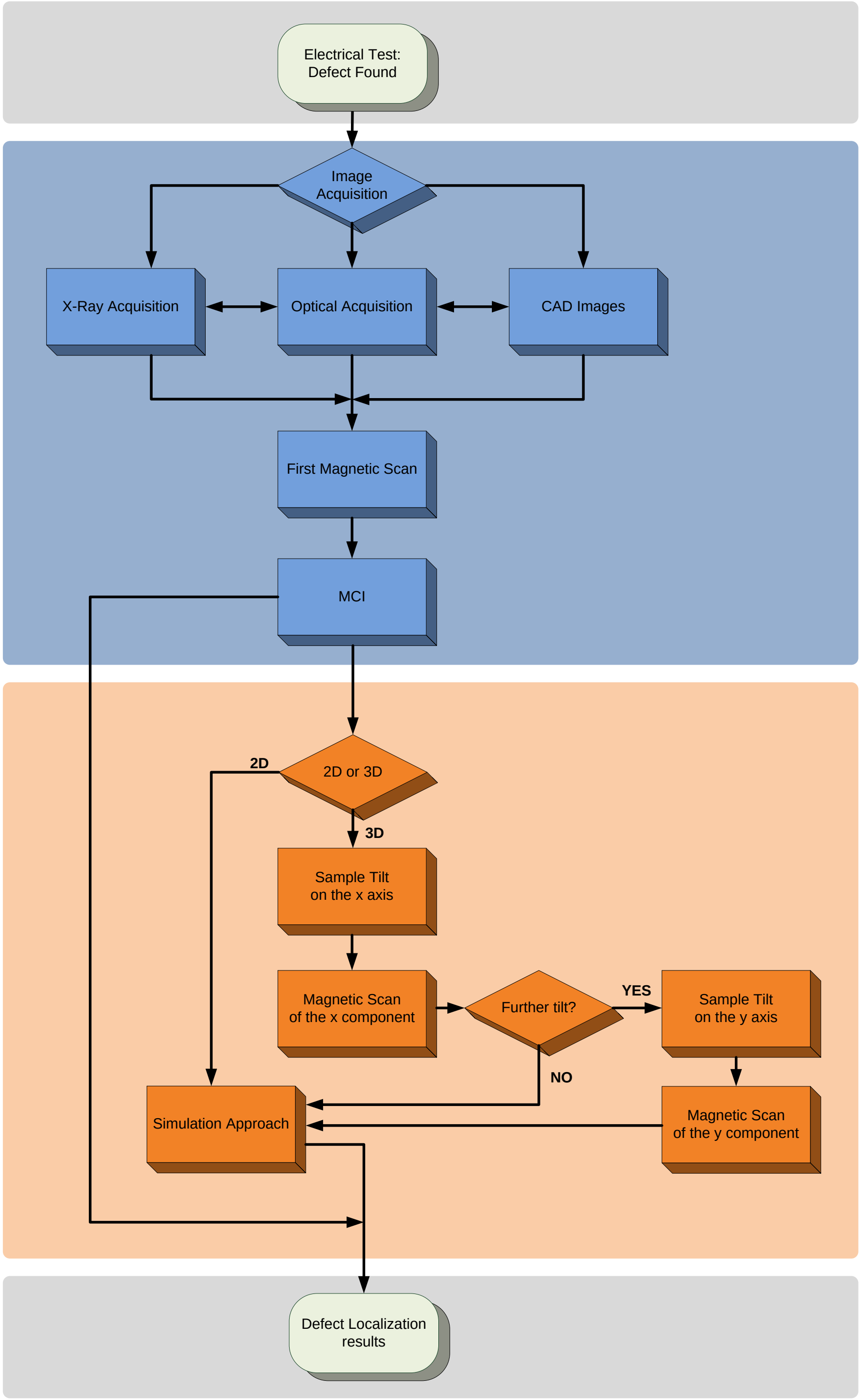

Figure III.6.1: Process flow for the application of three-dimensional magnetic microscopy

A first tilt, performed on the x axis (for the sake of simplicity, the case where it is better to first perform a tilt on the y axis will not be shown: the results are exactly the same, only with the inverted axes), is followed by a magnetic scan. This scan will give a combination of the z and y components of B. The tilt angle will be chosen as a compromise between noise level for the measurement and long working distance. For big angles, in fact, the points of the samples which will be positioned further away from the x axis, will have a high working distance. For small angles, the ratio between B_y and B_z will be too small: the y component will not have a Signal to Noise Ratio high enough. As stated before, this angle will be chosen depending on the size of the sample.

This first tilt might be enough, in some cases, to obtain the required information. Again, this is strictly dependent on the chosen sample. For the most complex cases, however, a third and final magnetic scan will be performed, after a second tilt of the component, this time on the y axis. The Magnetic acquisition will allow the extraction of the x component of B. Again, the chosen angle will be a compromise, and depends on the sample geometry.

Finally, when all the magnetic acquisitions are performed, the Simulation Approach will be applied.

III.6.1.3 Localization results

The Simulation Approach, which will be expanded in the next section, gives the path followed by the current in three dimensions. Very often, this is enough to obtain the precise localization. Sometimes, the discovered current path will need to be compared to that of a reference working device.

III.6.2 Simulation Approach process flow

As seen in the previous section, for complex defect localization cases, it is necessary to apply the Simulation Approach described in chapters III.2, III.3 and III.4 to generate a full and reliable current path reconstruction. This approach is very flexible, and it too depends on the specific device which is being studied: some of the steps might be entirely bypassed, while some others could be performed more than once. It is anyway possible to describe the methodology by following the typical process flow which is shown in figure III.6.2. All the steps will be better explained hereunder.

III.6.2.1 MCI algorithm applied to the top layer

This first step, if not completely necessary, is really useful as it gives, in the case of bi-dimensional samples, a first layout of the currents flowing in the device. For three-dimensional components, it can give a more or less precise layout of the currents flowing on the plane which is closer to the sensor. The information gathered by this step can be used as a first constraint for the simulation model: it is the starting point from which the simulation can be applied.

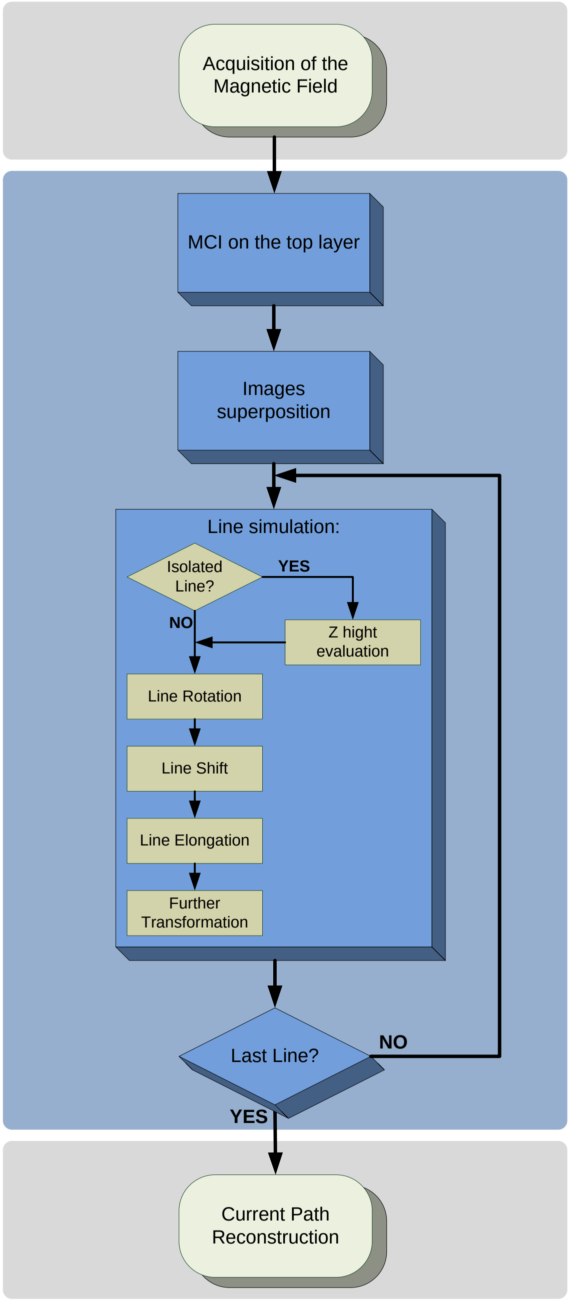

Figure III.6.2: Process flow for the Simulation Approach

III.6.2.2 Superposition of the acquired images

The first magnetic acquisition followed by a MCI calculation can also be used to overlap the first optical images to the current layout. This is also the step where all the available images are superposed on each other to obtain a deeper knowledge of the device. This superposition will be necessary once the points of the lines to be simulated have been selected. For instance, an X-Ray image, superposed to the magnetic acquisition, can be used to select the points of the structure which are not visible from the outside, when the sample is still packaged.

III.6.2.3 Line Simulation

As shown in figure III.6.2, this step can be still divided in sub-steps. The line which is being studied and therefore mapped can undergo a certain number of transformations, as explained in III.3.1. The steps proposed in this mini process flow are not necessarily to be applied in the same order. However, the proposed order is the one which is more suitable for most cases. The first line which will be chosen to be mapped depends again on the sample geometry; in most cases, the study starts with the currents which are closest to the sensor.

If the current line which needs to be localized is sufficiently distant from other currents, e.g. there is at least part of it which does not have much influence from other neighbor current lines, the vertical depth simulation described in the section III.3.1.5 can be used in order to place the current in the right z plane. This information can be of fundamental importance as it places the current line under study in the correct layer of the sample. Following this step, all the transformations can be applied to the current line in order to maximize the correlation. As the rotation of the current line is usually already known (normally the current travels on either the x axis or the y axis), the first transformation is usually a line shift (from section III.3.1.1). With this step the line is precisely placed on top of the metal track. A further rotation, as explained in section III.3.1.2 could slightly increase the correlation, and can be used to adjust the current on the precise orientation of the image. In some rare cases, however, currents might be flowing in a complete arbitrary direction in the plane: in these cases, a first rotation transformation is performed before the shift. Finally, the current line is adjusted in its length: the two extreme points are moved in their axes as shown in section III.3.1.3, until a maximum in the correlation is found. These steps can then be re-performed one by one to readjust the current until a stable solution, which is a compromise of all the transformations, is found.

III.6.2.4 Simulation of the following current lines

The mini process described in the previous section is then iterated for each current segment flowing inside the sample. All the current segments which have already been simulated will be taken into account by adding together all their contributions to the magnetic field. The overall correlation therefore should keep increasing until reaching a value close to 1, when the last current line is simulated and its contribution on the magnetic field has been added to that of the other segments.

III.6.2.5 Full current path reconstruction

The final goal of the Simulation Approach is then reached: the full current path flowing inside the sample can be reconstructed three-dimensionally. This information can be compared with the internal structure of the sample given by either the X-Ray acquisition or the CAD layout, or in some cases it can be compared with the same map produced on a reference device: the difference between the two paths will give the precise spot of the defect location.

CHAPTER III.7

Conclusion

In this part the fast Simulation Approach, based on a line approximation of the current flow, has been developed. The possibility to measure B_x and B_y with a mono-dimensional sensor, dedicated to the measurement of B_z, by tilting the sample has been shown. Complex problems, including short circuits inside ground planes, can also be solved with this technique. The Simulation Approach has thus been implemented in a full process flow. Its efficiency will be shown in the next part, where it is applied in a number of case studies, and will be described in detail.

Part IV

Application of the new techniques to case studies

CHAPTER IV.1

Introduction

In order to understand the technique described in part III, some applications to real case studies will be described here. The goal is not only to illustrate the use of such a technique more clearly, but also to prove its validity for a wide range of different problems.

Therefore each example chosen here is propaedeutic to its successor, and show the progression from the standard bi-dimensional magnetic microscopy applied with the inversion technique, to the most advanced three-dimensional current reconstruction. The first chapter will show the application of the technique described in chapter III.5 which is used to simulate the bi-dimensional current distributions, such as those flowing in the ground plane of the circuits; the technique will be validated through the application on a test vehicle PCB. In the following chapters, the Simulation Approach will be applied to different cases, from a planar Integrated Circuit presenting a short circuit, to a real case multilayer defective System in Package from 3D-Plus. In the third example, the Simulation Approach will be applied to a test vehicle, which was used to show the proof of the ability of the technique to map the currents at very long working distances in the three dimensions.

CHAPTER IV.2

Ground Plane current localization on a test vehicle

It has been seen how the localization of bi-dimensional current distributions flowing on the ground planes are very complicated to map. This is primarily due to the small variation of the magnetic field on such planes, and of the low SNR value.

In this chapter a test vehicle, comprising a bi-dimensional metallic layer, is built and shown. The first use of the Simulation Approach on this type of devices is shown.

IV.2.1 Test Vehicle conception

The test vehicle which was built in order to demonstrate the validity of this technique is shown in figure IV.2.1. It is a multilayer PCB, with one of the layers presenting a square metallic plane, connected through some metallic tracks to the external pins. The metallic square is visible in transparency in figure IV.2.1.

IV.2.2 Magnetic Analysis

IV.2.2.1 Electrical setup

Through two of the electrical connections to the metallic plane, an AC voltage of a few mV was applied. This induced an AC current of a few mA in the plane. The chosen frequency used was of $5kHz$: with such small frequencies, the capacitive behavior of the plane can be neglected, and the plane can be therefore considered as an impedance network, where all the impedances have only their real value.

IV.2.2.2 Magnetic Acquisition

The first step, once the device was fed, was to perform an acquisition of the magnetic field generated by such a plane. The resulting map of the magnetic field is shown in figure IV.2.2: this image shows how the strongest magnetic signal is acquired on top of the tracks which are carrying the current to the plane, while the field on the plane itself is of much lower intensity.

IV.2.2.3 MCI algorithm application

The acquired magnetic field of figure IV.2.2 was then transformed according to the MCI algorithm; the resulting current map is shown in figure IV.2.3. It is clear, from this image, that the MCI algorithm is only able to produce information about the currents flowing in tracks which are narrow enough. In this case, only the currents flowing in the tracks are visible: the current distribution on the metallic plane does not give a big enough contribution to the magnetic field, and therefore cannot be visualized with the MCI technique.

IV.2.3 The application of the simulations

The simulation of the current flowing on the plane was generated as in chapter III.5: the metallic plane was discretized as a resistors network, and the current flowing on each branch was evaluated. The magnetic field generated by such currents was then calculated and compared to the acquisitions.

IV.2.3.1 Ground Plane discretization

A number of choices had to be made in order to generate the network of resistors. They mostly reduced to the choice of the step, on both x and y, between two successive resistors, in micrometers. The step, in this case, was of $100\mu m$ on both sides, creating a network of $n \times n$ resistors. Each simulation could then take up to 2 hours to perform.

IV.2.3.2 Defect hypotheses

In order to validate the approach, a few defect hypotheses were performed on the entry and exit points of the current inside the metallic plane. Some of the results obtained are shown in figure IV.2.4. When the simulated entry point is completely different from the real one, as in the first image on the left, the correlation is very low. On the other hand, when the simulation which was very similar to the real current distribution was performed, an increasing correlation was observed, with a maximum of 0.6 corresponding to the exact superposition of the simulation and the real current.

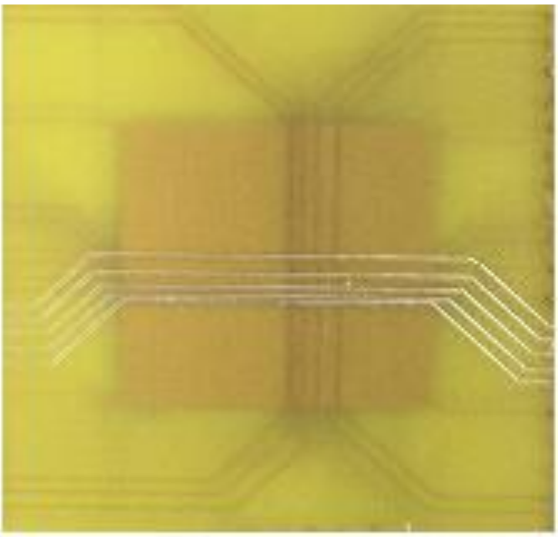

Figure IV.2.1: Optical image of the test vehicle

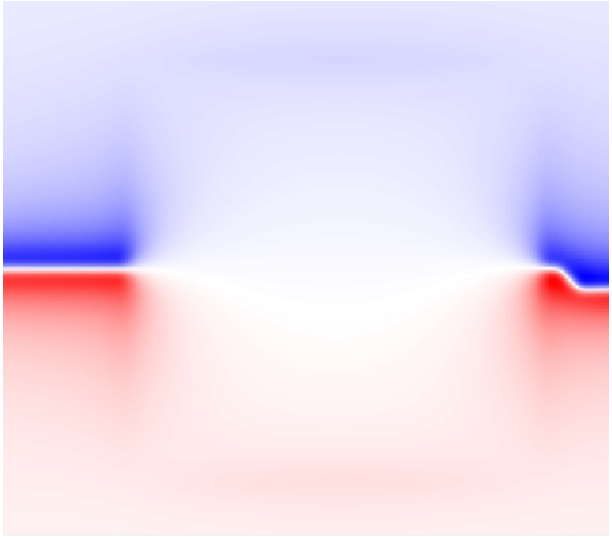

Figure IV.2.2: Image of the magnetic field acquired above the ground plane

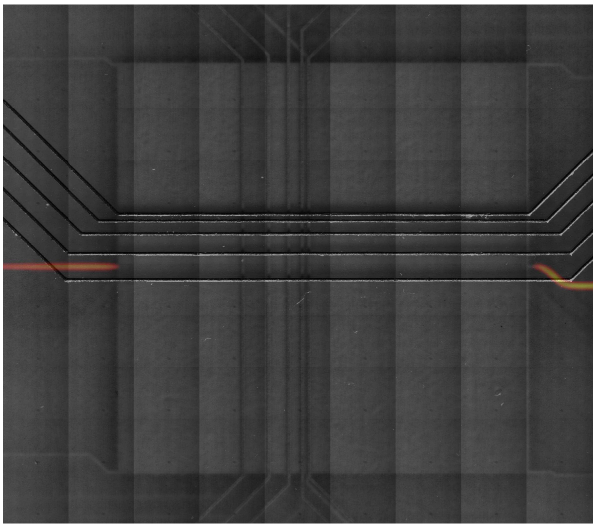

Figure IV.2.3: Current map as a result of the MCI algorithm

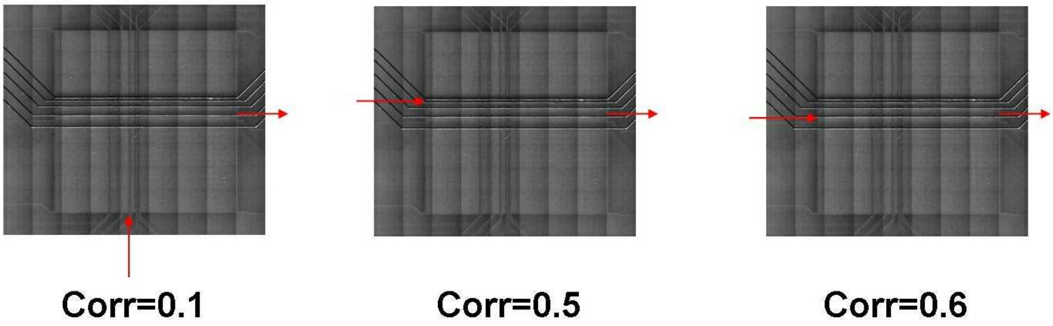

Corr=0.1

Corr=0.5

Corr=0.6

Figure IV.2.4: Ground plane currents hypotheses, with the relative correlation results

IV.2.4 Results

Figure IV.2.4 shows the correlation values for the comparisons between the simulations of the different current path hypotheses and the magnetic acquisitions. Even if the best correlation found, which was when the hypothesis perfectly matched the real current path, was far from the best possible value of 1, this was still a very good result. First of all, the highest correlation was shown on the real current, meaning that there is a correlation between the simulations and the measurements. And secondly, the correlation might have increased if all the currents had been simulated, not only those present in the plane: if the currents getting in and out of the plane had been simulated, they would have polarized the correlation value and therefore the results.

CHAPTER IV.3

The simulation approach for the defect localization on a bi-dimensional device

---

IV.3.1 Introduction

The Failure Analysis performed for this sample was performed with the help of the Simulation Approach in two dimensions. The failing device was an ST Microelectronics IC which presented a very low resistance (approximately 10 Ohms) between Vdd and Ground. The I/V curve also showed a resistive behavior of the defect, as it was completely linear. The very small value of the resistance was probably denoting a short circuit between the two I/Os. When the component was received, other localization techniques (EMMI, Laser stimulation, OBIRCh) had already been used and were not able to give results which could localize the defect. These techniques cannot be used on packaged components, unlike Magnetic Microscopy which can see through non-magnetic materials. Therefore the IC had already been de-packaged, and it was possible to acquire information by optical and X-Ray inspection.

IV.3.2 Optical and X-Ray Inspection

The pictures taken of the component package showed no sign of defect, as it can be seen in figure IV.3.1. From this image, there is no evidence of any damage to the component. A further X-Ray inspection is then shown in figure IV.3.2.

These pictures show that no external damage is visible. To obtain a visual inspection of the die, then, the component was de-packaged and the molding compound was removed. The die was then attached on a flexible PCB, as shown in figure IV.3.3

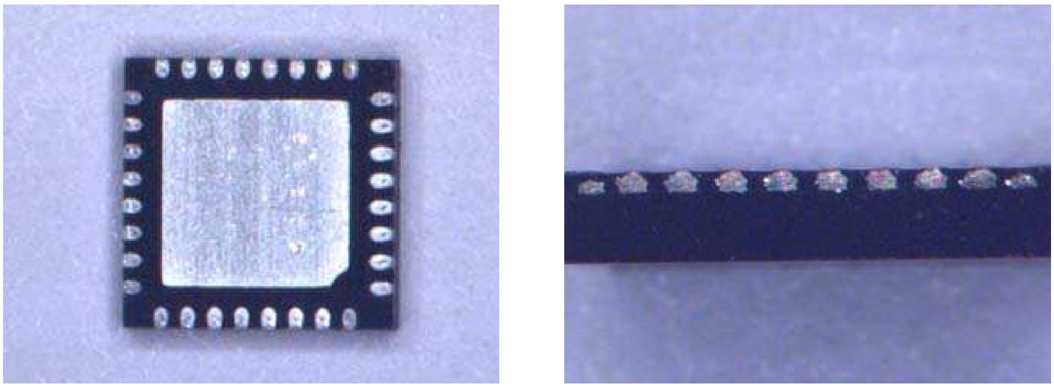

Figure IV.3.1: Optical inspection of the failed device

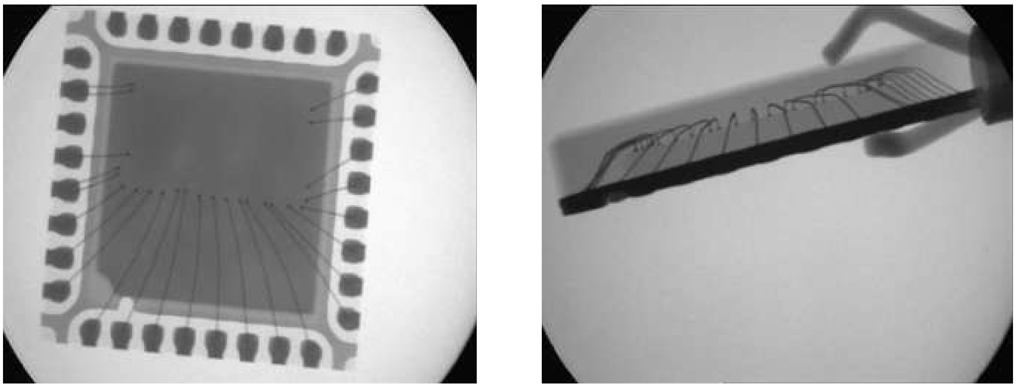

Figure IV.3.2: X-Ray images of the failed device

A close optical inspection, which is shown in the two images of figure IV.3.4, shows that there is no visible damage on the bonding wires or on the die itself which could localize and explain the failure.

From the optical acquisitions, it was possible to verify that the ST Integrated Circuit presented two metal tracks running in two loops around the component. Part of these loops are shown in figure IV.3.5: they are the Vdd and GND loops, which carry the power to the whole component.

IV.3.3 Magnetic Scan

The magnetic scan shows that some currents are flowing inside the device, as the shape of the field is such that already some currents can be hypothesized to be flowing between the two bonding wires. In figure IV.3.6 the magnetic scan of the defective device is shown. Starting from the knowledge of the magnetic field, the MCI algorithm was applied in order to obtain a first visualization of the currents layout; the

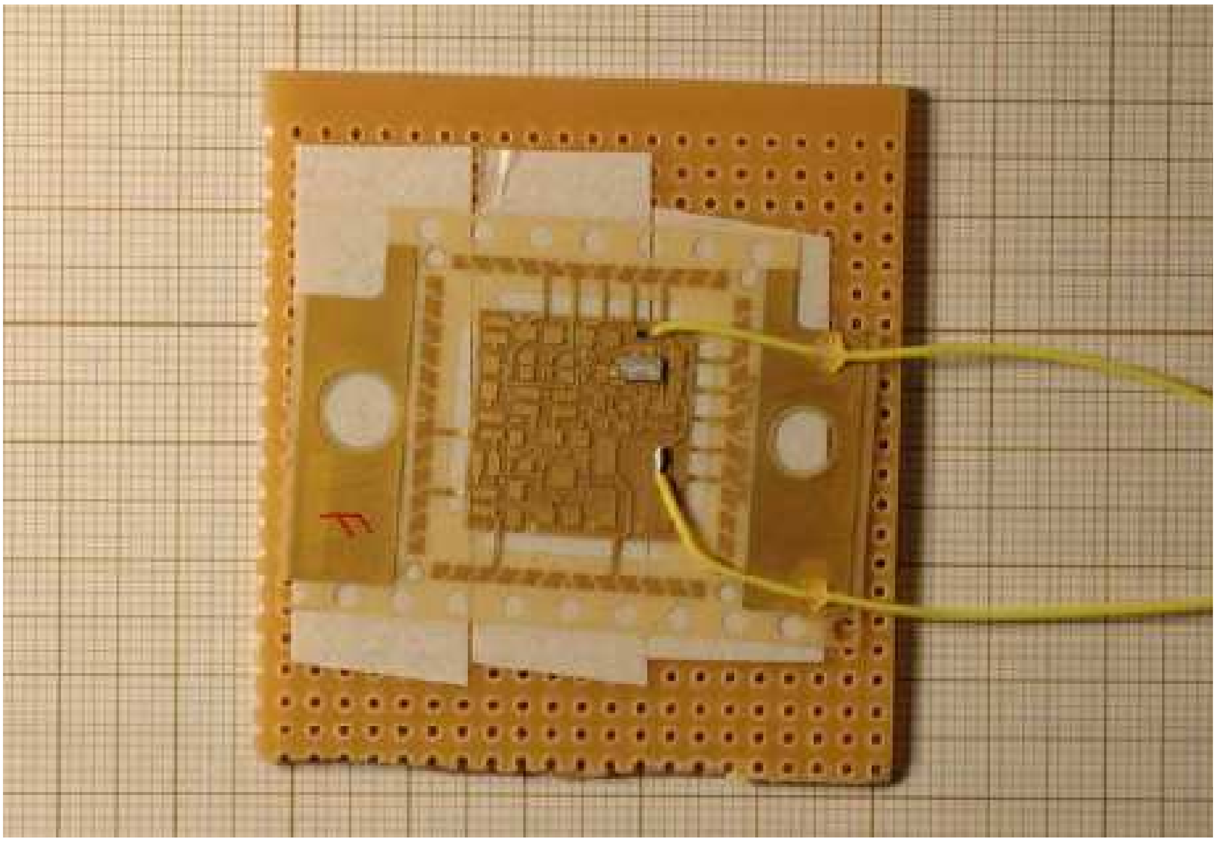

Figure IV.3.3: Depackaged component

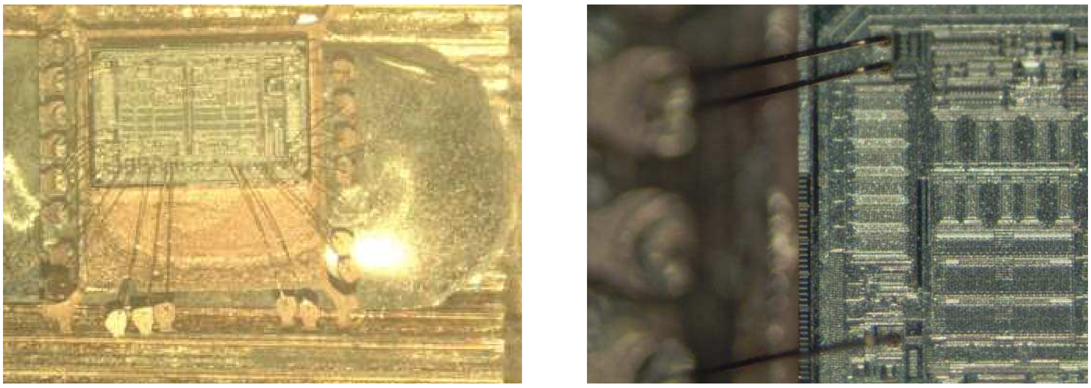

Figure IV.3.4: Close up pictures of the failing die

superposition of an optical acquisition of the sample to the results of the MCI technique are shown in figure IV.3.7.

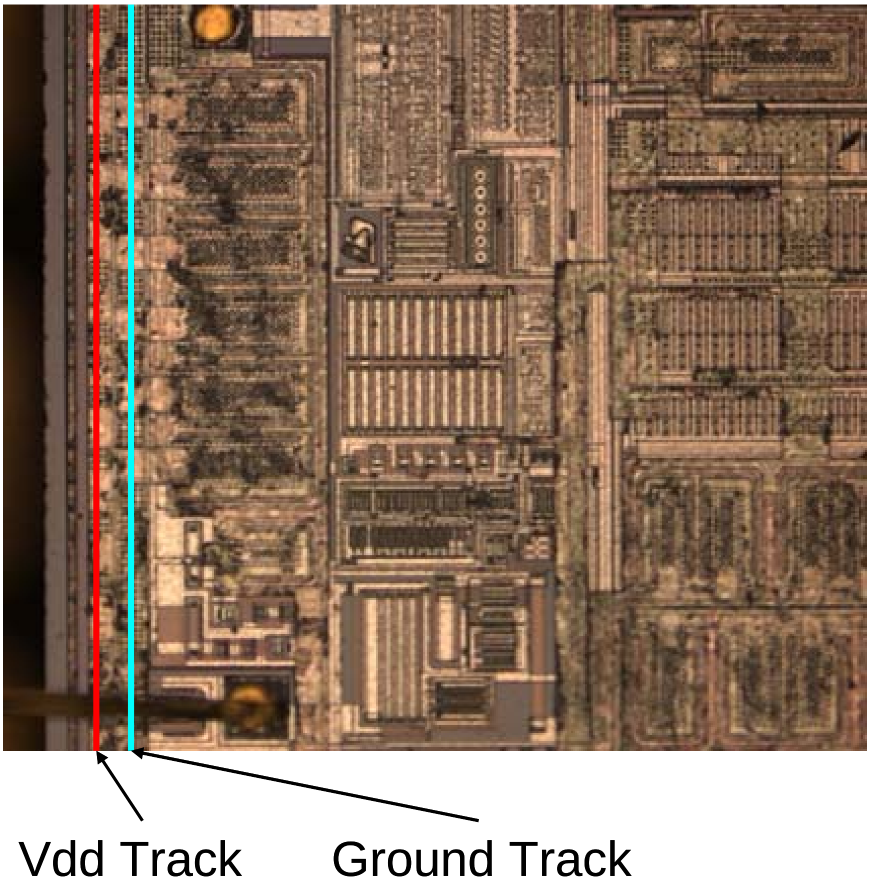

Figure IV.3.5: Detail of the Vdd and GND tracks running in a loop around the component

This image shows that it is impossible to localize the defect precisely from the simple MCI application, as the resolution is not good enough. However, from this first image it is possible to obtain an initial approximate idea of its position.

IV.3.4 Magnetic simulations

The next step was to come up with several defect hypotheses: each hypothesis represents a different possible current path. The pictures previously taken with an optical microscope produced the information about the two track loops around the component: these were schematized in order to simulate the possible currents flowing through them. As the short circuit was between the Vdd and the GND tracks, the defect needed to be at some point between the two loops.

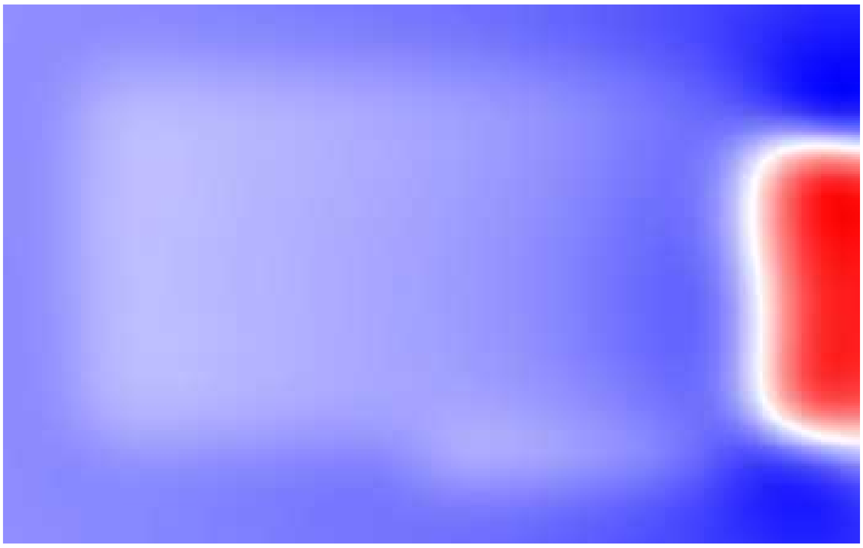

Figure IV.3.6: Magnetic image of the device

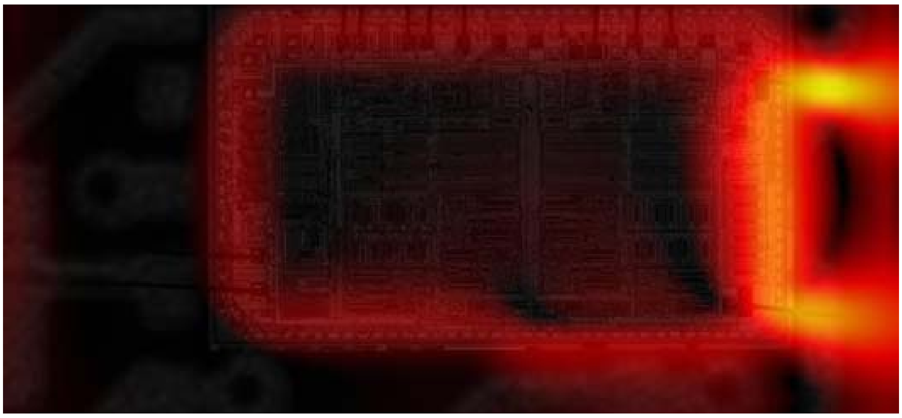

Figure IV.3.7: Magnetic Current Imaging results

IV.3.4.1 First defect hypothesis

The first hypothesis was to put a short circuit between the two tracks just next to the connection of the bonding wires. On the left side of figure IV.3.8 a schematical view of the layout of the two loops is shown: the small black line represents the short circuit which was simulated. The simulation of the magnetic field shown on the right side of the same image is quite different from the measurement of the magnetic field.

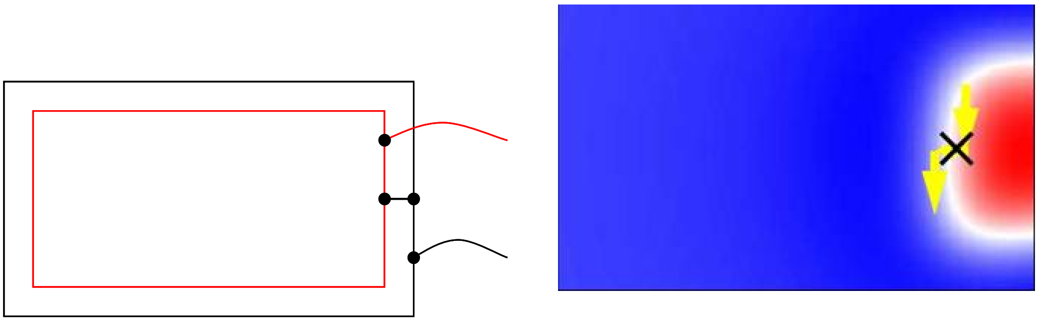

Figure IV.3.8: First defect hypothesis: current layout scheme (left) and simulation result (right)

IV.3.4.2 Second defect hypothesis

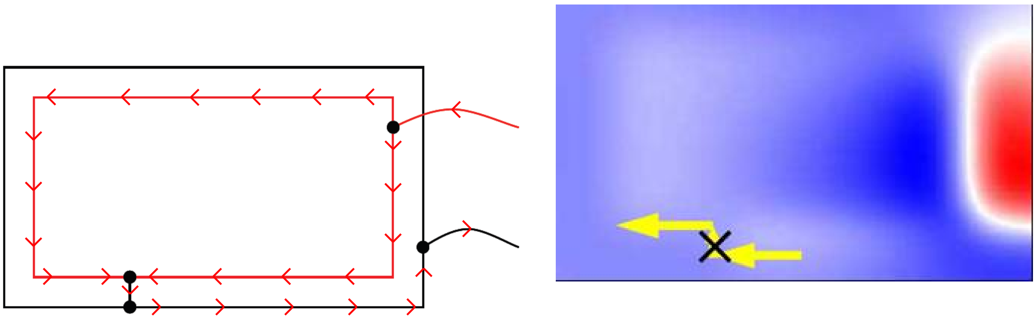

Figure IV.3.9: Second defect hypothesis: current layout scheme (left) and simulation result (right)

From both the magnetic image of figure IV.3.6 and the MCI result of figure IV.3.7 it is clear that there is a passage of current from the external ring to the internal one on the bottom side of the images; therefore the proposed simulations were performed on hypotheses which took into account short circuits on this part of the device. In figure IV.3.9 the second defect hypothesis is shown. In this case, there are two main current flows, running through the Vdd loop. The result of the simulation is shown in the image on the right.

IV.3.4.3 Third defect hypothesis

The third hypothesis shown here is still a short circuit between Vdd and GND on the bottom side of the images. However, the defect is placed in a different position with respect to the second hypothesis.

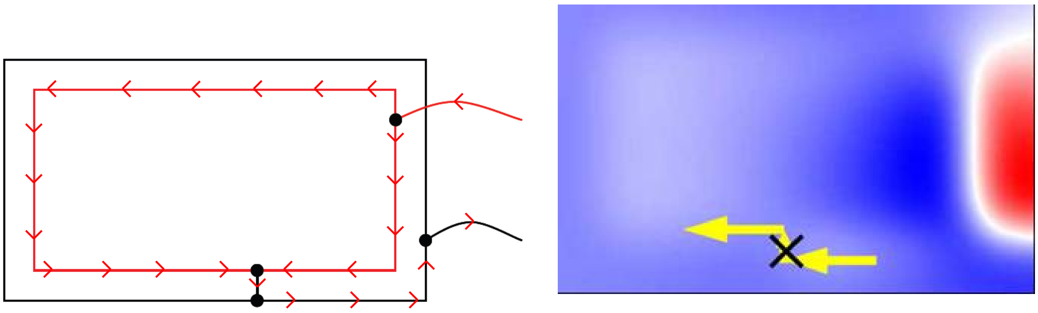

Figure IV.3.10: Third defect hypothesis: current layout scheme (left) and simulation result (right)

IV.3.4.4 First rough result

The three simulations shown above were then compared to the magnetic field acquired on the device as in figure IV.3.6. The simulation with the maximum correlation to the measurement is the second one; it was possible, just by comparing the two magnetic images, to see the affinity between them. The higher value of the correlation then gave the correct result in terms of position of the short circuit.

The Simulation Approach applied here was sufficient to identify the area of the circuit where the defect was situated. However its precise location had still not been found.

IV.3.4.5 Finer localization

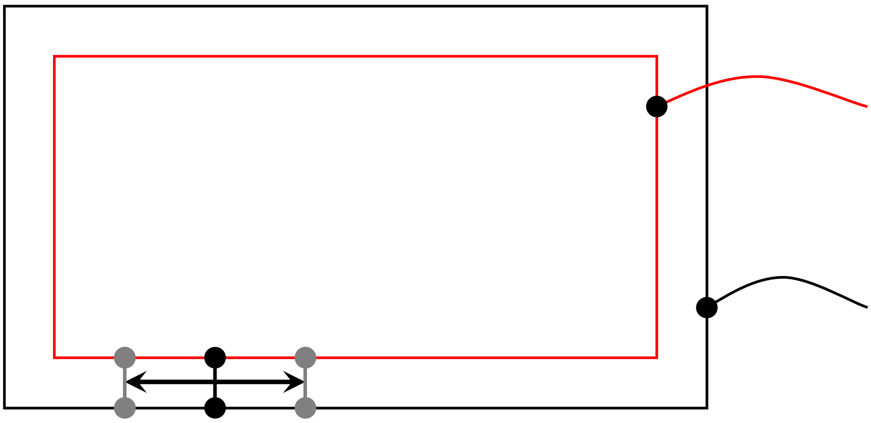

Figure IV.3.11: Short circuit line shift

To localize the defect precisely, a second set of simulations had to be performed. In this case a particular version of the line shift transformation explained in section III.3.1.1 was applied to the short circuit line. A schematical view of this shift is shown in figure IV.3.11. While shifting the small vertical line, all the currents flowing around it were changed. The step chosen for the shift was of $1\mu m$. The results of the correlation with the second set of simulations gave the precise location of the short circuit.

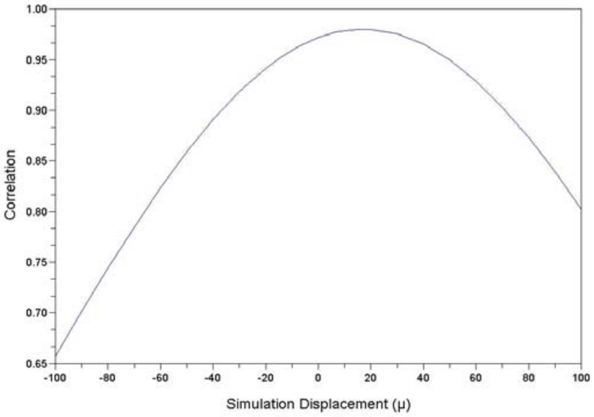

Figure IV.3.12: Correlation in function of the line shift

In figure IV.3.12 the variation of the correlation in function of the short circuit displacement is shown. This figure shows that a variation of the position of the simulated short circuit corresponds to a regular variation of the evaluated correlation. The maximum of the correlation corresponds to the exact spot where the short circuit was found.

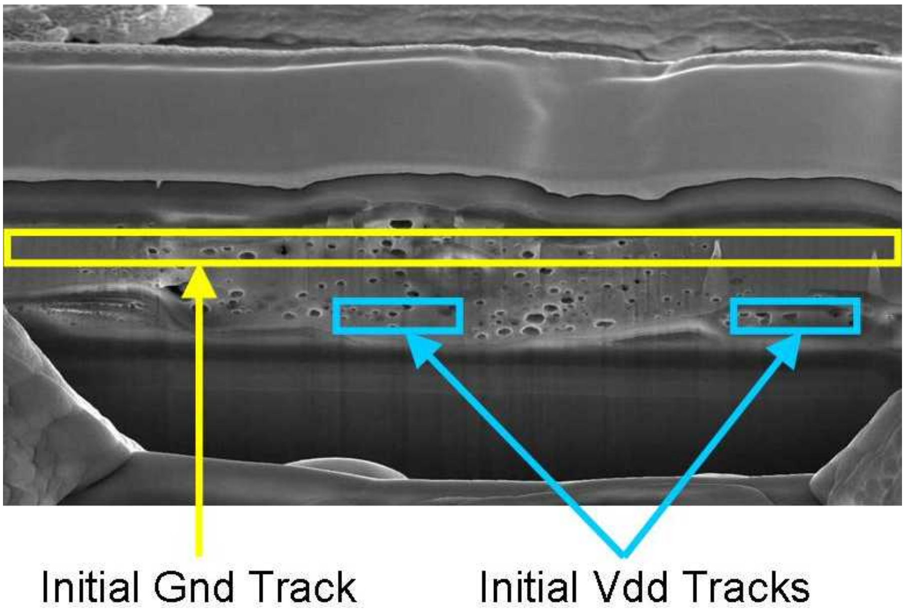

Figure IV.3.13: Device FIB cross-section

IV.3.5 Results

The results of the analysis on the ST device allowed the validation of the new methodology. In the end the short circuit was found between the positive and the ground tracks; after cross-sectioning the circuit, the defect was validated by Scanning Electronic Microscopy inspection, as shown in figure IV.3.13. The results of the cross-sectioning show that the metal track (the one in the middle) had completely melted, making a net contact with two different lines (located on the left and on the right at the bottom of the picture).

CHAPTER IV.4

Three-dimensional Test Vehicle: reconstruction of a 3D current path

In order to validate the Magnetic Microscopy technique with the help of simulations for three-dimensional components, a test vehicle was built. In this way it was possible to show the benefits of the Simulation Approach for three-dimensional currents shown in chapter III.4.

IV.4.1 Test Vehicle conception

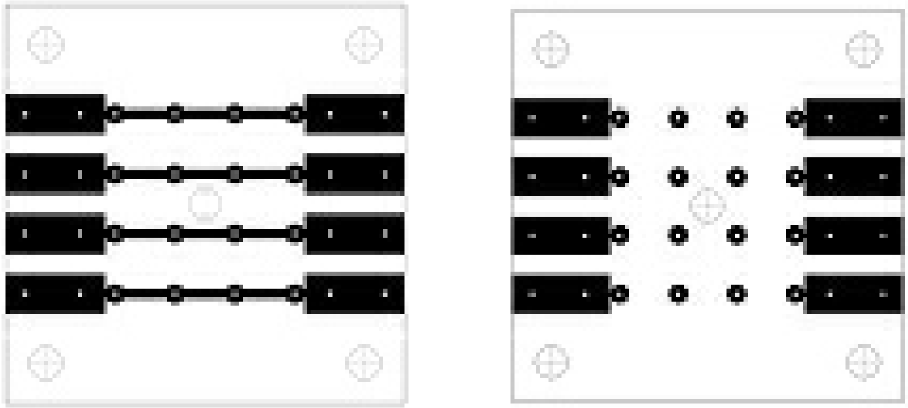

Figure IV.4.1: Layout of a layer of the test vehicle

The test vehicle consisted of a stack of Printed Circuit Boards (PCBs), with several tracks representing the interconnections between the different modules of a system. The vehicle was built to represent the geometry of the interconnections on a 3D component, such as a System in Package, as closely as possible. In figure IV.4.1 it is shown how each layer of the stack of PCBs is composed. There are several possible current lines on each layer, and the layers are linked to each other by small metallic wires. The composition of the different layers is then shown in figure IV.4.2.

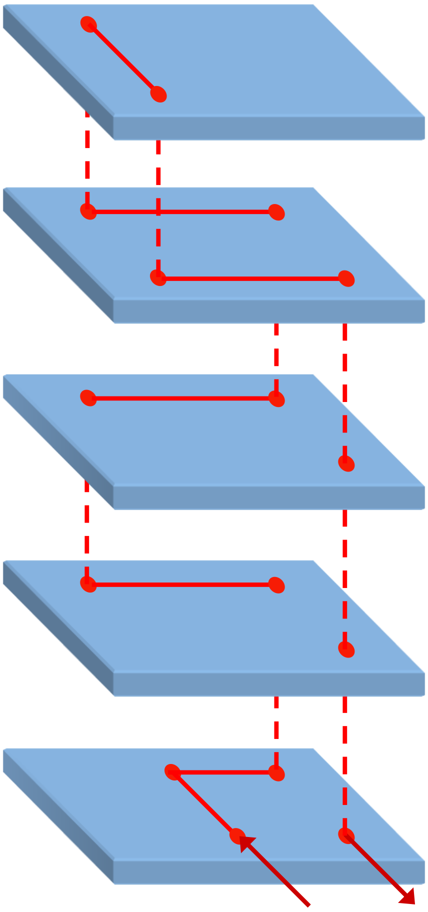

Figure IV.4.2: Schematic view of the Test Vehicle

In figure IV.4.3 the final assembled test vehicle is compared with a real case device from the French manufacturer 3D-Plus with approximately the same dimensions. In order to obtain the map of the currents, the steps described in chapter III.4 were followed.

IV.4.1.1 Electrical setup

The test vehicle was built to emulate a generic System in Package presenting a short circuit between power and ground. It therefore contained a three-dimensional conducting path with a total resistance of approximately 10Ω running inside the structure. The current injected into the sample was the result of a trade off between the maximum power permitted in a typical defective device and the need to have a magnetic signal, which is strong enough at long working distances, given that the magnetic induction

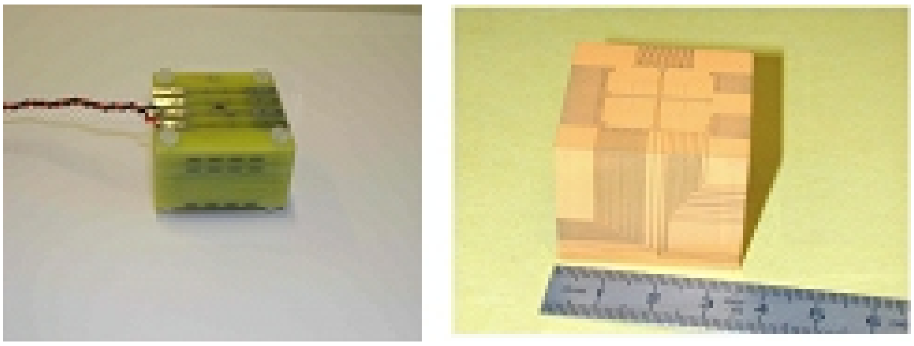

Figure IV.4.3: The test vehicle (left) and a real case SiP (right)

field is inversely proportional to the square value of the distance. Therefore it was decided to apply a current of $3mA$. The total power dissipated was:

$$P = RI^2 = 10\Omega(3 \cdot 10^{-3}A)^2 = 10 \cdot 9 \cdot 10^{-6}W \approx 0.1mW \qquad \text{(IV.4.1)}$$

IV.4.2 Magnetic acquisitions

As the information needed about the topology of the metal lines was already known, X-Ray images were not acquired. Therefore the first acquisition to be performed was a magnetic scan.

IV.4.2.1 Flat scan

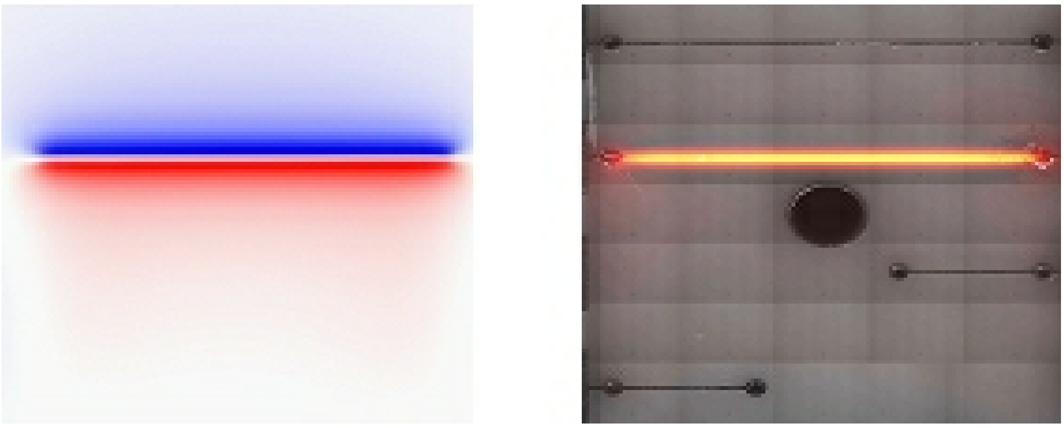

Figure IV.4.4: Magnetic scan (left) and MCI image (right) of the test vehicle

This is shown in fig.IV.4.4, together with the results of the MCI analysis. Thanks to the application of the MCI algorithm, it was possible to obtain the location of the current flowing in the line closest to the probe. It was not possible to focus on currents flowing in other layers of the sample using MCI, as they were both too far from the probe and hidden by the top current.

By proceeding with the basic simulation approach alone, it would have been possible to localize some of the other currents which were buried inside the sample. However, some of the currents were flowing on the z axis and therefore did not produce any magnetic field in the z direction, and some currents would have been hidden by those flowing above them. The only solution which could map all the currents flowing inside the device was to proceed to tilt the sample.

IV.4.2.2 Sample tilt

The flat and titled scans produce different information about the currents flowing inside the vehicle. While the flat scan gives the precise position of the currents flowing on the top layer, the tilted scans can give additional information about the deep buried currents. The schemes of the flat and tilted scans, together with the photographs taken during the scans, are shown in figure IV.4.5. These images show how it is possible to map currents even when their projections are superposed on the $x - y$ plane. The projection of the currents on a plane parallel to the surface of the sample is not enough to distinguish the different lines. However, when the sample is tilted, the currents projected on the measurement plane are not superposed.

From a physical point of view, the projections of the currents on this new scanning plane represent the information given by the other components of the Magnetic Induction Field which were missing from the first scan. By using the standard MCI technique it would not have been possible to map any of the currents inside the sample, as all of them would have been too far from the probe. The Magnetic acquisition for the tilted sample, together with the superposition of the MCI image to the optical acquisition are shown in figure IV.4.6.

IV.4.3 Magnetic simulations

Due to the information given by the MCI and the information about the internal structure of the sample, only a limited set of simulations was necessary. The position of each simulated current inside the sample was varied, layer by layer, in order to understand the relation between the distance from the currents to the SQUID and the space resolution obtainable.

Therefore, for each current path (or set of paths) of the sample a number of simulations was performed, each representing the different possible positions of each line, until the relative maximum of the correlation was obtained.

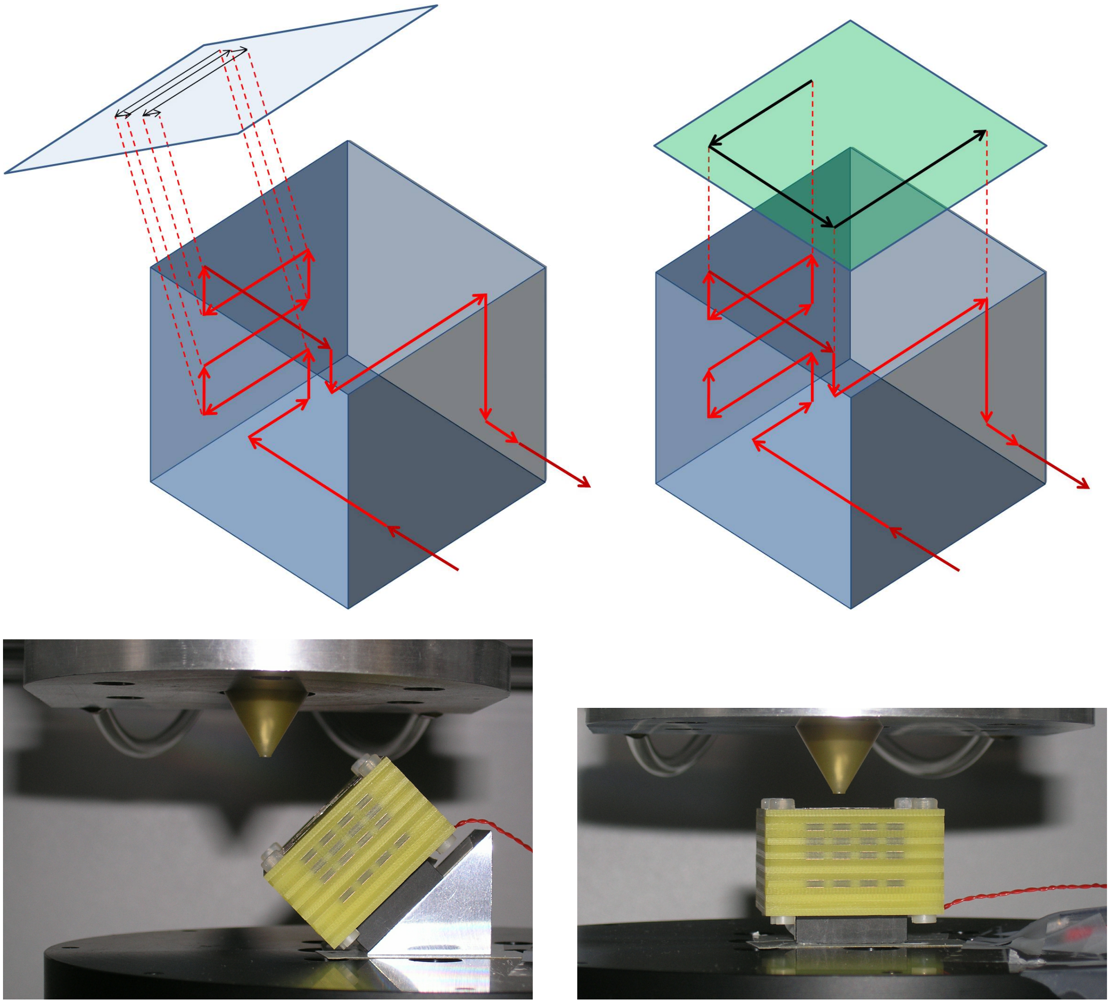

Figure IV.4.5: Sample measurements, tilted (left) and flat (right)

IV.4.4 Results

With this procedure it was possible to localize with precision the entire current path with a resolution sufficient to localize all the electrical defects at assembly level. Even though the high working distance problem was solved by using the simulation approach, by tilting the sample it was possible to increase the spatial resolution and to visualize those currents flowing underneath other currents. It was also possible to map currents flowing along the z axis, which do not make any contribution to the z component of the magnetic induction field, as this is generated in accordance with the Biot-Savart law of equation II.1.25.

The resolution obtained was highly dependent on the working distance, as could easily have been predicted. For the top layer, the resolution was of approximately $5\mu m$. It then decreased linearly with

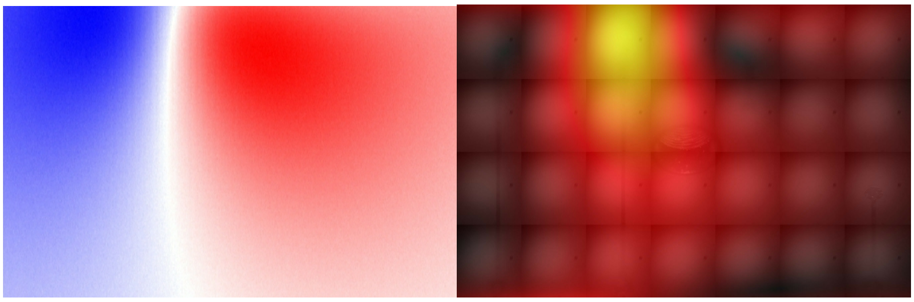

Figure IV.4.6: Tilted Magnetic scan (left) and superposition of the MCI to the optical acquisition (right)

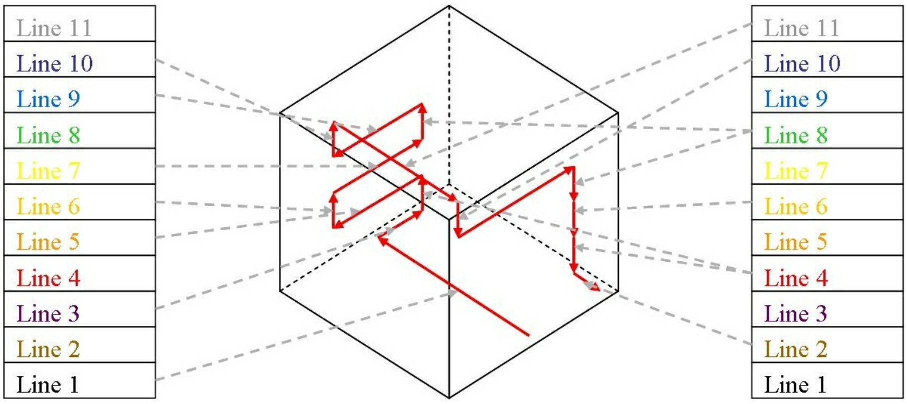

Figure IV.4.7: Simulated currents

the working distance. For currents more than $2cm$ from the probe it was then impossible to discern the magnetic signal from the noise, so all the simulations gave almost the same correlation.

In figure IV.4.7 all the lines which were simulated are shown. For each of them, a few positioning hypotheses were simulated and compared with the measurements. In the graph in figure IV.4.8 the results of the correlations are shown. The study started with the simulation of the currents placed furthest away from the SQUID. By shifting the simulated lines, it was possible to find the relative maximum of the correlation for each current. The study passed then to a new current line and the same process was repeated. In figure IV.4.8 it can be seen that there are small jumps in the correlation which correspond with the simulation of a new line closer to the SQUID. The correlations shown are the results of the average of the correlations obtained from both the flat and the tilted scan.

Finally, the highest correlation found was very next to 1, which is the maximum obtainable. This correlation value was obtained when all the simulated currents were positioned in the right places on the model, where the real current was actually flowing.

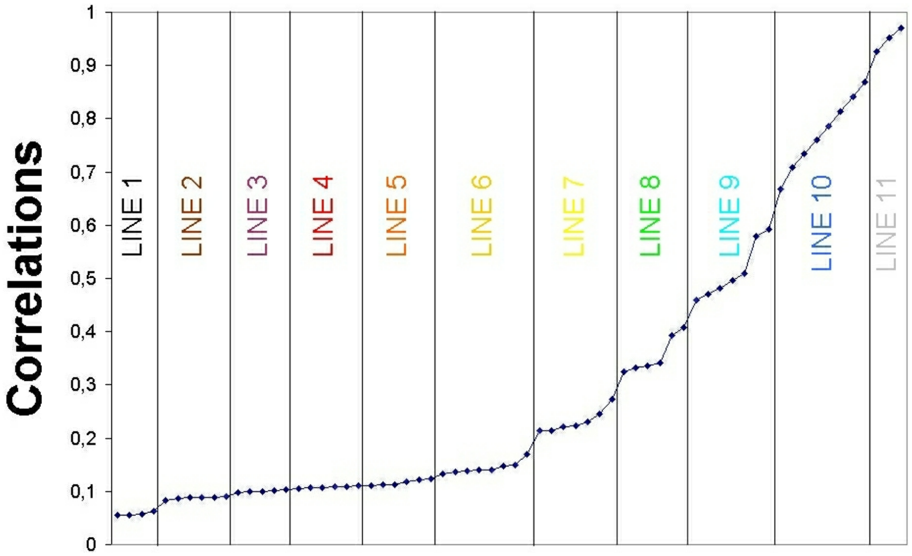

Figure IV.4.8: Correlation function depending on the displacements of the simulated currents

CHAPTER IV.5

Three-dimensional failure localization on a cube assembly: a deep buried short circuit

The use of the MCI technique for three-dimensional System in Package devices has been previously documented [70]. However, in that particular case studied all the currents were flowing on the external part of the package. Therefore it was possible to perform the measurements at a short distance from the currents. A case where the simple application of the MCI algorithm was not able to give the desired results will be presented here. This was because some of the currents were flowing as far as one centimeter away from the package's external surface. Consequently the MCI technique was not able to generate a full map of the currents.

In such cases it is possible to find the current leak by using the Simulation Approach. By applying this technique, it is therefore possible to reconstruct the current path with enough precision to isolate the defect. To measure the precise value of the working distance, the fitting algorithm, applied using the knowledge of the shape of the magnetic acquisition curve, was used, as has been explained in chapter III.3.1.5. This new methodology was employed to find those parameters which previously could not be found with sufficient accuracy.

IV.5.1 The failed device

The failed component studied was a memory stack from 3D-Plus. A certain percentage of the manufactured components all presented the same type of defect: abnormal behavior observed during electrical tests. Furthermore, only one failed device was provided for examination.

IV.5.1.1 Sample Background

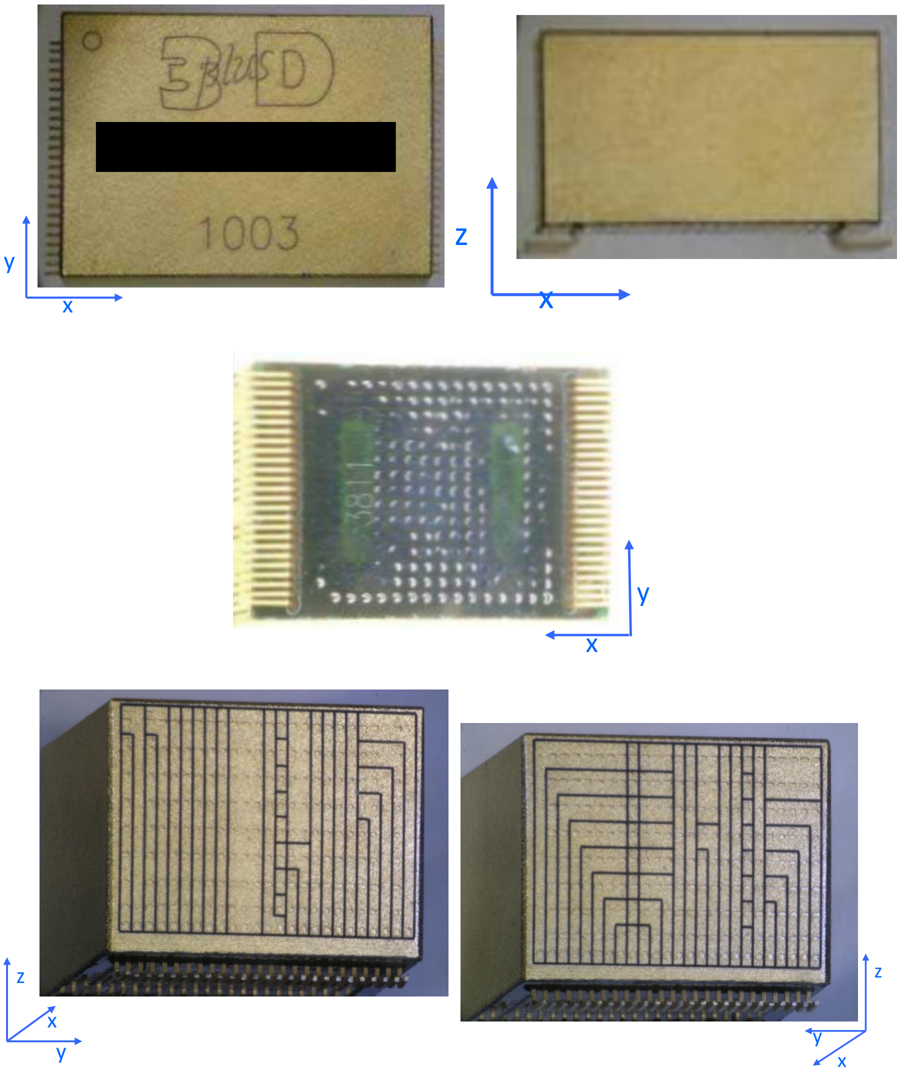

Figure IV.5.1: Optical views of the DUT: the top of the component (top left), the bottom (top right), one of the plain sides (middle) and the two sides with the vertical connections between different layers (bottom). The coordinates indicate orientation of the device.

Figure IV.5.1 shows optical images of the DUT. It is an eight layer flash memory stack. Each layer is composed of a strap board which connects the two sides of the component which have the vertical connections, and a flexible PCB connected via bond wires to the memory chips.

IV.5.1.2 Faulty behaviour

During the electrical characterization of the module performed with ATE (Automatic Test Equipment), an abnormal current value was detected on the Write Enable pin of the 8th level (WE7). The test showed a current of $65mA$ on this pin, which was only limited by the compliance of the equipment. However, despite this faulty behavior, the device was fully functional.

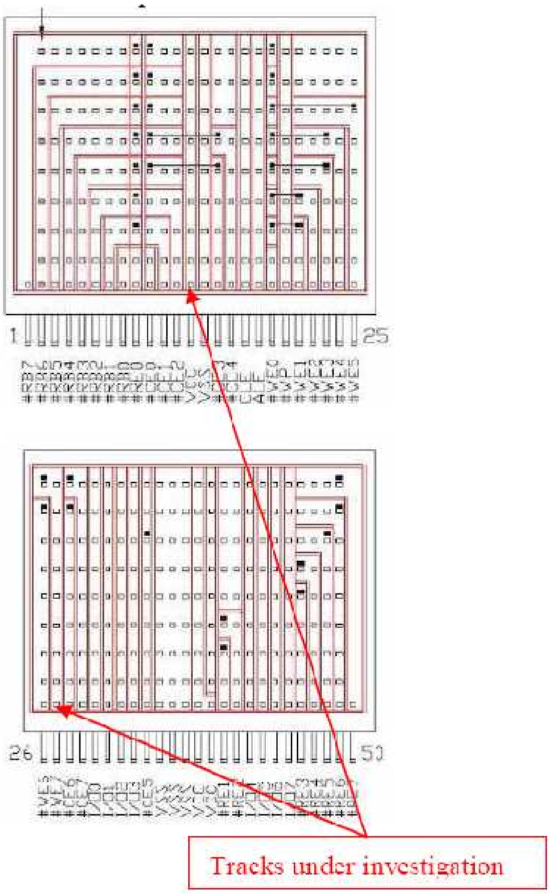

Figure IV.5.2: Layout of the lateral connections of the sample: all the layers are connected to the external pins by the lateral metallic tracks. The tracks under investigation are those which relate to the WE07 and VCC pins.

As only the 8th level of the component presented an anomaly, comparative tests between the 7th (the reference device) and 8th (the faulty device) levels were performed. It was then verified that all the other levels (from the 1st to the 6th) behaved exactly as the 7th. The tracks under investigation can be seen in the pin-out image in figure IV.5.2. Here can be seen the complete layout of the external connections which are used to link the different layers of the circuit electrically.

IV.5.1.3 Electrical tests

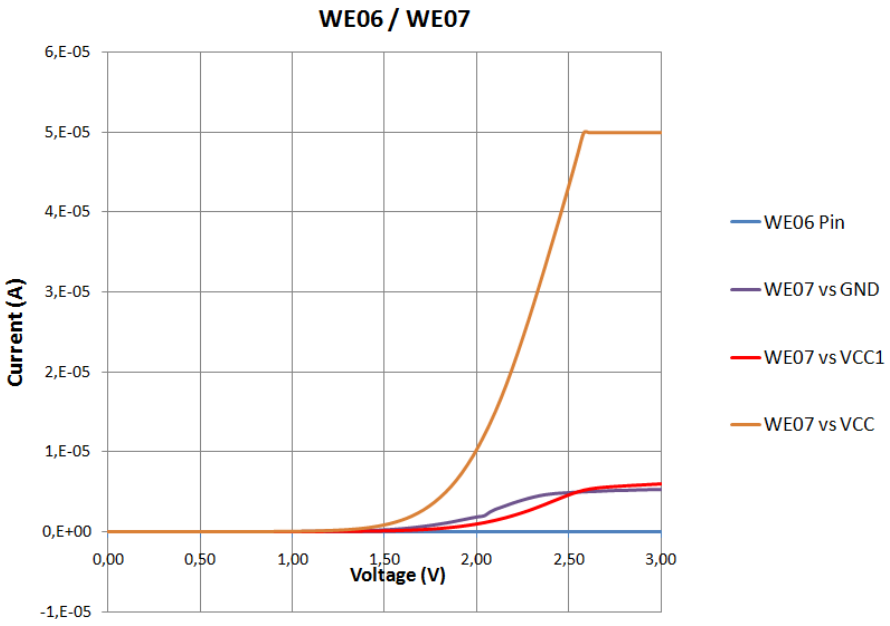

Figure IV.5.3: Differences in the electrical signatures between WE06 and WE07 pins versus GND, VCC1 and VCC. WE06 vs GND, WE06 vs VCC1 and WE06 vs VCC produced the same results and are therefore all represented by the same line on the graph.

Electrical tests performed on the sample showed a current leak on the Write Enable pin of the 8th level (WE07). The electrical signature of the defective pin was acquired and compared with that of the 7th layer pin (WE6). The module presented two VCC pins which were not connected internally (VCC and VCC1). Therefore an acquisition of the current/voltage characteristic between the WE pins and, respectively, the ground (GND), VCC and VCC1 was performed. The results are shown in figure IV.5.3. It is clear from this picture that, as expected, there is no current flowing between the WE06 and the VCC, VCC1 or GND pins.

The two curves relating to WE07 versus GND and VCC1 are very similar. In both cases, a small amount of current (approximately $5\mu A$) starts to flow if a high enough bias is applied. Finally, there is a very high current leak flowing between the WE7 and VCC pins. The compliance used for this measurement was $50\mu A$, and it saturated before it could reach the 3V measurement limit. The current flowing between the WE7 and VCC pins is a lot higher than the current on the reference device. This signature does not show a direct short circuit, but a current leakage at some point in the device. The fact that the signature of the failure showed on the WE07 pin, could easily have led to the conclusion that the defect was on the top layer of the sample. It was later proved, by using magnetic techniques, that the defect was in fact very deep inside the device and not on this layer.

IV.5.1.4 Optical and X-Ray inspection

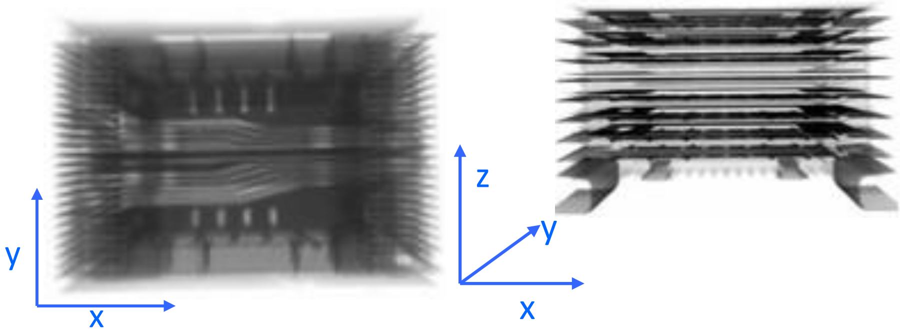

Figure IV.5.4: X-Ray acquisitions of the sample: top view (left)and side view (right).

The external optical inspection of the sample showed no sign of defects. An X-Ray inspection of the sample was therefore carried out. In figure IV.5.4 the X-Ray acquisitions of the sample are shown. Due to the complex nature of the assembly, it is not possible to see any defects in these images. In the side view it is possible to see how complex the assembly of the device is: there are eight separated layers composed of a lead frame, a strap board and the die. By acquiring an X-Ray image from above the DUT it is therefore not possible to focus on a particular layer or to obtain sufficient information about the internal layout. At this point in the analysis, it was still most probable that the defect was situated on the 8th layer. An attempt was made to focus the X-Ray image on this layer with no results.

IV.5.2 Magnetic Microscopy analysis

The best way to localize a defect without risk of destroying it is to use a non-invasive contactless technique, such as Magnetic Microscopy. An electrical setup which permitted the use of this technique was therefore put in place.

IV.5.2.1 Electrical setup

To avoid applying too high a voltage on the pins, the maximum current allowed on the WE07 pin was around $100\mu A$. In order to get the best signal to noise ratio, magnetic acquisitions are usually performed through an AC bias. The acquisitions are then filtered through a lock-in amplifier working at the same frequency of the injected AC current. This makes it possible to filter out all the background magnetic noise, which is mostly due to the DC fields generated by ferromagnetic materials and the $50Hz$ field generated by the system currents. The DC bias was then set to 2.5V to activate the defect and then added a $1Vpp$ AC voltage. The resulting current, Ipp was approximately $100\mu A$. For currents of this amplitude, the MCI technique is the best solution for working distances of up to a few hundred micrometers, which was the distance we had estimated from the top of the package to the 8th layer.

IV.5.2.2 Magnetic analysis

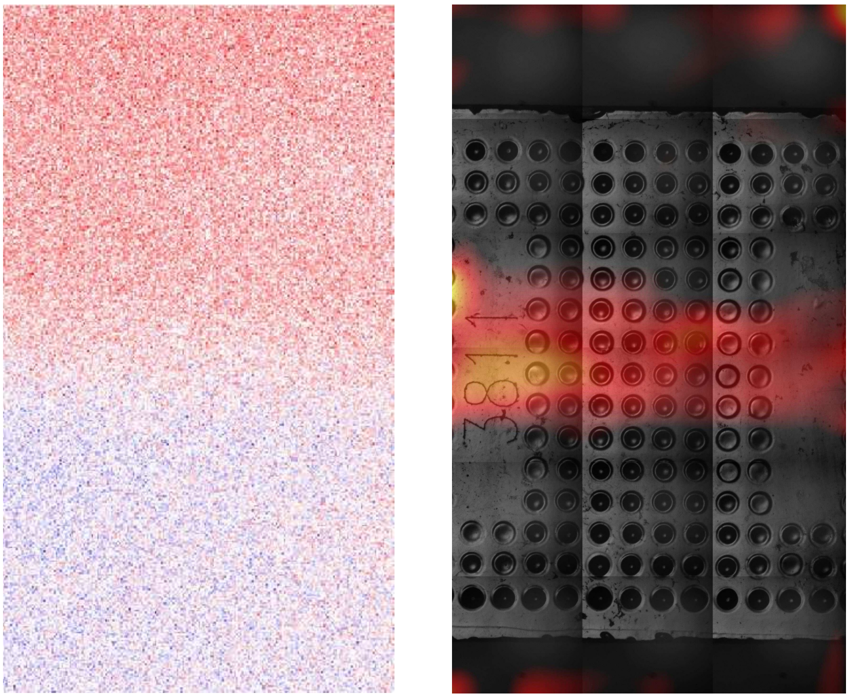

Figure IV.5.5: Magnetic acquisition (left) and overlay of the results of the MCI calculations with the optical acquisition (right).

A first scan showed no signal at all above the DUT. This was the first sign that the over-current was not flowing in the 8th layer. The lack of signal was also due to the package metalization, as part of this metal layer can become partially magnetized and prevent the magnetic acquisition from giving meaningful results in terms of MCI analysis. An attempt was therefore made to acquire the magnetic signal from backside, which was not covered in metal. The result was a very noisy acquisition, but one which still provided some information that could be analyzed. An MCI calculation performed on this acquisition gave an initial idea of the current distribution. The results can be seen in figure IV.5.5. It is clear that the output current map is not very precise.

IV.5.2.3 First Simulation

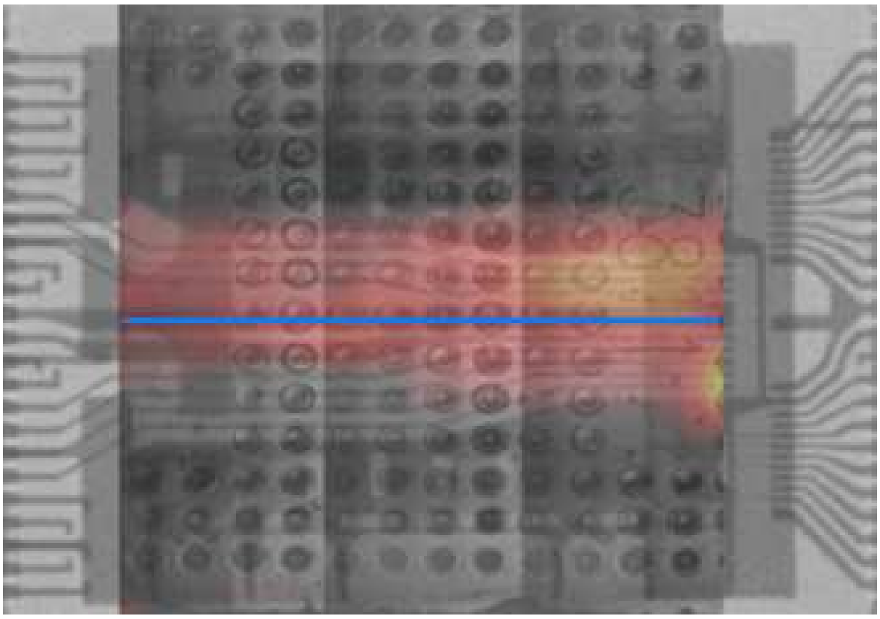

Figure IV.5.6: Superposition of the MCI results, the current localization by simulation and the X-Ray image.

To localize the current on the $x - y$ plane with greater precision a magnetic simulation of a current line was performed. Starting from the hypothesis that there was a current line on one of the layers, a set of simulations was generated by shifting the current direction and position. The results are shown in figure IV.5.6. The thin blue line represents the position of the simulated line which had the highest correlation to the measurement. This result was then superposed to an X-Ray image in order to obtain information about the current's position in the circuit layout.

IV.5.2.4 Tilted acquisitions

As this step was not conclusive, it was decided to perform magnetic acquisitions followed by MCI analyses on the sides of the sample, where all the connections between the pins of the device and the different layers of the stack are located. The MCI results are shown in figure IV.5.7. These results showed that the current was not flowing on the top layer, but that it was buried deep inside the package. Surprisingly, the vertical currents stopped at the 5th level on both sides. This is the reason why the acquisition taken above the sample did not give any results: the current was flowing too far from the surface.

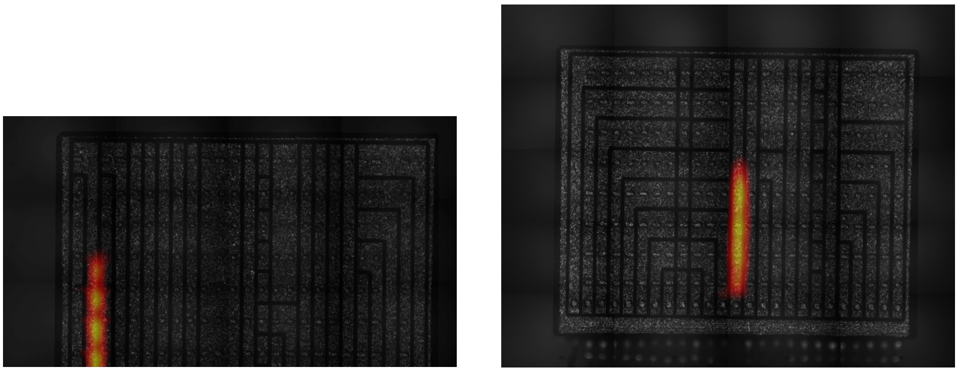

Figure IV.5.7: MCI results for the sides of the sample

IV.5.2.5 Partial sample de-processing

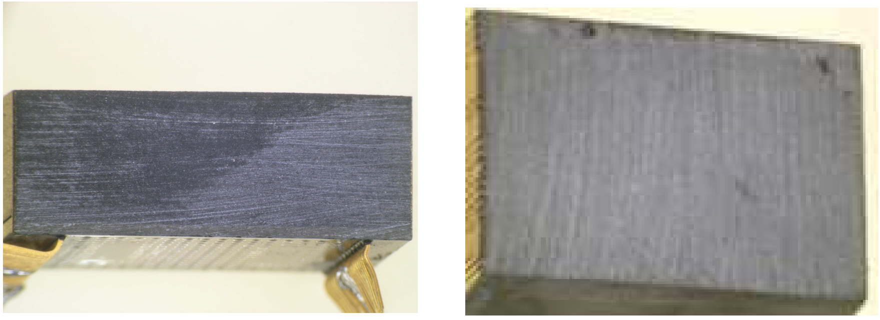

Figure IV.5.8: Side view (left) and top view (right) of the de-processed sample

Thanks to this last step, it was finally possible to verify that the defect was on the 5th layer. To obtain more detailed results it was necessary to decrease the working distance. A physical de-processing of the package was performed by cutting the device just above the fifth layer. The results of the cross section are shown in figure IV.5.8. The electrical tests performed earlier were then re-performed to be sure that the defect had not been destroyed.

IV.5.2.6 Further MCI analysis

After this step, the bi-dimensional layout of the current was obtained by performing a magnetic scan followed by an MCI analysis. The resulting current layout is shown in figure IV.5.9. In this image it can be clearly seen that there is a current flowing in the middle of the sample. However, the exact z plane where the current is flowing is still unknown. Therefore a further magnetic simulation was performed.


[redacted]

Figure IV.5.9: MCI results on the top side

IV.5.2.7 Evaluation of the z plane by the Simulation Approach

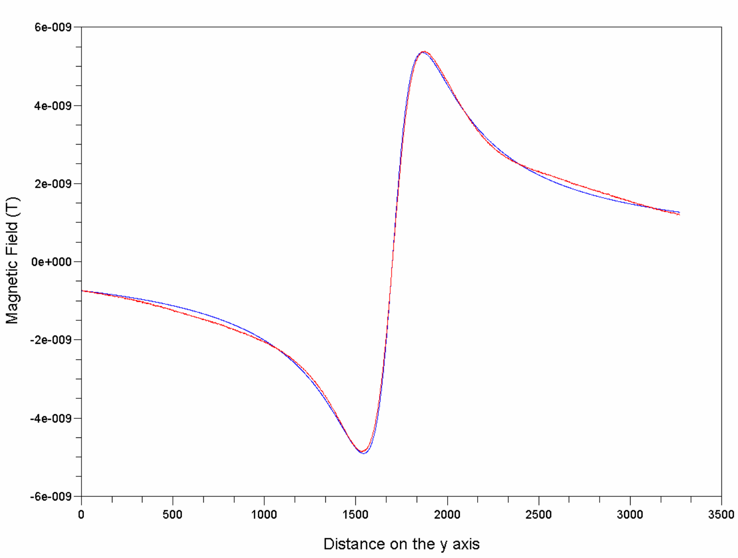

Figure IV.5.10: Fitting of the magnetic field

To evaluate the z plane on which the current was flowing with precision, a magnetic curve fitting was generated as in section III.3.1.5. The results of this analysis are shown in figure IV.5.10. The red curve is the acquisition of the magnetic field on the y axis, while the blue curve is the best fit. The two curves are very similar, showing that the output parameters of the fitting are extremely precise.

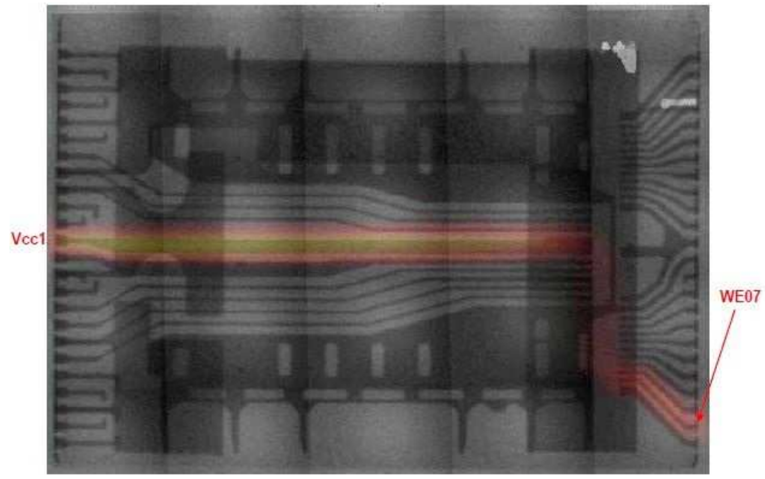

Figure IV.5.11: Superposition of the MCI results to the X-Ray acquisition of the 5th layer

The fitting gave a z distance of $834\mu m$ from the probe. As the package was now already partially de-processed, it was possible to acquire an X-Ray image of only the 5th layer. By superposition of this image to the simulation it was then possible to localize with precision the exact z plane inside the layer on which the current was flowing. Once the vertical localization of the current was found, it was possible to superpose the X-Ray acquisition of that layer to the current layout, as shown in figure IV.5.11. This figure shows the exact track where the current was flowing.

IV.5.3 Defect Localization results

On the fifth level of the sample, the WE7 pin should not be connected to the flex board. However, it can be seen in figure IV.5.11 that there is an electrical connection on that pin. In order to validate the results, a comparison study between the 8th and 5th levels of the sample was performed.

In figure IV.5.12 the electrical contacts of the 8th layer are shown and enlarged. The two tracks which are highlighted in the image are clearly open, so there is no contact with the external tracks which connect the vertical layers to the pins of the component. These two lines need to be left open and not connected to the external vertical tracks; as the dies are reported on these lines through bond wires, the tracks were cut at this level. This same cut was performed on all the other layers in order to leave these pins unconnected for all the dies.

In figure IV.5.13, the X-ray images of the 5th layer are shown. It has to be noted that one of the two pins still makes a short circuit with the external connections. This defect was due to a misalignment of the layers. While the 8th layer board had been correctly placed, the 5thh layer board had been slightly shifted to the right. An enlarged view of the left-hand side of the two layers is shown in figure IV.5.14.

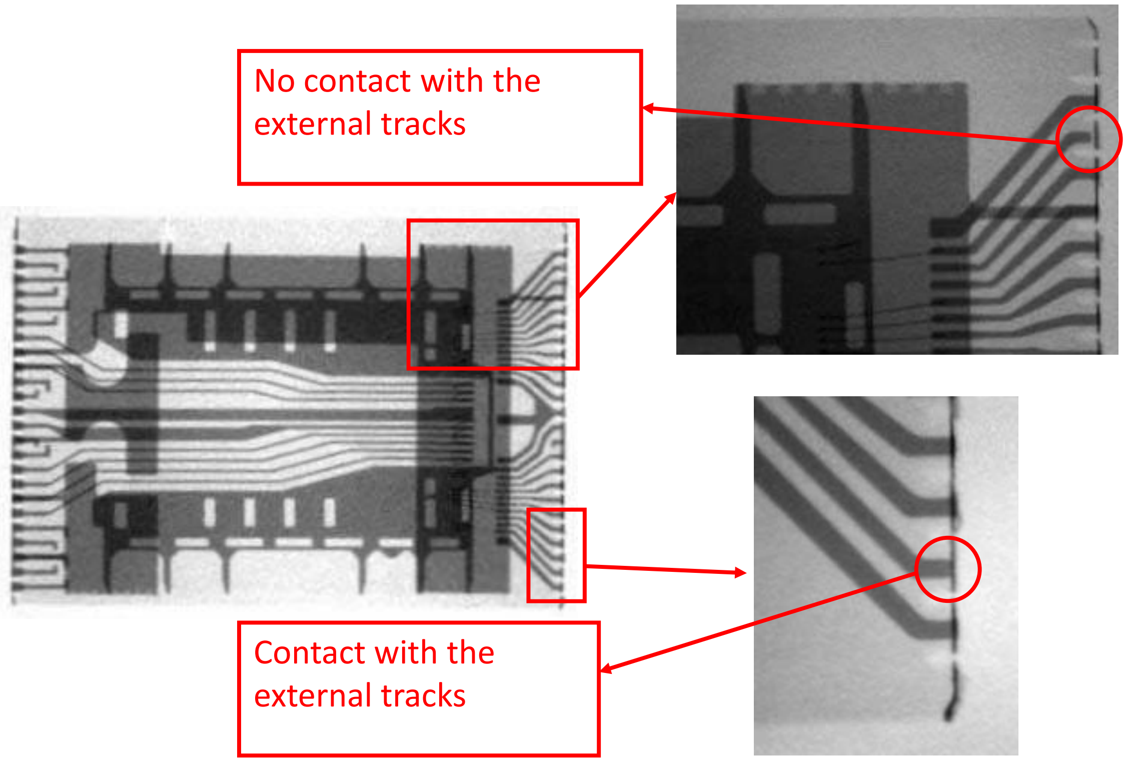

Figure IV.5.12: Electrical contacts on the 8th layer

Here it can be seen that, due to a misalignment of the component during production, there was still a part of the external lead frame remaining on the 5th layer. Not all the layers of the component had been placed and cut in the same way. On the left-hand side parts of the lead frame which should have been cut out were still present, as the 5th layer was shifted to the right. This is shown in figure IV.5.14. Meanwhile, on the right-hand side of the layer the cut was performed further over to the left than it should have been. Therefore parts of the lead frame which should not have been removed were cut out. In this case, the track which should have been left open was short-circuited to the external vertical lines.

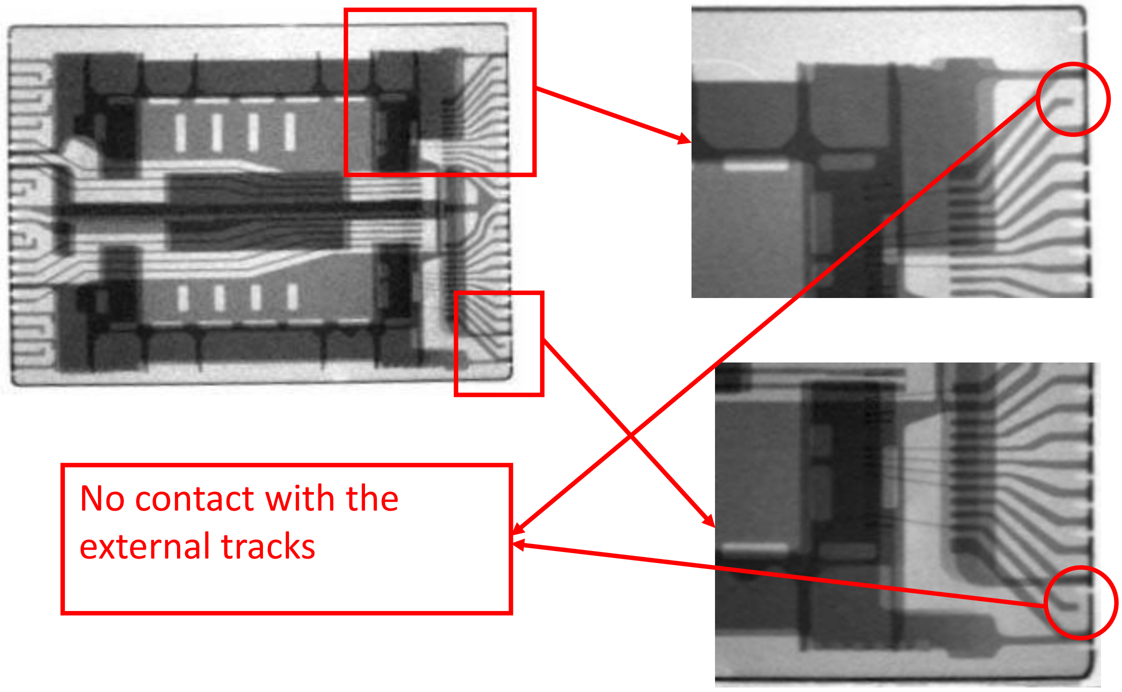

Figure IV.5.13: Electrical contacts on the 5th layer

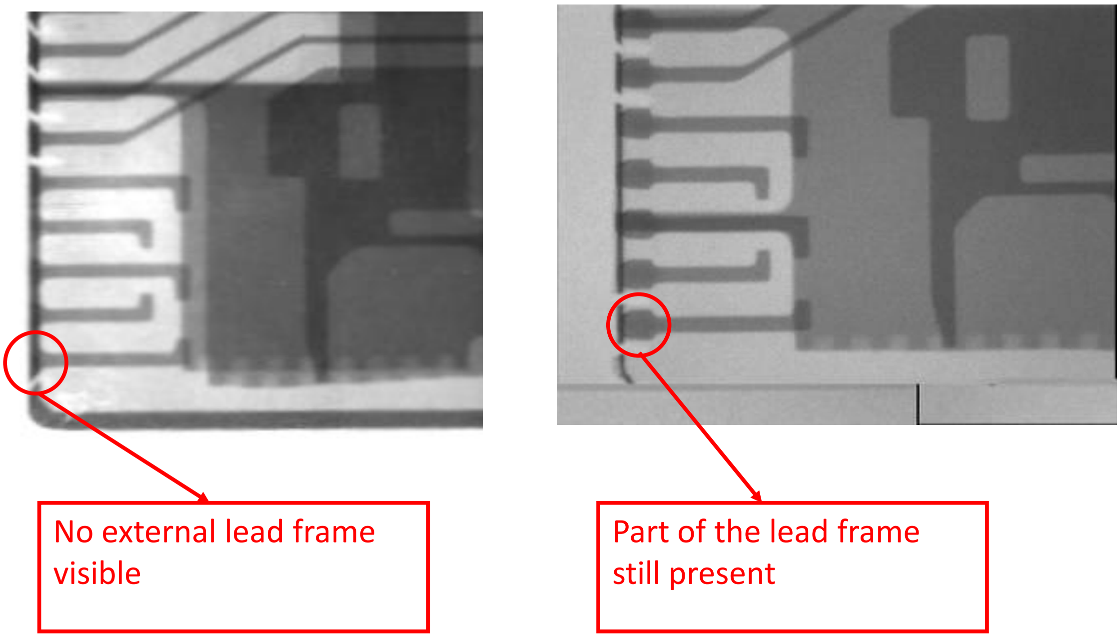

Figure IV.5.14: Connections on the 8th layer (left) and on the 5th layer (right)

CHAPTER IV.6

Conclusion

In this part, the developed Simulation Approach has been validated starting with a simple ground plane example. Then a bi-dimensional real case, a three-dimensional test structure and a three-dimensional real case are discussed. These examples focus on three-dimensional SiP-like structures, and do not include TSVs that represent a higher level of density with a smaller pitch. At the time of writing, further research to improve the Simulation Approach for these devices is ongoing.

Conclusions

With the coming of new generation electronic devices, the Failure Analysis community has to take into account a very wide set of new problems. As this world has struggled over the years to find ingenious solutions in order to be able to work on Integrated Circuits made of smaller and smaller transistors, the new challenge relates to the emergence of three-dimensional components and packages. For the first time, these challenges are not only due to the shrinking of the feature sizes, but to a whole new difficulty: stacking more devices inside the packages makes the failure analysis process more and more complicated. This document deals with a step forward in the solution of this problem. In order to perform a failure analysis on a three-dimensional component, there are many variables which need to be taken into account. The same three-dimensionality of the packages make useless a set of techniques which were previously used. Now, only techniques which are non-destructive can be used. The main problem is that removing the package will not in this case expose all of the dies: only the techniques which use the physical phenomena able to traverse matter can be used.

With this in mind some techniques were described in part I: for example, X-Ray tomography is a very good candidate for visualizing defects on three-dimensional structures, as is Lock-in Thermography. However, the most promising technique is Magnetic Microscopy, which permits the gathering of information about the currents from outside the packages. This technique is used nowadays for defect localization at both die and assembly levels in standard bi-dimensional devices. In order to be used for three dimensional components, a number of developments need to be carried out. These developments are the main topic of this work. As in part II the state of the art of Magnetic Microscopy was described in detail, it became clear how the way it is applied today is limiting the current reconstruction procedure.

The new approach, based on the coupling of magnetic acquisitions and simulations, was presented in part III. With the use of this Simulation Approach, it was possible to increase the technique accuracy, and to map currents flowing very far away from the SQUID sensor. This first result was then used to generate fully three-dimensional currents, even on very bulky components. To do that, it was concluded that the measurement of the z component of the magnetic field alone was not enough: it was also necessary to measure all the three components. This was performed by sample tilt: once the sample was tilted, the measurement performed would be used to evaluate the other components of the vector B. Once all the components were measured, the application of the Simulation Approach allowed for full 3D current reconstructions.

Still, to generate the simulations, some model simplifications had to be performed; the current lines were considered mono-dimensional as in a wire model. The time taken over the simulations in this case would be much less. However, this model could not intrinsically take into account bi-dimensional current distributions. This would be the case for currents flowing inside a ground plane of a circuit. In this case, even the standard MCI technique showed its limitations. The solution for this problem was still found in the simulations: the bi-dimensional distributions could be discretized, not as in a usual Finite Element Method simulator, which would be far too time consuming, but as a resistors network. Once the currents flowing in each branch of the network were evaluated, the magnetic field could be simulated and compared to the measurements, by applying the Simulation Approach described earlier. Finally, in part IV the new discoveries in the field of Magnetic Microscopy were validated through their application on four case studies. All the applications of the technique were shown: on a ground plane, with the help of a test vehicle; on a standard Integrated Circuit, with the application of the Simulation Approach in two dimensions; on a three-dimensional test vehicle; and, finally, on a real SiP Failure Analysis. All the analyses were described in detail.

This work has opened the door to a new range of possible developments. The research done on the Simulation Approach is just a first step in the solution of three-dimensional failure localization. This approach has demonstrated that there still is important information coming out from the magnetic field which so far has not had been used. The simulations are the way to extract the maximum from this information, in order to increase localization accuracy and to generate three-dimensional current maps. This technique can then be developed further: the transformations performed on the current lines can be extended to a whole new set; the simulation itself can be optimized and quickened. Regarding the acquisitions, they can still be improved: a thorough study of the available sensors can enable the map of currents at very high resolution, and the acquisition of more than one component of the magnetic field at the same time.

Furthermore, as electronic technologies keep developing, Failure Analysis is always expected to be able to solve the problems, even on the most up-to-date components. New developments of TSVs bring the 3D defect localization problem to a whole new perspective: the working distances are no longer very high, but there is a high integration density in very small volumes. This is then transferred to the interconnections: with more dies stacked on top of each other, there is a large number of vertical connections, at very small distances from each other. For these cases, adding one segment at a time to the simulation model is no longer possible. Some recent work on the Simulation Approach has shown how very dense current layouts can bias the simulations, if all the currents are not taken into account [71]. In cases like this, the Simulation Approach alone is not able to localize with precision all the currents, unless a more or less automatized algorithm is found.

It is very well known, in fact, that the job of a failure analyst will become more and more challenging in the years ahead, as the development of the techniques adopted cannot move at the same speed as the microelectronics technologies themselves. Some new ways of performing the defect localization step need to be found. The direction taken by this work is that of using the simulations to enhance standard Magnetic Microscopy: however, a whole set of possibilities is open for research. It is possible, for example, to integrate several techniques in the same process, as some complement each other. In this way MM could be coupled with X-Ray tomography: where the former generates the map of the currents, the latter can generate the background structure where the currents could be superposed. Or, LiT can be used to precisely localize, in space, a change in the impedance which has already been pinpointed by advanced TDR techniques. The new perspectives, as standard techniques are reaching their final physical limitations, are to use them in combination.

Scientific contributions of the author

Publications as first author

F. Infante, P. Perdu, S. Petremont, and D. Lewis, ”A new Methodology for Short Circuit Localization on Integrated Circuits using Magnetic Microscopy Technique Coupled with Simulations,” in *16th IEEE International Symposium on the Physical and Failure Analysis of Integrated Circuits*, pp. 208-212, IEEE, 2009.

F. Infante, M. Gabarrot, P. Perdu and D. Lewis, ”Ultimate Resolution for Current Localization by means of Magnetic techniques,” in *Proceedings of 35th ISTFA*, pp. 314-318, 2009.

F. Infante, P. Perdu and D. Lewis, ”Magnetic microscopy for 3D devices: Defect localization with high resolution and long working distance on complex system in package,” *Microelectronics Reliability*, vol. 49, no. 9-11, pp. 1169-1174, 2009.

F. Infante, R. Gomes, P. Perdu, F. Battistella, S. Annerau and D. Lewis, ”Magnetic Microscopy for 3D Structures: use of the Simulation Approach for the Precise Localization of Deep Buried Weak Currents” in *Proceedings of 36th ISTFA*, pp. 71-78, 2010.

F. Infante, P. Perdu and D. Lewis, ”Magnetic Microscopy for ground plane current detection: a fast and reliable technique for current leakage localization by means of magnetic simulations” *Microelectronics Reliability*, vol. 50, no. 9-11, pp. 1700-1705, 2010.

F. Infante, P. Perdu, H.B. Kor, C.L. Gan and D. Lewis, ”Magnetic field spatial Fourier analysis: A new opportunity for high resolution current localization” *Microelectronics Reliability*, vol. 51, no. 9-11, pp. 1684-1688, 2011.

Other publications

P. Perdu and F. Infante, ”Facing more than moore, is magnetic microscopy the new Swiss knife for 3D defect localization in SiP?,” in *17th IEEE International Symposium on the Physical and Failure Analysis of Integrated Circuits*, pp. 351-358, IEEE, 2010.

H.B. Kor, F. Infante, P. Perdu, C.L. Gan and D. Lewis, ”3D Current Path in Stacked Devices: Metrics and Challenges,” in *18th IEEE International Symposium on the Physical and Failure Analysis of Integrated Circuits*, IEEE, 2011.

Acronyms

DUT	Device Under Test
EoL	End of Life
FA	Failure Analysis
FIB	Focused Ions Beam
FEM	Finite Elements Method
FWHM	Full-Width at Half Maximum
IC	Integrated Circuit
IR	Infrared
LiT	Lock-in Thermography
MCI	Magnetic Current Imaging
MM	Magnetic Microscopy
MtM	More than Moore
MCM	Multi Chip Module
PCB	Printed Circuit Board
PiP	Package in Package
PoP	Package on Package
SA	Simulation Approach
SAM	Scanning Acoustic Microscopy

SEM	Scanning Electron Microscope
SiP	System in Package
SNR	Signal to Noise Ratio
SoP	System on Package
SoC	System on a Chip
SQUID	Superconducting QUantum Interference Device
TDR	Time Domain Reflectometry
TEM	Transmission Electron Microscope
TSV	Through Silicon Via

Bibliography

[1] G. Moore, "Cramming more components onto integrated circuits," *Electronics Magazine*, vol. 4, 1965. 3, 9

[2] H. Goldstein, "Packages go vertical," *IEEE Spectrum*, vol. 38, no. 8, pp. 46–51, 2001. 3, 14

[3] G. Zhang, M. Graef, and F. van Roosmalen, "The rationale and paradigm of More than Moore," in *Proceedings of 56th Electronic Components and Technology Conference*, pp. 151–157, IEEE, 2006. 3, 10

[4] C. Constantinescu, "Trends and challenges in VLSI circuit reliability," *IEEE Micro*, vol. 23, no. 4, pp. 14–19, 2003. 9

[5] J. Baliga, "Chips go vertical," *IEEE Spectrum*, vol. 41, no. 3, pp. 43–47, 2004. 9, 11

[6] R. Tummala, "Moore's law meets its match (System-on-Package)," *IEEE Spectrum*, vol. 43, no. 6, pp. 44–49, 2006. 9

[7] M. Sham, Y. Chen, L. Leung, J. Lin, and T. Chung, "Challenges and Opportunities in System-in-Package (SiP) Business," in *7th International Conference on Electronic Packaging Technology*, pp. 1–5, IEEE, 2006. 10

[8] M. Sham, H. Fu, J. Lin, L. Leung, Y. Chen, and T. Chung, "Product-Oriented System-in-Package (SiP) Technology for Next Generation Wireless/Portable Electronics," in *1st Electronics System-integration Technology Conference*, vol. 1, pp. 299–303, IEEE, 2006. 10

[9] S. Al-Sarawi, D. Abbott, and P. Franzon, "A review of 3-D packaging technology," *IEEE Transactions on Components, Packaging, and Manufacturing Technology, Part B: Advanced Packaging*, vol. 21, no. 1, pp. 2–14, 1998. 10

[10] J. Zheng, Z. Zhang, Y. Chen, and J. Shi, "3D Stacked Package Technology and Its Application Prospects," in *International Conference on New Trends in Information and Service Science*, pp. 528–533, IEEE, 2009. 12, 13

[11] M. Karnezos, "3D packaging: Where all technologies come together," in *IEEE/CPMT/SEMI 29th International Electronics Manufacturing Technology Symposium*, pp. 64–67, IEEE, 2004. 13

[12] R. Tummala, M. Swaminathan, M. Tentzeris, J. Laskar, G. Chang, S. Sitaraman, D. Keezer, D. Guidotti, Z. Huang, and K. e. a. Lim, "The SOP for miniaturized, mixed-signal computing, communication, and consumer systems of the next decade," *IEEE Transactions on Advanced Packaging*, vol. 27, no. 2, pp. 250–267, 2004. 13

[13] B. Black, M. Annavaram, N. Brekelbaum, J. DeVale, L. Jiang, G. Loh, D. McCaule, P. Morrow, D. Nelson, D. Pantuso, *et al.*, "Die stacking (3D) microarchitecture," in *39th Annual IEEE/ACM International Symposium on Microarchitecture*, pp. 469–479, IEEE, 2006. 13

[14] R. Terrill and G. Beene, "3D packaging technology overview and mass memory applications," in *Proceedings of Aerospace Applications Conference*, vol. 2, pp. 347–355, IEEE, 1996. 14

[15] S. Vempati, N. Su, C. Khong, Y. Lim, K. Vaidyanathan, J. Lau, B. Liew, K. Au, S. Tanary, A. Fenner, R. Erich, and J. Milla, "Development of 3-D Silicon Die Stacked Package Using Flip Chip Technology with Micro Bump Interconnects," in *IEEE International Electronics Components and Technology Conference*, pp. 980–987, IEEE, 2009. 14

[16] N. Sillon, A. Astier, H. Boutry, L. Di Cioccio, D. Henry, and P. Leduc, "Enabling technologies for 3D integration: From packaging miniaturization to advanced stacked ICs," in *IEEE International Electron Devices Meeting*, pp. 1–4, IEEE, 2008. 16

[17] P. Ramm, A. Klumpp, J. Weber, and M. Taklo, "3D System-on-Chip technologies for More than Moore systems," *Microsystem Technologies*, vol. 16, no. 7, pp. 1051–1055, 2010. 16

[18] K. Takahashi, M. Umemoto, N. Tanaka, K. Tanida, Y. Nemoto, Y. Tomita, M. Tago, and M. Bonkohara, "Ultra-high-density interconnection technology of three-dimensional packaging," *Microelectronics Reliability*, vol. 43, no. 8, pp. 1267–1279, 2003. 16

[19] N. Tanaka, Y. Yamaji, T. Sato, and K. Takahashi, "Guidelines for structural and Material-System Design of a Highly Reliable 3D Die-stacked Module with Copper Though-vias," in *IEEE International Electronics Components and Technology Conference*, pp. 597–602, IEEE, 2003. 16

[20] S. Abdullah, S. Mohd Yusof, I. Ahmad, A. Jalar, and R. Daud, "Dicing Die Attach Film for 3D Stacked Die QFN Packages," in *32nd IEEE/CPMT International Electronic Manufacturing Technology Symposium*, pp. 73–75, IEEE, 2007. 16

[21] D. Wilkins, "The bathtub curve and product failure behavior," *Reliability HotWire*, vol. 21, 2002. 17

[22] G. Pfeiffer, “Overview of the failure analysis process for electrical components,” in *Accelerated stress testing handbook*, pp. 127–133, IEEE Press, 2001. 19

[23] C. Durin, R. Ecoffet, D. Lacroix, R. Laulheret, P. Lay, F. Pressecq, O. Puig, and M. Villenave, *Spacecraft Techniques and Technology*, vol. 1. 111, rue Nicolas-Vauquelin 31100 Toulouse - France: CNES, cépaduès editions ed., May 2005. 19

[24] M. Ferrier, “The Failure Analysis Process Flow,” in *Microelectronics Failure Analysis Desk Reference* (A. International, ed.), EDFAS, fifth ed., October 2004. 19

[25] E. D. R. Committee, ed., *Microelectronic Failure Analysis Desk Reference*. ASM international, fifth ed., October 2004. 23

[26] T. M. CD Hartfield, “Acoustic Microscopy of Semiconductor Packages,” in *Microelectronics Failure Analysis Desk Reference* (A. International, ed.), pp. 268–288, EDFAS, fifth ed., October 2004. 24, 25, 26, 27

[27] “Sonoscan website.” `http://www.sonoscan.com`. 24, 27

[28] S. Canumalla, “Resolution of broadband transducers in acoustic microscopy of encapsulated ICs: Transducer selection,” *IEEE Transactions on Components and Packaging Technologies*, vol. 22, no. 4, pp. 582–592, 1999. 24

[29] G. Andriamonje, *Contribution à la modélisation et au développement expérimental de la technique d’acoustique picoseconde pour l’analyse des circuits intégrés*. PhD thesis, Université de Bordeaux, 2004. 28

[30] S. Wang, “X-Ray Microtomography Tools for Advanced IC Packaging Failure Analysis,” in *Microelectronics Failure Analysis Desk Reference* (A. International, ed.), pp. 260–267, EDFAS, fifth ed., October 2004. 28, 29, 30

[31] “Phenix x-ray website.” `http://www.phoenix-xray.com/en/applications`. 29

[32] S. Wang, “Die-level Fault Localization with X-Ray Microscopy,” in *Microelectronics Failure Analysis Desk Reference* (A. International, ed.), pp. 253–259, EDFAS, fifth ed., October 2004. 29

[33] “Xradia website.” `http://www.xradia.com/solutions/semiconductor.php`. 32

[34] D. Smolyansky, “Electronic Package Fault Isolation Using TDR,” in *Microelectronics Failure Analysis Desk Reference* (A. International, ed.), pp. 289–302, EDFAS, fifth ed., October 2004. 32, 33, 34

[35] Y. Cai, Z. Wang, R. Dias, and D. Goyal, "Electro Optical Terahertz Pulse Reflectometry - an innovative fault isolation tool," in *Proceedings of 60th Electronic Components and Technology Conference*, pp. 1309–1315, IEEE, 2010. 35

[36] D. L. Bartonm and P. Tangyunyong, "Thermal Defect Detection Techniques," in *Microelectronics Failure Analysis Desk Reference* (A. International, ed.), pp. 378–397, EDFAS, fifth ed., October 2004. 35, 37

[37] C. Schmidt, C. Grosse, and F. Altmann, "Localization of electrical defects in system in package devices using Lock-in Thermography," in *3rd Electronic System-Integration Technology Conference*, pp. 1–5, IEEE, 2010. 35, 36, 38, 39

[38] O. Breitenstein, W. Warta, and M. Langenkamp, *Lock-in Thermography: Basics and Use for Evaluating Electronic Devices and Materials*, vol. 10. Springer, 2010. 37

[39] C. Schmidt, F. Altmann, R. Schlangen, and H. Deslandes, "Non-destructive defect depth determination at fully packaged and stacked die devices using Lock-in Thermography," in *17th IEEE International Symposium on the Physical and Failure Analysis of Integrated Circuits*, pp. 1–5, IEEE, 2010. 36

[40] F. Wellstood, Y. Gim, A. Amar, R. Black, and A. Mathai, "Magnetic microscopy using SQUIDs," *IEEE Transactions on Applied Superconductivity*, vol. 7, no. 2, pp. 3134–3138, 1997. 40

[41] S. Chatraphorn, E. Fleet, F. Wellstood, L. Knauss, and T. Eiles, "Scanning SQUID microscopy of integrated circuits," *Applied Physics Letters*, vol. 76, pp. 2304–2306, 2000. 40

[42] S. Hsiung, K. Tan, A. Komrowski, D. Sullivan, J. Gaudestad, A. Orozco, E. Talanova, and L. Knauss, "Failure analysis on resistive opens with scanning SQUID microscopy," in *Proceedings on the 42nd International Reliability Physics Symposium*, pp. 611–612, IEEE, 2004. 40

[43] H. Haus and J. Melcher, *Electromagnetic fields and energy*. Prentice Hall Englewood Cliffs, New Jersey, 1989. 44

[44] B. Roth, N. Sepulveda, and J. Wikswo, "Using a magnetometer to image a two-dimensional current distribution," *Journal of applied physics*, vol. 65, no. 1, pp. 361–372, 1989. 49, 52, 55, 56

[45] H. Weinstock, *SQUID sensors: fundamentals, fabrication, and applications*. No. 329 in 3, Kluwer Academic Print on Demand, 1996. 49, 56

[46] S. Chatraphorn, E. Fleet, F. Wellstood, and L. Knauss, "Noise and spatial resolution in SQUID microscopy," *IEEE Transactions on Applied Superconductivity*, vol. 11, no. 1, pp. 234–237, 2001. 56, 57

[47] E. Fleet, S. Chatraphorn, F. Wellstood, and L. Knauss, “HTS scanning SQUID microscopy of active circuits,” *IEEE Transactions on Applied Superconductivity*, vol. 9, no. 2, pp. 4103–4106, 1999. 63

[48] J. Kirtley, “SQUID microscopy for fundamental studies,” *Physica C: Superconductivity*, vol. 368, no. 1-4, pp. 55–65, 2002. 64

[49] L. Knauss, A. Cawthorne, N. Lettsome, S. Kelly, S. Chatraphorn, E. Fleet, F. Wellstood, and W. Vanderlinde, “Scanning SQUID microscopy for current imaging,” *Microelectronics Reliability*, vol. 41, no. 8, pp. 1211–1229, 2001. 65, 66

[50] L. Knauss, S. Woods, and A. Orozco, “Current imaging using magnetic field sensors,” in *Microelectronics Failure Analysis Desk Reference* (A. International, ed.), pp. 303–311, EDFAS, fifth ed., October 2004. 64

[51] F. Gruhl, M. M
"uck, M. Von Kreutzbruck, and J. Dechert, “A scanning superconducting quantum interference device microscope with high spatial resolution for room temperature samples,” *Review of Scientific Instruments*, vol. 72, p. 2090, 2001. 64

[52] A. Orozco, “Magnetic Current Imaging in Failure Analysis,” *EDFA Magazine*, vol. 11, no. 4, pp. 14–21, 2009. 67

[53] F. Felt, “Analysis of a Microcircuit Failure using SQUID and MR Current Imaging,” in *Proceedings of the 31st International Symposium for Testing and Failure Analysis*, vol. 1, ASM International, 2005. 67

[54] L. Knauss, A. Orozco, and S. Woods, “Advances in magnetic-based current imaging for high resistance defects and sub-micron resolution,” in *Proceedings of the 11th International Symposium on the Physical and Failure Analysis of Integrated Circuits*, pp. 267–270, IEEE, 2004. 67

[55] L. Knauss, A. Orozco, S. Woods, and A. Cawthorne, “Advances in scanning SQUID microscopy for die-level and package-level fault isolation,” *Microelectronics Reliability*, vol. 43, no. 9-11, pp. 1657–1662, 2003. 67

[56] M. Hechtl, “Backside GMR Magnetic Microscopy for flip chip and related microelectronic devices,” in *15th International Symposium on the Physical and Failure Analysis of Integrated Circuits*, pp. 1–4, IEEE, 2008. 67

[57] C. Teo, H. Lwin, V. Narang, and J. Chin, “Device-level fault isolation of advanced FC devices using Scanning SQUID Microscopy,” in *15th International Symposium on the Physical and Failure Analysis of Integrated Circuits*, pp. 1–4, IEEE, 2008. 67

[58] S. Woods, N. Lettsome Jr, A. Cawthorne, L. Knauss, and R. Koch, “High resolution current imaging by direct magnetic field sensing,” in *Proceedings of the 29th International Symposium for Testing and Failure Analysis*, p. 6, ASM International, 2003. 67

[59] K. Tan and S. Hsiung, “Integration of Package Analysis Tools to Solve Discontinuity Failures,” in *Proceedings of the 31st International Symposium for Testing and Failure Analysis*, vol. 1, ASM International, 2005. 67

[60] R. Dias, L. Skoglund, Z. Wang, and D. Smith, “Integration of SQUID microscopy into FA flow,” in *Proceedings of the 27th International Symposium for Testing and Failure Analysis*, p. 77, ASM International, 2001. 67

[61] W. Vanderlinde, M. Cheney, E. McDaniel, K. Skinner, L. Knauss, B. Frazier, and H. Christen, “Localizing power to ground shorts in a chips-first MCM by scanning SQUID microscopy,” in *Proceedings on the 38th International Reliability Physics Symposium*, pp. 413–419, IEEE, 2000. 67

[62] B. Schrag, X. Liu, M. Carter, and G. Xiao, “Scanning magnetoresistive microscopy for die-level sub-micron current density mapping,” in *Proceedings of the 29th International Symposium for Testing and Failure Analysis*, pp. 2–5, ASM International, 2003. 67

[63] M. Pacheco and Z. Wang, “Scanning SQUID microscopy for new package technologies,” in *Proceedings of the 30th International Symposium for Testing and Failure Analysis*, p. 67, 2004. 67

[64] K. Wills, O. de Leon, K. Ramanujachar, and C. Todd, “Super-Conducting Quantum Interference Device Technique: 3-D Localization of a Short within a Flip Chip Assembly,” in *Proceedings of the 27th International Symposium for Testing and Failure Analysis*, pp. 69–76, ASM International, 2001. 67

[65] O. Crepel, P. Poirier, and P. Descamps, “Magnetic microscopy for ICs failure analysis: comparative case studies using SQUID, GMR and MTJ systems,” in *Proceedings of the 11th International Symposium on the Physical and Failure Analysis of Integrated Circuits*, pp. 45–48, IEEE, 2004. 67

[66] B. Schrag, M. Carter, X. Liu, J. Hoftun, G. Xiao, *et al.*, “Magnetic current imaging with magnetic tunnel junction sensors: case study and analysis,” in *Proceedings of the 32nd International Symposium for Testing and Failure Analysis*, p. 13, ASM International, 2006. 67

[67] B. Schrag, X. Liu, J. Hoftun, P. Klinger, T. Levin, and D. Vallett, “Quantitative Analysis and Depth Measurement via Magnetic Field Imaging,” *EDFA Magazine*, vol. 7, no. 4, p. 24, 2005. 69

[68] F. Infante, P. Perdu, S. Petremont, and D. Lewis, “A new Methodology for Short Circuit Localization on Integrated Circuits using Magnetic Microscopy Technique Coupled with Simulations,” in *16th IEEE International Symposium on the Physical and Failure Analysis of Integrated Circuits*, pp. 208–212, IEEE, 2009. 94

[69] F. Wellstood, J. Matthews, and S. Chatraphorn, “Ultimate limits to magnetic imaging,” *IEEE Transactions on Applied Superconductivity*, vol. 13, no. 2, pp. 258–260, 2003. 95

[70] F. Felt, L. Knauss, A. Gilbertson, and A. Orozco, “Construction of a 3-D Current Path Using Magnetic Current Imaging,” in *Proceedings of the 33rd International Symposium for Testing and Failure Analysis*, vol. 33, p. 197, ASM International, 2007. 153

[71] H. Kor, F. Infante, P. Perdu, C. Gan, and D. Lewis, “3D Current Path in Stacked Devices: Metrics and Challenges,” in *Proceedings of the 18th International Symposium on the Physical and Failure Analysis of Integrated Circuits*, IEEE, 2011. 168